1225-0767(ISSN Print)
2287-6715(ISSN Online)
한국연구재단 우수등재학술지

Journal of Ocean Engineering and Technology

Vol. 36, No. 3 (Serial Number 166) June 2022

한국해양공학회지

KSOE

www.joet.org

KSOE The Korean Society of Ocean Engineers

Journal of Ocean Engineering and Technology
한국해양공학회지
Vol. 36 No. 3
(Serial Number 166)
June 30, 2022
www.JOET.org

Editorial Board

Research and Publication Ethics Committee

Published on June 30, 2022
Published by The Korean Society of Ocean Engineers (KSOE)
Room 1302, 13, Jungang-daero 180beon-gil, Dong-gu, Busan, 48821, Korea
TEL: +82-51-759-0656 FAX: +82-51-759-0657 E-mail: ksoehj@ksoe.or.kr URL: http://www.ksoe.or.kr
Printed by Hanrimwon Co., Ltd., Seoul, Korea E-mail: hanrim@hanrimwon.co.kr
ISSN(print) 1225-0767 **ISSN(online)** 2287-6715

This journal was supported by the Korean Federation of Science and Technology Societies (KOFST) grant funded by the Korean government.

Journal of Ocean Engineering and Technology
한국해양공학회지

CONTENTS

Volume 36, Number 3 June, 2022

<Original Research Articles>

<Review Article>

GENERAL INFORMATION

"Journal of Ocean Engineering and Technology" is the official journal published by "The Korean Society of Ocean Engineers (KSOE)". The ISO abbreviation is "J. Ocean Eng. Technol." and acronym is "**JOET**". It was launched in 1987. It is published bimonthly in February, April, June, August, October, and December each year. Supplement numbers are published at times.

Journal of Ocean Engineering and Technology (JOET) is a medium for the publication of original research and development work in the field of ocean engineering. JOET covers the entire range of issues and technologies related to the following topics:

Ships and offshore platforms: Design of marine structures; Resistance and propulsion; Seekeeping and maneuvering; Experimental and computational fluid dynamics; Ocean wave mechanics; Fatigue strength; Plasticity; Optimization and reliability; Arctic technology and extreme mechanics; Noise, vibration, and acoustics; Concrete engineering; Thermodynamics and heat transfer; Hydraulics and pneumatics;
Coastal civil engineering: Coastal structures; Port and harbor structures; Soil mechanics; Drilling and exploration; Hydraulics of estuary; Seismic engineering; Coastal disaster prevention engineering;
Ocean renewable energy platforms: Offshore wind turbines; Wave energy platforms; Tidal current energy platforms; Floating photovoltaic energy platforms;
Marine robots: Robot sensor system; Autonomous navigation; Robot equipments; Spatial information and communications; Underwater network; Design of underwater vehicles;
Multidisciplinary areas: Design for safety; IT-based design; IT-based production engineering; Welding mechanics; Control engineering; GPS and GIS; Inspection and sensor; Port and logistics; Leisure boat and deep see water; Offshore process systems engineering; Marine metallic materials; Marine organic materials; Marine Composite materials; Materials properties; Corrosion and Anti-corrosion; Tribology;

It contains original research articles, case reports, brief communications and reviews on technial issues. Conference papers, research papers, diploma papers and academic articles can be submitted.

All of the manuscripts are peer-reviewed. **JOET** has a system where two or more peer reviewers must review each submitted paper and it is operated very strictly.

JOET is being indexed in some prominent database such as Korean Citatation Index (KCI), Google Scholar, Science Central, Korea Science and Directory of Open Access Journals (DOAJ).

For correspondences concerning business matters, author needs to contact KSOE Secretariat by email or phone (e-mail: ksoehj@ksoe.or.kr or Tel: +82 51 759 0656). Correspondences for publication matters can be asked via email to the Editor-in-Chief (email: heroeswise2@gmail.com).

KSOE

Journal of Ocean Engineering and Technology 36(3), 143-152, June, 2022
https://doi.org/10.26748/KSOE.2022.004

pISSN 1225-0767
eISSN 2287-6715

Original Research Article

Changes in the Hydrodynamic Characteristics of Ships During Port Maneuvers

Thi Loan Mai[1], Anh Khoa Vo[2], Myungjun Jeon[1] and Hyeon Kyu Yoon[3]

[1]*Ph.D. Candidate Student, Dept. of Eco-friendly Offshore Plant FEED Eng., Changwon National University, Changwon, Korea*
[2]*Master Candidate Student, Dept. of Smart Environmental Energy Eng., Changwon National University, Changwon, Korea*
[3]*Professor, Dept. of Naval Architecture and Marine Engineering, Changwon National University, Changwon, Korea*

KEY WORDS: Port navigation, Shallow water, Computational fluid dynamics, Model test, Autonomous surface ship, Hydrodynamic forces and moments, Maneuverability, Course stability, Collision avoidance

ABSTRACT: *To reach a port, a ship must pass through a shallow water zone where seabed effects alter the hydrodynamics acting on the ship. This study examined the maneuvering characteristics of an autonomous surface ship at 3-DOF (Degree of freedom) motion in deep water and shallow water based on the in-port speed of 1.54 m/s. The CFD (Computational fluid dynamics) method was used as a specialized tool in naval hydrodynamics based on the RANS (Reynolds-averaged Navier-Stoke) solver for maneuvering prediction. A virtual captive model test in CFD with various constrained motions, such as static drift, circular motion, and combined circular motion with drift, was performed to determine the hydrodynamic forces and moments of the ship. In addition, a model test was performed in a square tank for a static drift test in deep water to verify the accuracy of the CFD method by comparing the hydrodynamic forces and moments. The results showed changes in hydrodynamic forces and moments in deep and shallow water, with the latter increasing dramatically in very shallow water. The velocity fields demonstrated an increasing change in velocity as water became shallower. The least-squares method was applied to obtain the hydrodynamic coefficients by distinguishing a linear and non-linear model of the hydrodynamic force models. The course stability, maneuverability, and collision avoidance ability were evaluated from the estimated hydrodynamic coefficients. The hydrodynamic characteristics showed that the course stability improved in extremely shallow water. The maneuverability was satisfied with IMO (2002) except for extremely shallow water, and collision avoidance ability was a good performance in deep and shallow water.*

Nomenclature

$O-xy$	Earth-fixed coordinate
$o-x_by_b$	Body-fixed coordinate
ψ	Heading angle
U	Ship speed
β	Drift angle
u	Surge velocity
v	Sway velocity
r	Yaw rate
$\dot{u}$	Surge acceleration
$\dot{v}$	Sway acceleration
$\dot{r}$	Angular acceleration
I_{zz}	Yaw mass motion of inertia
x_G	Longitudinal center of gravity
m	Ship mass
n_P	Propeller revolution
t	Thrust deduction factor
x_P	Longitudinal coordinate of propeller position
y_P	Lateral coordinate of propeller position
w_P	Wake coefficient in maneuvering motion
K_T	Propeller thrust open water characteristic
J_P	Propeller advanced ratio
t_R	Steering resistance deduction factor
a_H	Rudder increase factor
x_H	Longitudinal coordinate of the rudder position
F_N	Rudder normal force
U_R	Resultant rudder inflow velocity
α_R	Effective inflow angle to the rudder
u_R	Longitudinal inflow velocity
v_R	Lateral inflow velocity

Received 13 February 2022, revised 22 March 2022, accepted 8 April 2022
Corresponding author Hyeon Kyu Yoon: +82-55-213-3683, hkyoon@changwon.ac.kr

f_α Rudder lift gradient coefficient
Λ Rudder aspect ratio
ε Ratio of a wake fraction at propeller and rudder positionsAn experimental constant for expressing u_R
κ Ratio of propeller diameter to rudder span
η Flow straightening coefficient
$\gamma_R \beta_R$ Effective inflow angle to the rudder in maneuvering motions
C_P Wake correction coefficient
β_P Geometrical inflow angle the to propeller in maneuvering motions
C Course stability index
l'_r Yaw damping lever
l'_v Sway damping lever

1. Introduction

When a ship navigates in waters with varying depths, such as in-port, straits, and channel, it encounters danger from sinkage and trim, as well as changes in maneuvering characteristics. The interaction influences the behavior of ships in shallow water, and the flow velocity is increased by the gap between the ship bottom and the seabed. Furthermore, because of Bernoulli's law, the pressure field in that area decreased, causing fluctuations in the hydrodynamic forces and moments, changing the attitude of ships, potentially resulting in unexpected collisions.

Research on the influence of shallow water has been conducted in recent years. Duarte et al. (2016) classified the water level in ship maneuvering based on the draft to water depth ratio (h/T) of a ship as deep water: $h/T > 3.0$; medium-deep water: $1.5 < h/T < 3.0$; shallow water: $1.2 < h/T < 1.5$; and extremely shallow water: $h/T < 1.2$. In addition, the authors provided some aspects affected by shallow water as resistance, trim, checking, counter tuning ability, turning diameter, and rate of turn. Jachowski (2008), Yun et al. (2014), and Lee (2021) examined the ship squat, also known as sinkage and trim in shallow water. Delefortrie et al. (2016) conducted the captive model test based on the 6-DOF (degree of freedom) maneuvering model of KVLCC2 (KRISO Very large crude oil carrier 2) at various under keel clearances of 20%, 30%, and 80%. In the study, the ship was forced in the horizontal 3-DOF with free heave and pitch motion, while the roll was estimated from the roll decay test. In addition, some assumptions and numerical analyses were applied to assess the ship in vertical motion. Taimuri et al. (2020) studied the 6-DOF maneuvering model in deep and shallow water. It started from horizontal 3-DOF and non-linear unified seakeeping. The maneuvering time-domain using a numerical decay test was introduced as a rapid method for estimating the heave, roll, and pitch motion. Carrica et al. (2016) used CFD (Computational fluid dynamics) and an experimental study to develop a direct method for zigzag maneuvers in shallow water ($h/T = 1.2$) for KCS (KRISO container ship). A satisfactory relationship between CFD and the experimental study was observed for self-propulsion results and zigzag variables except for the yaw and yaw rate. Lee and Hong (2017) examined the course stability in shallow water for very large vessels like KVLCC2 and DTC using CFD. The study confirmed that the course stability was improved in very shallow water and was more significant in KVLCC2.

Kim et al. (2007) used a mathematical model for a twin-propeller ship. They developed a 4-DOF mathematical model for a maneuvering simulation of a large container ship with a twin-propeller and twin-rudder, including roll motion effects by a model test and numerical simulation. According to the simulation results, the twin-propeller ship reported worse turning but better course-keeping and course-changing abilities than the single-propeller ship. Khanfir et al. (2011) presented a 3-DOF mathematical model for a twin-rudder system. A method based on free-running model test was proposed to estimate the rudder hull interaction coefficients. Di Mascio et al. (2011) used various prediction methods, namely statistical regression, system identification, and RANSE (Reynold-Averaged Navier-Stoke Equation), to estimate the maneuverability behavior of twin-propeller naval ships.

To address collision avoidance, Shaobo et al. (2020) proposed a new collision avoidance decision-marking system based on a modified velocity obstacle method designed for an autonomous ship. Lee et al. (2020) presented a collision avoidance method for multi-ship encounter situations. The round generating algorithm, which consisted of course changing and track keeping, was introduced to guide the ship to turn away from the obstacles and steer the ship back. Yim (2021) identified the effect of turning characteristics on collision avoidance for maritime autonomous surface ships. A method that could change the rudder angle and the ship speed was proposed to investigate the effect of turning ability on collision avoidance.

This study presented the maneuvering characteristics of an autonomous surface ship in deep and shallow water at low speed. A numerical simulation in CFD was used to estimate the hydrodynamic forces and moments by running the virtual captive model test. The accuracy of the numerical method was demonstrated by comparing the hydrodynamic forces and moments with the results obtained from the model test in the case of static drift test in deep water. The maneuvering characteristics as course stability and maneuvering simulation were then performed using the hydrodynamic coefficients obtained to evaluate the stability and maneuverability of the ship in deep and shallow water. A simple collision avoidance situation was also executed to investigate the effect of shallow water on the collision avoidance ability.

2. Maneuvering Simulation Model

2.1 Objective

The candidate ship used in this study was an autonomous surface ship equipped with a twin rudder, twin propeller, and a skeg in the center of the stern. Fig. 1 shows a scale model of 1/11 attaching a

Fig. 1 Model test

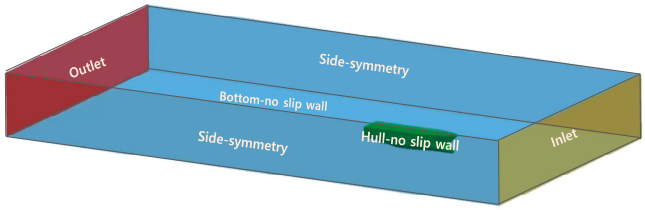

Fig. 2 Boundary domain and boundary condition

Table 1 Main particulars of the autonomous surface ship

Item (unit)	Symbol	Full scale	Model scale
Scale ratio	λ	1	1:11
Length perpendicular (m)	L_{pp}	22.000	2.000
Breadth (m)	B	6.000	0.545
Draft (m)	T	1.250	0.114
Volume (m^3)	∇	85.681	0.064
Rudder lateral area (m^2)	A_R	0.518 × 2	0.004 × 2
Propeller diameter (m)	D_P	0.950	0.086

twin-rudder and skeg used in the experimental study. Fig. 2 displays the boundary domain of a full-scale ship which consists of a bared hull and skeg, which is applied to numerical study in CFD. Table 1 lists the main particulars of the hull, propeller, and rudder. The propeller and rudder specifications were used in the maneuvering simulation.

2.2 Test Condition

The full-scale ship was assumed to operate at a low speed of 1.54 m/s in shallow water areas. The static drift, circular motion, and combined circular motion were simulated for a full-scale ship in deep and shallow water with water depth ratios of 2.0, 1.5, and 1.2, respectively, using a numerical simulation in CFD. Furthermore, an experiment of scale-model with the length between perpendiculars of 2.0 m was performed in a towing tank in deep water to verify the accuracy of numerical simulation. A corresponding 1.54 m/s in the

Table 2 Calculation matrix of the virtual captive model tests

Test type	Motion variables
Static drift test	β = 0°, ±3°, ±6°, ±9°, ±12°, ±15°, ±18°
Circular motion test	r' = ±0.2, ±0.3, ±0.4, 0.5
Horizontal circular motion with drift test	β = ±3°, +6°, +9° r' = 0.2, 0.3, 0.4, 0.5

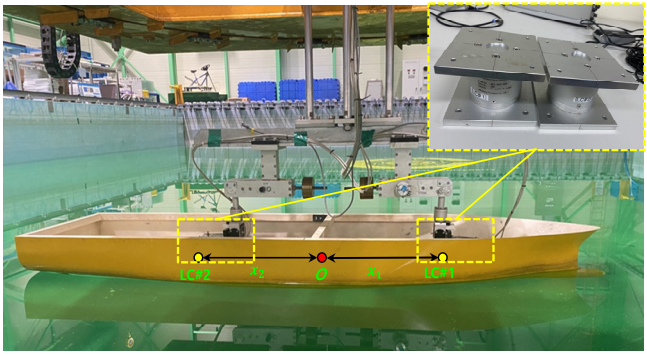

Fig. 3 Experimental installation

speed of full-scale ship, the static drift test of model-scale was towed at 0.47 m/s. The numerical simulation in CFD was conducted under the constraints test listed in Table 2. All damping coefficients were obtained for deep and shallow water.

For this experimental study, the ship was towed by a carriage at a given speed. The hydrodynamic forces and moments were measured using two load cells located near the bow (LC#1) and stern (LC#2), where the distance to the midship was x_1 and x_2, respectively. Furthermore, all motions were restrained throughout the experimental performance. Fig. 3 presents an experimental installation of the ship.

For a numerical study, the virtual captive model test with the test condition in Table 2 was simulated using the Ansys fluent program to calculate the hydrodynamic forces and moments. In Table 2, and are the drift angle β and r' dimensionless yaw rate, respectively.

The continuity and momentum equations were applied as governing equations assuming that the flow was incompressible (Mai et al., 2020). As an ITTC (International Towing Tank Conference) recommendation for CFD (ITTC, 2011), the boundary domain size was large enough to avoid backflow excluding the bottom side, and it was generated under shallow water conditions.

A hybrid mesh that includes the tetrahedral, hexahedral, and prism mesh type were adopted for mesh generation, as shown in Fig. 4. Table 3 lists the analytic method for the CFD simulation. The boundary conditions were set for each domain corresponding to its physical characteristics, such as the inlet assigns the pressure-inlet, the outlet sets the pressure-outlet, the top and sides are symmetry, the ship defines the no-slip wall, and the bottom specifies the no-slip wall to consider the influent of shallow water. The $k-\omega$ SST (Shear stress transport) turbulence model is applied extensively to predict the hydrodynamic forces and moments on a maneuvering ship because of several advantages in terms of its accuracy and time calculation (Quérard et al., 2008). The volume of fluid and open channel flow are

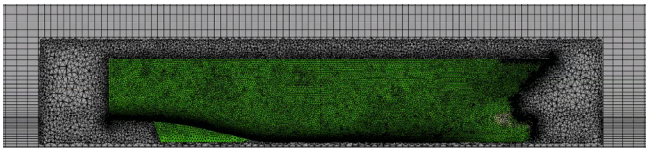

Fig. 4 Hybrid mesh generation

Table 3 Analytic methods for the CFD simulation

	Item	Description
Boundary conditions	Inlet	Pressure-inlet
	Outlet	Pressure-outlet
	Ship	No-slip wall
	Bottom	No-slip wall
	Top, Sides	Symmetry
Method	Two-phase	Volume of fluid Open channel flow
	Circular motion	Multiple reference frames
	Turbulence model	$k-\omega$ Shear stress transport (SST) model
	Algorithm	Semi-implicit method for pressure-linked equations (SIMPLE)
	Gradient	Least squares cell based
	Interpolation method for pressure	Second order upwind
Meshing	y+	300
	Number of elements	about 4.5 million
	Type of mesh	Tetrahedral, hexahedral, and prism

the techniques to define the free surface and two flow phases of water and air. A SIMPLE (Semi-implicit method for pressure-linked equations) algorithm was used to solve the governing equation iteratively, adjusting the pressure to ensure that the resulting velocity field satisfied continuity. The least-squares cell-based method was used to evaluate the gradient of flow variables. The quantities at cell faces were calculated from the cell-centered values by the second-order upwind method. Unlike the static test, the circular motion test determines the rotating fluid zones using a multiple reference frame approach.

2.3 Mathematical Model

Two coordinate systems comprising earth-fixed coordinate (Oxy) and body-fixed (ox_by_b) were set to determine the 3-DOF motion of the horizontal plane, as shown in Fig. 5. The earth-fixed coordinate defined the ship trajectory, orientation angle, and body-fixed (ox_by_b) defined the equation of motion and external force acting on the ship. The origin of the ship was located at the intersection of the midship, centerline, and draft.

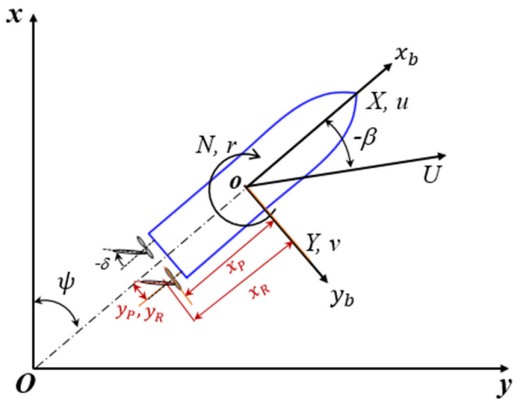

Fig. 5 Coordinate systems

The maneuvering motion of 3-DOF in the horizontal plane was written for surge, sway, and yaw. Eq. (1) expresses the equation of motion of the ship based on the maneuvering modeling group (MMG) model (Yasukawa and Yoshimura, 2015). The external force on the right is the component of hull force, thrust, and rudder force, denoted by the letters H, P, and R.

$$\begin{aligned} m(\dot{u}-vr-x_G r^2) &= X_H+X_P+X_R \\ m(\dot{v}+ur+x_G\dot{r}) &= Y_H+Y_P+Y_R \\ I_{zz}\dot{r}+mx_G(\dot{v}+ur) &= N_H+Y_H+Y_R \end{aligned} \tag{1}$$

The mathematical model of the hull force, thrust, and rudder force on the right side of Eq. (1) was formulated in Eqs. (2), (3), and (4), respectively, for twin-screw naval ship (Kim et al., 2021; Khanfir et al., 2011). The model of the hull forces Eq. (2) was determined as the regression formula of simulation results. In which the damping coefficients regarding sway velocity X_{vv}, Y_v, $Y_{v|v|}$, N_v, and $N_{v|v|}$ were estimated from the static drift test where the sway velocity was generated, the damping coefficients with respect to the yaw angular velocity X_{rr}, Y_r, $Y_{r|r|}$, N_r, and $N_{r|r|}$ were obtained from the circular motion test, where the yaw angular velocity was given, and the coupling damping coefficients relative to sway velocity and yaw rate X_{vr}, Y_{vvr}, Y_{vrr}, N_{vvr}, and N_{vrr} were taken from combined circular motion with drift, where both sway velocity and yaw angular velocity were generated. Furthermore, the added mass coefficients $X_{\dot{u}}$, $Y_{\dot{v}}$, $Y_{\dot{r}}$, $N_{\dot{v}}$, and $N_{\dot{r}}$ were determined from the pure surge, pure sway, and pure yaw test reported by Kim et al. (2021).

$$\begin{aligned} X_H &= X_{\dot{u}}\dot{u}+X_{vv}v^2+X_{vr}vr+X_{rr}r^2-R \\ Y_H &= Y_{\dot{v}}\dot{v}+Y_{\dot{r}}\dot{r}+Y_v v+Y_r r+Y_{v|v|}v|v|+Y_{r|r|}r|r| \\ &\quad +Y_{vvr}v^2r+Y_{vrr}vr^2 \\ N_H &= N_{\dot{v}}\dot{v}+N_{\dot{r}}\dot{r}+N_v v+N_r r+N_{v|v|}v|v|+N_{r|r|}r|r| \\ &\quad +N_{vvr}v^2r+N_{vrr}vr^2 \end{aligned} \tag{2}$$

$$\begin{aligned} X_P &= (1-t)\rho D^4\left[(n^P)^2.K_T^P(J_P^P)+(n^S)^2.K_T^S(J_P^S)\right] \\ Y_P &= 0 \\ N_P &= y_P(1-t)\rho D^4\left[(n^P)^2.K_T^P(J_P^P)-(n^S)^2.K_T^S(J_P^S)\right] \end{aligned} \tag{3}$$

$$\begin{aligned} X_R &= -(1-t_R)(F_N^P+F_N^S)\sin\delta \\ Y_R &= (1+a_H)(F_N^P+F_N^S)\cos\delta \\ N_R &= (x_R+a_H x_H)(F_N^P+F_N^S)\cos\delta-y_R(1-t_R)(F_N^P-F_N^S)\sin\delta \end{aligned} \tag{4}$$

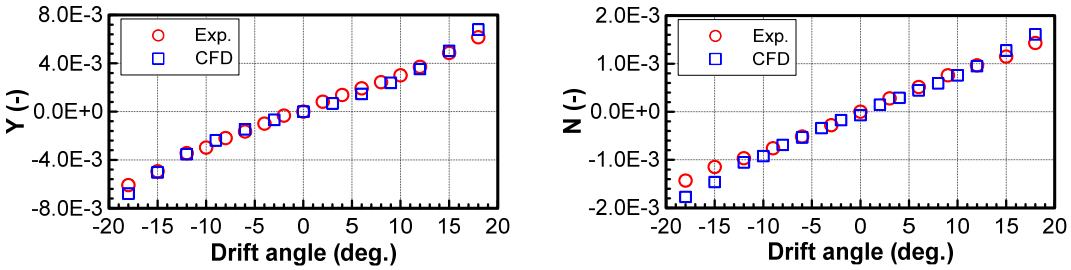

Fig. 6 Comparison of the static drift test on deep water

The parameters mentioned in the thrust model (3) and rudder model (4) are expressed below. The parameter in the formulae was written for the rudder and the propeller on the starboard side (subscript S), so the formulae of the port side could be obtained by replacing them with subscript P, and the formulae are the same except for the flow straightening coefficient (γ_R) and wake correction coefficient (C_P). γ_R in the sway velocity (v_R) formula of the rudder was different as γ_R^+ and γ_R^-, depending on the sign of the effective inflow angle to the rudder (β_R). Considering the symmetry of twin-propeller and twin-rudder, the same value of γ_R^+ was used as $\beta_R \geq 0$ in the starboard side and $\beta_R < 0$ in the port side, and conversely. Similarly, C_P in the surge velocity of the propeller was also considered symmetrical to the propeller position. According to the sign of the geometrical inflow angle to the propeller (β_P), the same value of C_P^+ was used as $\beta_P \geq 0$ in the starboard side and $\beta_P < 0$ in the port side, and vice versa.

$$J_P^S = \frac{(1-w_P^S)u}{n^S D} \tag{5}$$

$$F_N^S = 0.5\rho A_R \left(U_R^S\right)^2 f_a \sin\alpha_R^S \tag{6}$$

$$f_\alpha = \frac{6.13\Lambda}{\Lambda+2.25}$$

$$U_R^S = \sqrt{\left(u_R^S\right)^2 + \left(v_R^S\right)^2},\ \alpha_R^S = \delta - \tan^{-1}\left(v_R^S/u_R^S\right)$$

$$u_R^S = \varepsilon u_P^S \sqrt{\eta\left[1+\kappa\left(\sqrt{1+\frac{8K_T^S}{\pi\left(J_P^S\right)^2}}-1\right)\right]^2 + (1-\eta)}$$

$$v_R^S = \gamma_R^S\left(v + l_R r\right)$$

$$(\beta_R = -\left(v' + l_R' r'\right),$$

$$\gamma_R^S = \gamma_R^+ \text{ when } \beta_R \geq 0,\ \gamma_R^S = \gamma_R^- \text{ when } \beta_R < 0)$$

$$u_P^S = \left(1-w_P^S\right)u \text{ with } w_P^S = w_{P0}\exp\left(-C_P^S.\beta_P^2\right)$$

$$(\beta_P = -\left(v' + x_P' r'\right),$$

$$C_P^S = C_P^+ \text{ when } \beta_P \geq 0,\ C_P^S = C_P^- \text{ when } \beta_P < 0)$$

3. Analysis results

3.1 Verification

The modeling and simulation method in CFD was verified by comparing the results of the sway force and yaw moment of static drift test in the deepwater with the experimental results, as shown in Fig. 6. The simulation results matched well with the experimental method, particularly at slight drift angles (<±12°). The yaw moment differed slightly as the drift angle increased, and it was asymmetrical between the negative and positive drift angles. On the other hand, this did not affect maneuvering analysis because of the required linear coefficients. The comparison demonstrated the accuracy of the simulation method in estimating the hydrodynamic forces and moments on a maneuvering ship.

3.2 CFD Simulation Results

The static test was performed to estimate the damping coefficients versus the velocities and yaw rate of the surface ship; it was the static drift, circular motion, and combined circular motion with drift. Table 4 provides details of the hydrodynamic force model for each test. The hydrodynamic force model was divided into a linear model, where the linearity of the force was measured at small motion variables, and a

Table 4 Static hydrodynamic force model for the hull motion variables

Test type	Model	Formula
Static drift	Linear	$\begin{cases} X_{HD} = X_0 \\ Y_{HD} = Y_0 + Y_v v \\ N_{HD} = N_0 + N_v v \end{cases}$, -9 <β< 9°
	Non-linear	$\begin{cases} X_{HD} = X_0 + X_{vv} v^2 \\ Y_{HD} = Y_0 + Y_v v + Y_{v\|v\|} v\|v\| \\ N_{HD} = N_0 + N_v v + N_{v\|v\|} v\|v \end{cases}$
Circular motion	Linear	$\begin{cases} X_{HD} = X_0 \\ Y_{HD} = Y_0 + Y_r r \\ N_{HD} = N_0 + N_r r \end{cases}$, $r' < 0.4$
	Non-linear	$\begin{cases} X_{HD} = X_0 + X_{rr} r^2 \\ Y_{HD} = Y_0 + Y_r r + Y_{r\|r\|} r\|r\| \\ N_{HD} = N_0 + N_r r + N_{r\|r\|} r\|r\| \end{cases}$
Combined circular motion with drift	Non-linear	$\begin{cases} X_{HD} = X_0 + X_{vv} v^2 + X_{rr} r^2 + X_{vr} \\ Y_{HD} = Y_0 + Y_v v + Y_{v\|v\|} v\|v\| + Y_r r \\ \quad + Y_{r\|r\|} r\|r\| + Y_{vvr\|} v^2 r + Y_{vrr} v r^2 \\ N_{HD} = N_0 + N_v v + N_{v\|v\|} v\|v\| + N_r r \\ \quad + N_{r\|r\|} r\|r\| + N_{vvr} v^2 + N_{vrr} v r^2 \end{cases}$

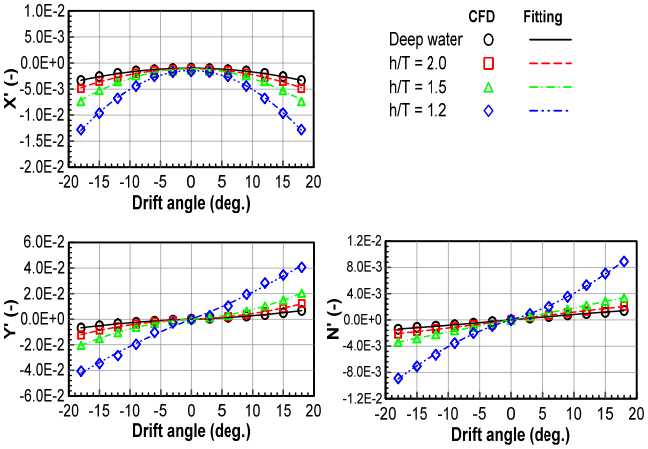

Fig. 7 Static drift test

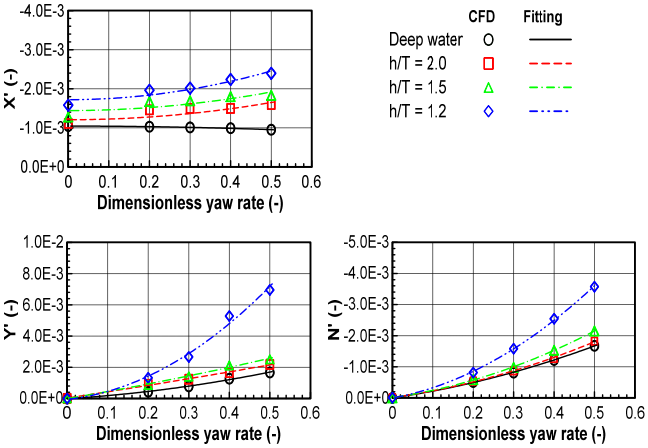

Fig. 8 Circular motion test

non-linear model, where the non-linearity of the force was predicted at greater motion variables. Non-dimensionalization complies with the prime system of the Society of Naval Architects and Marine Engineers (SNAME), in which non-dimensional forces and moments were written as $F' = F/(0.5\rho U^2 L^2)$ and $M' = M/(0.5\rho U^2 L^3)$, respectively. This model was applied to the ship under deep and shallow water conditions. Fig. 7 presents the results of the static drift test at various water depths. The results were obtained by adjusting the drift angle by±18°. As the water depth became shallower, the hydrodynamic forces and moments were greater, particularly in extremely shallow water (h/T = 1.2). It increased two times compared to h/T= 1.5.

Similar to the static drift test, the hydrodynamic forces and moments in the circular motion test were obtained by changing the yaw angular velocities, as shown in Fig. 8. Fig. 9 shows the results of the combined circular motion with drift by varying drift angles and yaw angular velocities. The hydrodynamic forces and moments increased with decreasing water depth, and the drift angle and yaw angular velocity increased. The hydrodynamic forces and moments increased slightly from deep to medium shallow water but significantly increased in extremely shallow water. These results proved the influence of shallow water on the sway velocity and yaw rate. The increase in hydrodynamic forces and moments in shallow water was caused by an increase in flow velocity and a decrease in pressure through the gap between the ship bottom and the seabed. Fig. 10 shows the increase in flow velocity through the gap between the ship bottom and seabed as water depth becomes shallower. Table 5 lists the damping coefficients in deep and shallow water.

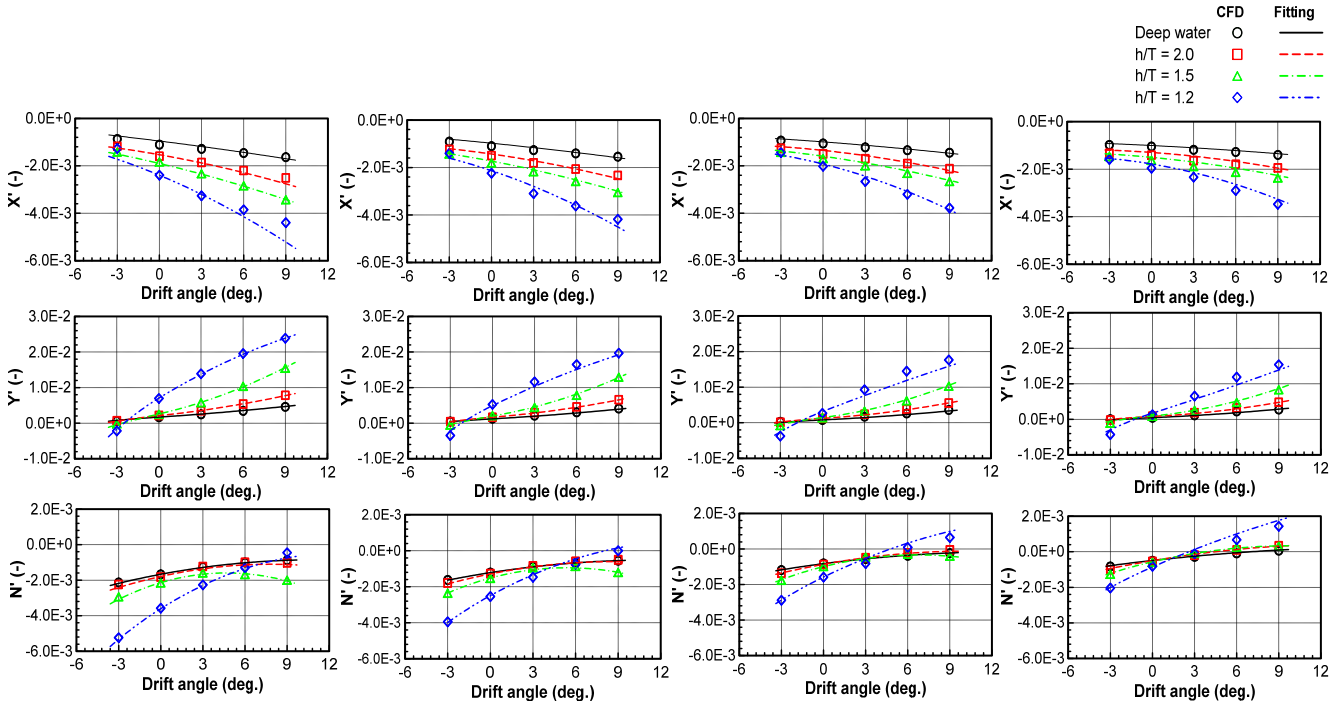

(a) r' = 0.2 (b) r' = 0.3 (c) r' = 0.4 (d) r' = 0.5

Fig. 9 Results of horizontal circular motion tests

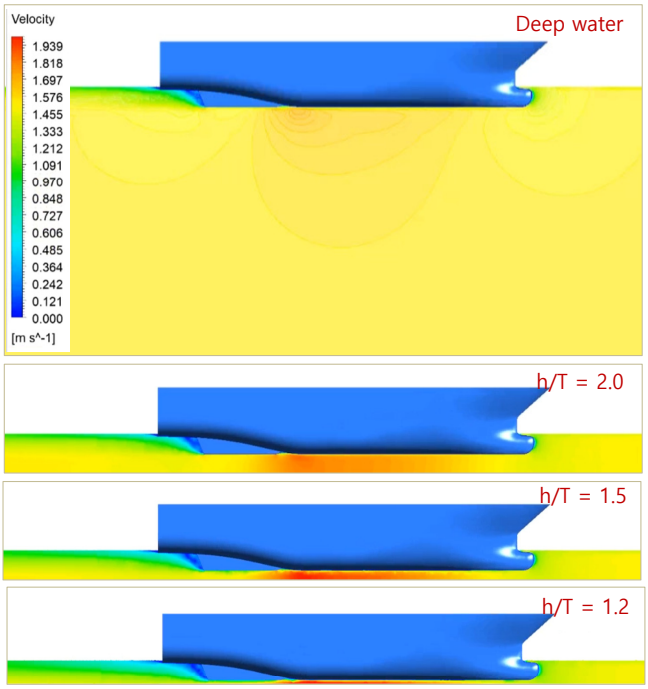

Fig. 10 Velocity field in deep and shallow water

Table 5 Damping coefficients in deep and shallow water

HD Coeff.	Deep water	h/T = 2.0	h/T = 1.5	h/T = 1.2
X_{vv}	-1.84E-02	-3.84E-02	-6.32E-02	-1.17E-01
X_{rr}	2.26E-03	-1.14E-03	-1.19E-03	-2.94E-03
X_{vr}	6.47E-03	1.12E-03	1.61E-02	2.84E-03
Y_{v}	-7.56E-03	-1.18E-02	-1.76E-02	-3.17E-02
$Y_{v\|v\|}$	-4.21E-03	-9.71E-02	1.64E-01	-1.85E-01
Y_{r}	9.35E-03	1.05E-02	1.06E-02	1.25E-02
$Y_{r\|r\|}$	3.64E-03	5.80E-04	1.62E-03	1.80E-02
Y_{vvr}	-2.72E-02	-3.45E-02	7.91E-02	-7.55E-01
Y_{vrr}	-2.47E-02	-5.84E-02	-1.45E-01	-3.12E0-1
N_{v}	-3.10E-03	-4.16E-03	-6.00E-03	-1.03E-02
$N_{v\|v\|}$	-1.54E-03	-1.37E-04	-3.32E-03	-1.05E-02
N_{r}	-1.35E-03	-1.43E-03	-1.60E-03	-2.53E-03
$N_{r\|r\|}$	-2.93E-03	-3.55E-03	-4.87E-03	-9.75E-03
N_{vvr}	-3.96E02	-7.08E-02	-1.70E-01	-1.51E-01
N_{vrr}	-1.65E-03	-1.14E-02	-1.63E-02	-4.10E-02

4. Dynamic Simulation

4.1 Course Stability

Stability analysis was performed to evaluate the course stability relative to the course of a ship. It was analyzed based on the linear hydrodynamic coefficients. As mentioned above, the linear coefficients were obtained by analyzing the hydrodynamic forces and moments at a small motion variable as the drift angle was smaller than 6° in the static drift test and the non-dimensional yaw angular velocity was less than 0.3 in the circular motion test. The course stability was examined as a function of the water depth using a sway-damping lever ($l'_v = N'_v/Y'_v$), yaw damping lever ($l'_r = N'_r/(Y'_r - m')$), and course stability index ($C = N'_r/(Y'_r - m') - N'_v/(Y'_v)$). The course was stable if the value of the course stability index was positive but was unstable if negative. Fig. 11 shows the results of the course stability based on the water depth. The sway damping lever decreased gradually while the yaw damping lever increased as the depth became shallower. In particular, a rapidly increasing yaw damping lever was observed in extremely shallow water (h/T= 1.2). The course stability index showed that it was unstable from deep water to h/T= 1.5 and improved in extremely shallow water. The yaw damping lever affected the course stability significantly.

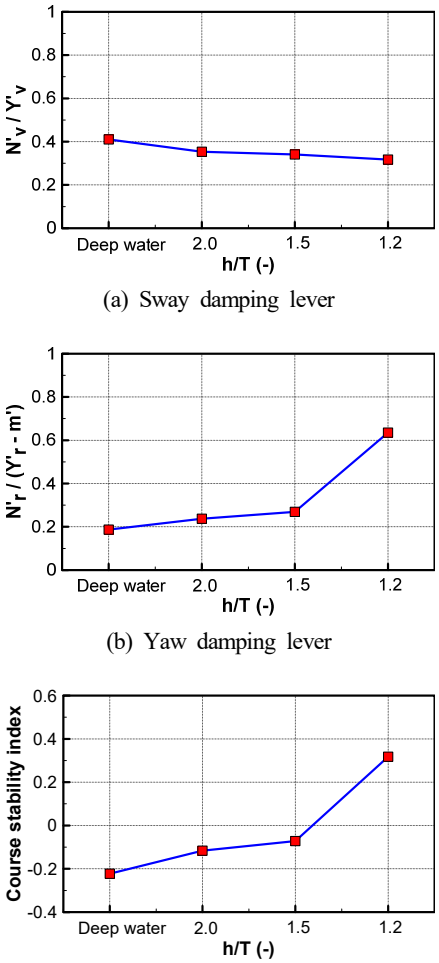

Fig. 11 Shallow water effects on course stability

4.2 Maneuverability Simulation

The maneuvering performance of the ship in shallow water was evaluated by simulating the turning circle 35° to the starboard side and zigzag 10°/10° test under an initial speed of 1.54 m/s. It was obtained by solving the 3-DOF equation of motion with the maneuvering coefficients, in which the damping coefficients were determined by the virtual captive model test, as shown in Table 5. The added mass

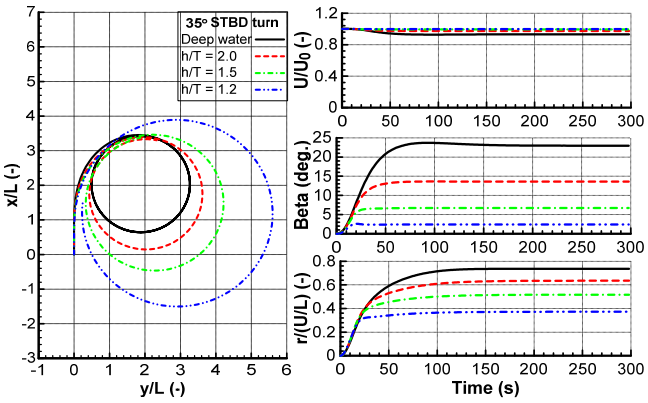

Fig. 12 Results of turning test

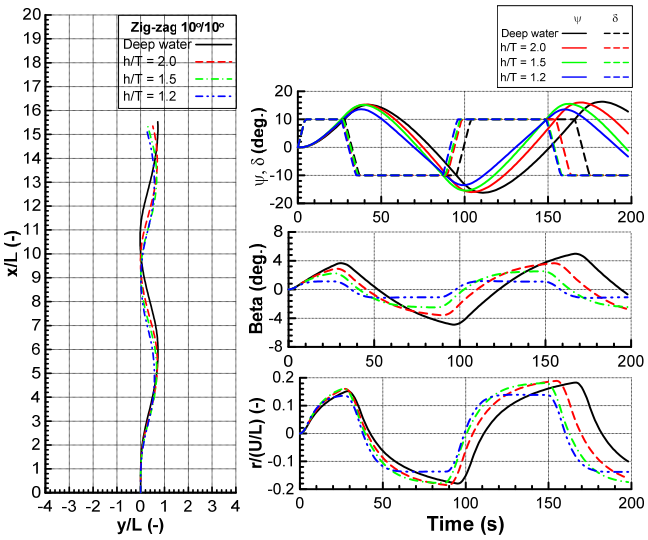

Fig. 13 Results of zig-zag 10°/10° test

coefficients were obtained from Kim et al. (2021), and the interaction coefficients of the rudder model and thrust model were taken from Kim et al. (2021). Figs. 12 and 13 present the results of turning circle and zigzag 10°/10° in the deep and shallow water. The turning circle was similar to the previous studies. The turning rate and drift angle were reduced, leading to a larger trajectory than that in deep water. This suggests that the influence of shallow water increased with decreasing water depth to $h/T = 1.2$. It was caused by the increasing hydrodynamic forces acting on the hull as the depth decreased. Therefore, the turning parameters in $h/T = 1.2$ did not satisfy the International Maritime Organization (IMO) (IMO, 2002). For the zigzag 10°/10° test, the first overshoot angle was more dominant at $h/T = 1.5$, 2.0, and smaller at $h/T = 1.2$ compared with those of deep water. By contrast, the second overshoot angle decreased gradually with increasing water depth to $h/T = 1.2$. Furthermore, the zigzag maneuver satisfied the IMO (2002) for deep and shallow waters.

The ship collision avoidance was conducted to examine the effect of shallow water on the collision avoidance ability of the ship. The dynamic model was applied to the equation of motion for both the own ship (OS) and target ship (TS) to simulate the ship collision avoidance. A simple scenario based on the encounter situation of the cross-right

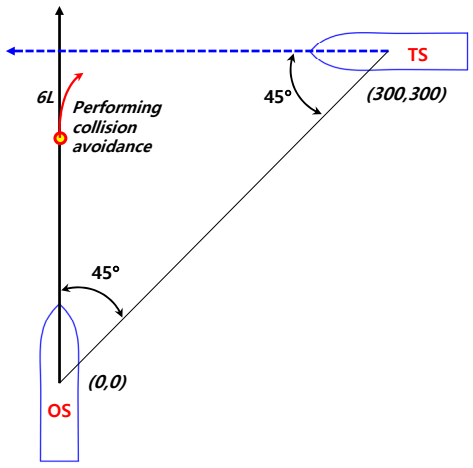

Fig. 14 Simple scenario of collision avoidance

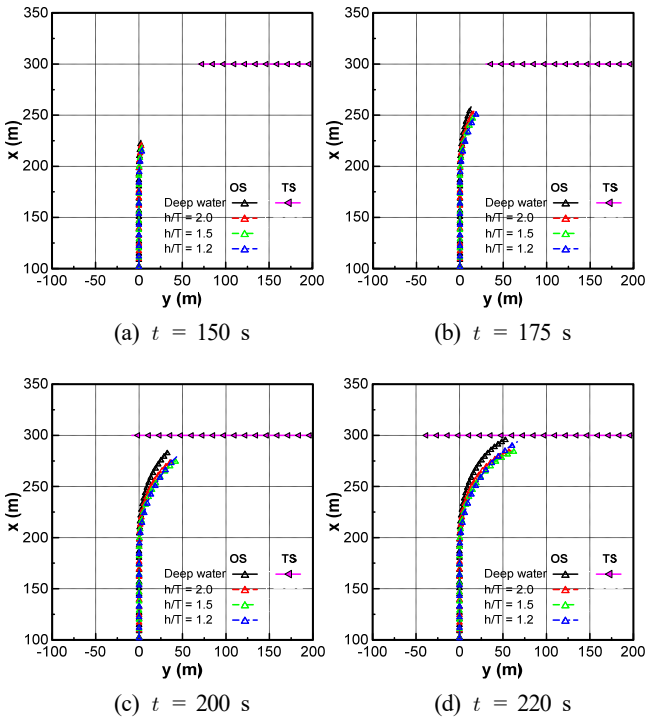

(a) t = 150 s (b) t = 175 s

(c) t = 200 s (d) t = 220 s

Fig. 15 Collision avoidance simulation

according to the International Regulations for Preventing Collisions at Sea (COLREGs), was undertaken in this study, as shown in Fig. 14. Collision avoidance was implemented when the owner detected the trajectory of the target ship at a distance of $6L$, as suggested by Fuji's ellipse model based on the collision risk (Fuji and Tanaka., 1971). The rudder or propeller was then commanded to prevent the collision. In this case, the rudder of the own ship was turned 10° when it was a distance of $6L$ from the target ship. Fig. 15 shows the collision avoidance simulation in deep and shallow water at different times. The collision avoidance ability of the ship was expressed well in both deep and shallow water because the target ship could reach a safe area when the own ship touched the trajectory of the target ship. On the other hand, the ability to avoid collisions in shallow water appeared to be superior.

5. Concluding Remarks

This study examined the hydrodynamic characteristics of an autonomous surface ship throughout the port maneuvers.

A numerical study in CFD was used to perform the virtual captive model test to measure the hydrodynamic forces and moments in deep and shallow water. In addition, a model test for static drift test in deep water was also carried out to demonstrate the accuracy of the numerical study, and a good agreement was observed between the experimental and numerical study. The numerical results in shallow water confirmed that the hydrodynamic forces and moments increased as water depth became shallower because of the accelerating flow velocity through the gap between ship bottom and seabed. The maneuvering coefficients were determined by distinguishing a linear model from the non-linear model, in which the linear coefficients were achieved from small motion variables.

The hydrodynamic characteristics in deep and shallow water were analyzed by assessing the course stability, maneuvering simulation, and collision avoidance. The course stability was conducted using the linear coefficients. The sway-damping lever decreased gradually while the yaw-damping lever increased as the deep water became shallower, and the course stability improved in extremely shallow water. A maneuvering simulation was obtained by solving the 3-DOF equation of motion with the mathematical models of twin-propeller and twin rudder. This denoted a larger turning circle in shallow water due to increased hydrodynamic forces and moments. Moreover, the parameters of the turning test and zigzag 10°/10° in deep and shallow water were satisfied with the IMO (2002) except for the parameters of the turning test at $h/T = 1.2$. Furthermore, a simple collision avoidance of cross-right situation was executed to investigate the effect of shallow water on the collision avoidance ability. Shallow water looked better than deep water in the collision avoidance ability of the ship, even though the turning ability was better in deep water.

Conflict of Interest

Hyeon Kyu Yoon serves as an editor of the Journal of Ocean Engineering and Technology, but has no role in the decision to publish this article. No potential conflict of interest relevant to this article was reported.

Acknowledgments

This research was supported by Changwon National University in 2021-2022.

References

Carrica, P.M., Mofidi, A., Eloot, K., & Delefortrie, G. (2016). Direct Simulation and Experimental Study of Zigzag Maneuver of KCS in Shallow Water. Ocean Engineering, 112, 117−133. https://doi.org/10.1016/j.oceaneng.2015.12.008

Delefortrie, G., Eloot, K., Lataire, E., Van Hoydonck, W., & Vantorre, M. (2016). Captive Model Tests Based 6 DOF Shallow Water Manoeuvring Model. Proceedings of the 4th International Conference on Ship Manoeuvring in Shallow and Confined Water (MASHCON), Hamburg, Germany, 273−286. https://doi.org/10.18451/978-3-939230-38-0

Di Mascio, A., Dubbioso, G., Notaro, C., & Viviani, M. (2011). Investigation of Twin-Screw Naval Ships Maneuverability Behavior. Journal of Ship Research, 55(4), 221−248. https://doi.org/10.5957/JOSR.55.4.090031

Duarte, H.O., Droguett, E.L., Martins, M.R., Lutzhoft, M., Pereira, P. S., & Lloyd, J. (2016). Review of Practical Aspects of Shallow Water and Bank Effects. Transactions of the Royal Institution of Naval Architects Part A: International Journal of Maritime Engineering, 158(July), 177−186. https://doi.org/10.3940/rina.ijme.2016.a3.362

Fuji, J., & Tanaka, K. (1971). Traffic Capacity. The Journal of Navigation, 24, 543-552.

IMO. (2002). Resolution MSC. 137 (76), Standard for Ship Maneuverability. Report of the Maritime Safety Committe on Its Seventy-Sixth Session-Annex 6.

ITTC. (2011). Practical Guidelines for Ship CFD Applications. ITTC − Recommended Procedures and Guidelines, 11−18.

Jachowski, J. (2008). Assessment of Ship Squat in Shallow Water Using CFD. Archives of Civil and Mechanical Engineering, 8(1), 27−36. https://doi.org/10.1016/s1644-9665(12)60264-7

Khanfir, S., Hasegawa, K., Nagarajan, V., Shouji, K., & Lee, S.K. (2011). Manoeuvring Characteristics of Twin-Rudder Systems: Rudder-Hull Interaction Effect on the Manoeuvrability of Twin-Rudder Ships. Journal of Marine Science and Technology, 16(4), 472−490. https://doi.org/10.1007/s00773-011-0140-3

Kim, Y.G., Kim, S.Y., Kim, H.T., Lee, S.W., & Yu, B.S. (2007). Prediction of the Maneuverability of a Large Container Ship with Twin Propellers and Twin Rudders. Journal of Marine Science and Technology, 12(3), 130−138. https://doi.org/10.1007/s00773-007-0246-9

Kim, D.J., Choi, H., Kim, Y.G., & Yeo, D.J., (2021), Mathematical Model for Harbour Manoeuvres of Korea Autonomous Surface Ship (KASS) Based on Captive Model Tests. Proceedings of Conference of Korean Association of Ocean Science and Technology Societies.

Lee, S.-M. (2021). Reduction of UKC for Very Large Tanker and Container Ship in Shallow Water. Journal of the Korean Society of Marine Environment and Safety, 27(3), 409−420. https://doi.org/10.7837/kosomes.2021.27.3.409

Lee, S., & Hong, C. (2017). Study on the Course Stability of Very Large Vessels in Shallow Water Using CFD. Ocean Engineering, 145(September), 395−405. https://doi.org/10.1016/j.oceaneng.2017.09.064

Lee, M.C., Nieh, C.Y., Kuo, H.C., & Huang, J.C. (2020). A Collision Avoidance Method for Multi-Ship Encounter Situations. Journal of Marine Science and Technology (Japan), 25(3), 925–942. https://doi.org/10.1007/s00773-019-00691-8

Mai, T.L., Nguyen, T.T., Jeon, M., & Yoon, H.K (2020). Analysis on Hydrodynamic Force Acting on a Catamaran at Low Speed Using RANS Numerical Method. Journal of Koran Navigation and Port Research, 44(2), 53–64.

Quérard, A., Temarel, P., & Turnock, S. (2008). Influence of Viscous Effects on the Hydrodynamics of Ship-Like Section Undergoing Symmetric and Anti-Symmetric Motions Using RANS. Proceedings of the 27th International Conference on Offshore Mechanics and Arctic Engineering, Estoril, Portugal, 683–692. https://doi.org/10.1115/OMAE2008-57330

Shaobo, W., Yingjun, Z., & Lianbo, L. (2020). A Collision Avoidance Decision-Making System for Autonomous Ship Based on Modified Velocity Obstacle Method. Ocean Engineering, 215 (July), 107910. https://doi.org/10.1016/j.oceaneng.2020.107910

Taimuri, G., Matusiak, J., Mikkola, T., Kujala, P., & Hirdaris, S. (2020). A 6-DOF Maneuvering Model for the Rapid Estimation of Hydrodynamic Actions in Deep and Shallow Waters. Ocean Engineering, 218, 108103. https://doi.org/10.1016/j.oceaneng.2020.108103

Yasukawa, H., & Yoshimura, Y. (2015). Introduction of MMG Standard Method for Ship Maneuvering Predictions. Journal of Marine Science and Technology (Japan), 20(1), 37–52. https://doi.org/10.1007/s00773-014-0293-y

Yun, K., Park, K., & Park, B. (2014). Study of Ship Squat for KVLCC2 in Shallow Water. Journal of the Society of Naval Architects of Korea, 51(6), 539–547. https://doi.org/10.3744/snak.2014.51.6.539

Yim. J.B., (2021). Effect of Turning Characteristics of Maritime Autonomous Surface Ships on Collision. Journal Navigation Port Research, 45(6), 298–305.

Author ORCIDs

Author name	ORCID
Mai, Thi Loan	0000-0002-0849-3204
Vo, Anh Khoa	0000-0003-0185-2590
Jeon, Myungjun	0000-0002-1655-5364
Yoon, Hyeon Kyu	0000-0001-6639-0927

KSOE

Journal of Ocean Engineering and Technology 36(3), 153-160, June, 2022
https://doi.org/10.26748/KSOE.2022.003

pISSN 1225-0767
eISSN 2287-6715

Original Research Article

Experimental Study on Application of an Optical Sensor to Measure Mooring-Line Tension in Waves

Thi Thanh Diep Nguyen[1], Ji Won Park[2], Van Minh Nguyen[3], Hyeon Kyu Yoon[4], Joseph Chul Jung[5] and Michael Myung Sub Lee[6]

[1]*Graduate Student, Department of Smart Ocean Environmental Energy, Changwon National University, Changwon, Korea*
[2]*Graduate Student, Department of Advanced Defense Engineering, Changwon National University, Changwon, Korea*
[3]*Researcher, Department of Transportation Mechanical Engineering, University of Science and Technology, The University of Danang, Vietnam*
[4]*Professor, Department of Naval Architecture and Marine Engineering, Changwon National University, Changwon, Korea*
[5]*Researcher, Department of R&D manager, IT convergence Laboratory, CyTroniQ Co. Ltd., Cheonan, Korea*
[6]*Researcher, Department of Businesses Development, CyTroniQ Co. Ltd., Cheonan, Korea*

KEY WORDS: Semi-submersible, Triangle platform, Optical sensor, Tension of mooring line, Model test in waves

ABSTRACT: *Moored floating platforms have great potential in ocean engineering applications because a mooring system is necessary to keep the platform in station, which is directly related to the operational efficiency and safety of the platform. This paper briefly introduces the technical and operational details of an optical sensor for measuring the tension of mooring lines of a moored platform in waves. In order to check the performance of optical sensors, an experiment with a moored floating platform in waves is carried out in the wave tank at Changwon National University. The experiment is performed in regular waves and irregular waves with a semi-submersible and triangle platform. The performance of the optical sensor is confirmed by comparing the results of the tension of the mooring lines by the optical sensor and tension gauges. The maximum tension of the mooring lines is estimated to investigate the mooring dynamics due to the effect of the wave direction and wavelength in the regular waves. The significant value of the tension of mooring lines in various wave directions is estimated in the case of irregular waves. The results show that the optical sensor is effective in measuring the tension of the mooring lines.*

1. Introduction

A moored floating platform has great potential in ocean engineering applications because a mooring system is necessary to keep the floating platform in station. In order to do this, the tension of the mooring line is investigated to ensure its bearing capacity. Kim et al. (2005) investigated the mooring dynamics in wind, waves, and currents through a simulation and experiment. In addition, the mooring tension from the simulation's results was compared with experimental results. The effect of the position of the mooring line on the dynamic responses of the spar platforms was studied by Montasir et al. (2015). The platform was connected with asymmetric and symmetric mooring configurations. The dynamic responses of the spar were estimated based on the tension of the mooring lines. Natarajan and Ganapathy (1997) performed a model test on a moored ship to measure the tension of the mooring lines. The model test was carried out with two types of the mooring configurations: spread mooring and berth mooring. The experiment was performed in head sea in various environmental conditions of wind, waves, and current. Other studies on the hydrodynamic characteristics of a moored platform in freak waves were conducted (Pan et al., 2018; Pan et al., 2021). The tension of the mooring line response was increased significantly under the effect of freak waves. In addition, the dynamic response and the tension of the mooring line in the freak waves were compared to that in irregular waves. Cevasco et at. (2018) studied the dynamic response of a floating offshore wind turbine system by conducting a numerical simulation. Two different versions of the mooring dynamics were compared. Paduano et at. (2020) conducted an experiment and

Received 11 February 2022, revised 16 April 2022, accepted 22 May 2022
Corresponding author Hyeon Kyu Yoon: +82-55-213-3683, hkyoon@changwon.ac.kr
This paper was presented on the subject of "Experimental Study on Application of Optical Sensor in Mooring Line of Moored Floating Platform in Waves" in the Proceedings of the 2021 KAOSTS Joint Conference.

numerical simulation to investigate the dynamic motion and tension of floating wave energy converters. Three models of mooring lines were studied. Kim et al. (2016) investigated the anchor tension of a tension leg platform by conducting an experiment and simulation. The anchor tension in regular waves with wind was estimated. The experimental result and simulation result of the anchor tension were compared. Jiang et al. (2020) conducted a numerical simulation using Reynolds-averaged Navier-Stokes (RANS) to investigate a dynamic mooring system, and a coupled methodology potential was used for estimating the moored offshore structures.

The development of optical sensor technology has advanced since the beginning of research on fiber Bragg grating (FBG) sensors by Meltz et al. (1989) and Hill and Meltz (1997). However, the optical sensor has only been applied in the field of naval architecture in recent years. Chung et al. (2021) performed a longitudinal tension experiment to measure the tension of a sample mooring line. An optical sensor was integrated into the mooring line to measure its tension. However, the longitudinal tension experiment just measured the increased loading force without any dynamics of the mooring line. Therefore, it is necessary to investigate the effect of dynamic loading force on the optical sensor.

In order to accurately estimate a mooring line's tension, some sensors are used directly in the mooring line. Most research has used a tension gauge to measure the tension in a mooring line. In the present study, an optical sensor was developed to measure it. The rest of the paper is structured as follows. First, the technical and operational details of the optical sensor are introduced. Second, an experiment with a moored floating platform is presented to check the performance of the optical sensor. The tension of mooring lines measured by the optical sensor and tension gauge are compared. The maximum tension of the mooring lines is estimated to investigate the mooring dynamics due to the effect of the wave direction and wavelength in regular waves. Finally, the significant value of the mooring line's tension in various wave directions is estimated in irregular waves.

2. Optical Sensor

2.1 Characteristic and Technical of Optical Sensor

Fiber-optic strain sensors are among the optical sensors that have recently gained attention across various fields. They have been classified as high intensity, interferometric, and FBG sensors based on the measurement method. Distributed sensing technology has recently been developed since the popularization of optical components by Culshaw and Kersey (2008). An optical sensor has the following advantages: it is unaffected by external electromagnetic waves, it can transmit signals over long distances, and it enables multiplexing, making it convenient to connect numerous sensors due to their structural characteristics. They also have remarkable durability and a life of 20 years. In civil engineering, FBG sensors have been used to monitor large structures, such as bridges and tunnels, and they have recently been applied in mechanical engineering. An FBG creates a

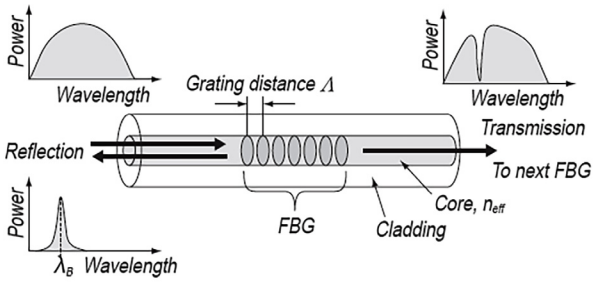

Fig. 1 Characteristics and structure of optical sensor Bragg grating

permanent refractive index modulation on the core in the longitudinal direction of the optical sensor, and this modulation is used as a sensor. Fig. 1 shows a schematic of an FBG structure. When a periodic refractive index modulation is made, coupling is generated between the propagation mode and the reflection mode, so a particular wavelength is reflected.

2.2 Operational Principle of Optical Sensor

The reflected wavelength by an FBG is determined by the spacing and refractive index modulation of the core. Eq. (1) is used to describe this property:

$$\lambda_B = 2n_{eff}\Lambda \tag{1}$$

where λ_B is the Bragg reflection wavelength, n_{eff} is the effective refractive index of the core, and Λ is the grating spacing that generates the refractive index modulation. The reflective wavelength of the FBG is influenced by external temperature and stress. The refractive index of the core varies with temperature. Hence, the reflection wavelength is changed. Moreover, the grating spacing changes with stress and consequently changes the reflection wavelength. These changes can be estimated by Eq. (2):

$$\frac{\Delta\lambda_B}{\lambda_R} = (1+P_\epsilon)\epsilon + \xi\Delta T \tag{2}$$

where P_ϵ is the effective photo-elastic coefficient, ϵ is the applied stress, ξ is the thermo-optic coefficient, and ΔT is the relative temperature change. Generally, the effective photo-elastic coefficient of a single-mode optical sensor is 0.22. For an FBG made from a single-mode optical fiber, the Bragg center wavelength modification due to the stress applied in the axial direction is generally adopted as 1.4 pm/microstrain in a 1550 nm band. In addition, the shift in the Bragg center wavelength because of temperature change is 10 pm/°C.

2.3 Design and Fabrication of Optical Sensor

A photosensitive single-mode optical fiber that responds to light in the ultraviolet region is used to produce an FBG. Photosensitivity is increased by injecting hydrogen into the core at high pressures or by doping with Ge. A phase mask is used to create a periodic refractive index modulation in an optical fiber with increased photosensitivity.

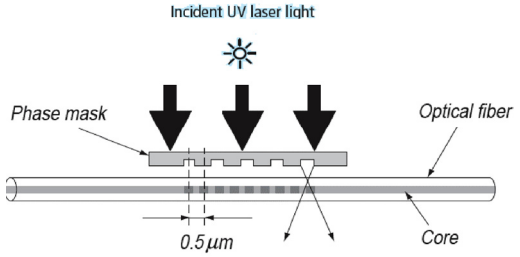

Fig. 2 Optical sensor Bragg grating fabrication method using UV laser and phase mark

The phase mask generates a periodic interference shape through the diffraction effect of light. As shown in Fig. 2, an excimer that generates light within the range of 190–250 nm and an argon laser with a frequency doubler are used to generate ultraviolet light, which is transmitted through the phase mask on the photosensitive optical fiber. The pattern with periodic intervals passing through the phase mask generates a periodic refractive index modulation in the optical fiber, thus producing the FBG. Fig. 3 shows the wavelength characteristics of the produced FBG.

As shown in Fig. 3, the light reflected by the optical sensor grating is transmitted in the direction of the incident optical fiber. Then, it is reflected and returns with the physical quantity information to the point where the FBG is located. The sensors can be multiplexed, assuming that the structure has light sources that can generate various light types and that gratings with different Bragg center wavelengths are connected in series. Therefore, the FBG can be structured with multiple sensors connected in series to one optical sensor, which can be advantageous depending on the application.

A highly effective method for achieving integration in the structure is the employment of several serialized sensors without additional parallel connections. Since the sensor signal is transmitted to the optical sensor, an amplifier is unnecessary for a distance of up to several kilometers. The FBG can be used in various temperature ranges due to its wide range of operating temperatures. In this study, a technique for measuring the load generated in a mooring was applied by adding an optical sensor. According to Lee and Kim (2011), this dynamic technique can be used for taking up to 100 samples per second by measuring in a specific area where a sensor is installed.

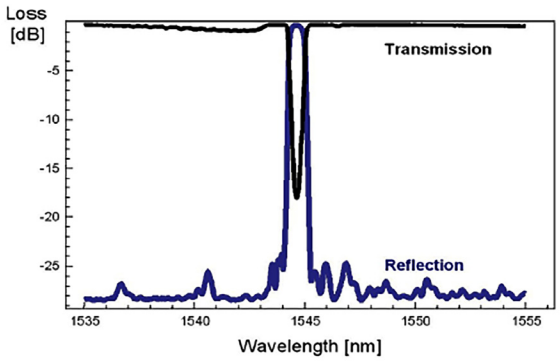

Fig. 3 Reflection and transmission spectrum of optical sensor Bragg grating

3. Performance Test of Optical Sensor

3.1 Experimental Method and Test Conditions

Semi-submersible and triangle platforms were used in the experiment. The model is fixed in the middle position of a square tank. During the experiment, the tension of the mooring lines is measured by an optical sensor and tension gauges. The model of the tension gauge used in this experiment was the WBST-100N gauge made by the Wonbang Company, which has a maximum capacity of 100 N. The principal dimensions of the semi-submersible and triangle platforms are listed in Tables 1 and 2, respectively. Figs. 4 and 5 show the real models of the semi-submersible and triangle platforms that were used in this experiment, respectively.

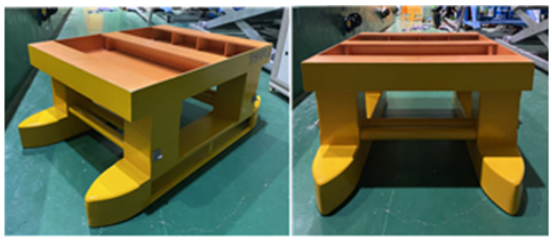

Fig. 4 Model of the semi-submersible

Fig. 5 Model of the triangle platform

Table 1 Principal dimensions of the semi-submersible

Item	Real	Model
Scale ratio (-)	1	1/100
Length overall (m)	104.000	1.040
Breadth overall (m)	65.000	0.650
Breadth/demi-hull (m)	13.000	0.130
Draft (m)	18.000	0.180
Height (m)	36.400	0.364
Displacement (t)	31636	0.032
Distance between center of demi-hull (m)	52.000	0.520

Table 2 Principal dimensions of the triangle platform

Item	Real	Model
Scale ratio (-)	1	1/100
Length between columns axis (m)	50.000	0.500
Column diameter - Middle part (m)	9.500	0.095
Column diameter - Bottom part (m)	10.900	0.109
Column diameter - Top part (m)	11.800	0.118
Height (m)	25.900	0.259
Draft (m)	14.000	0.140
Displacement (t)	3702	0.0037

3.2 Optical Sensor Calibration

Since an optical sensor has several advantages compared to some conventional sensors, it was used to measure the mooring line tension of the semi-submersible and triangle platforms. A calibration test of the optical sensor was carried out first. Then, the relation between the wavelength from the optical sensor and tension was estimated. During the experiment, when ship motion occurs due to waves, the tension of the mooring lines changes. The variation of the wavelength of the optical sensor is recorded. The mooring dynamics in waves is estimated based on the measurement of the wavelength of the optical sensor. The setup for the optical sensor calibration is shown in Fig. 6. The relation between the wavelength and tension measured by the optical sensor is shown Fig. 7.

Fig. 6 Setup for the optical sensor calibration

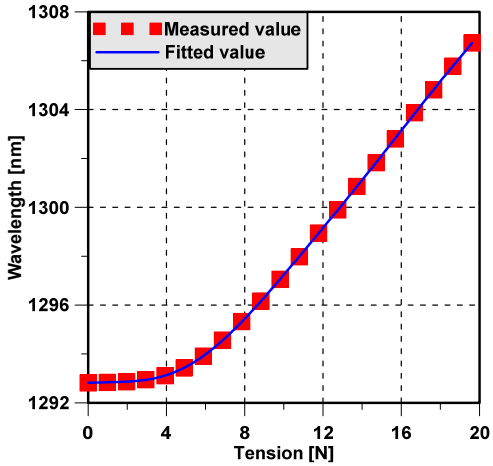

Fig. 7 Result of the optical sensor calibration

3.3 Experimental Setup

In the case of the semi-submersible, the model was attached to the tension gauges, optical sensor, and mooring line connect to a weight at the tank's bottom. The tension of the mooring lines was measured by three tension gauges and an optical sensor. The angle between the mooring lines was 90 degrees. Fig. 8 shows the experimental setup of the semi-submersible. On the other hand, two tension gauges and an optical sensor were attached to the triangle platform. The angle between the mooring lines was 120 degrees. The experimental setup of the triangle platform is shown in Fig. 9. The position of the mooring line in various wave directions in the case of the semi-submersible and triangle platforms are shown in Figs. 10 and 11, respectively.

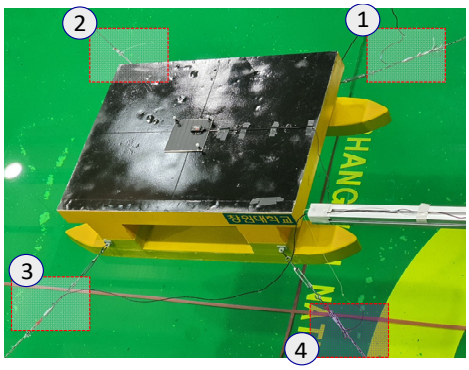

Fig. 8 Experimental setup of the semi-submersible

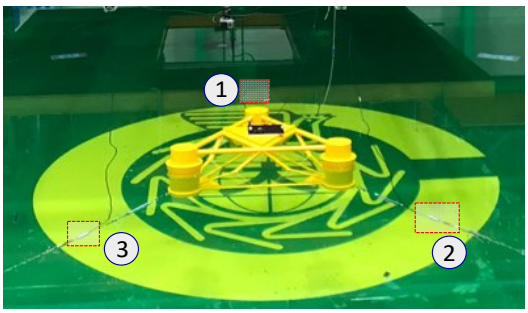

Fig. 9 Experimental setup of the triangle platform

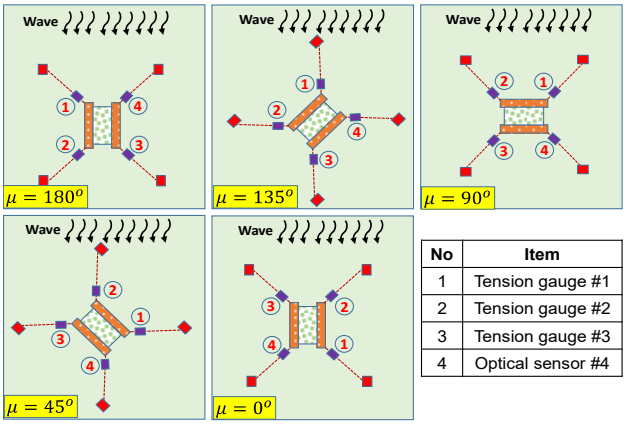

No	Item
1	Tension gauge #1
2	Tension gauge #2
3	Tension gauge #3
4	Optical sensor #4

Fig. 10 Position of the mooring lines in the case of the semi-submersible

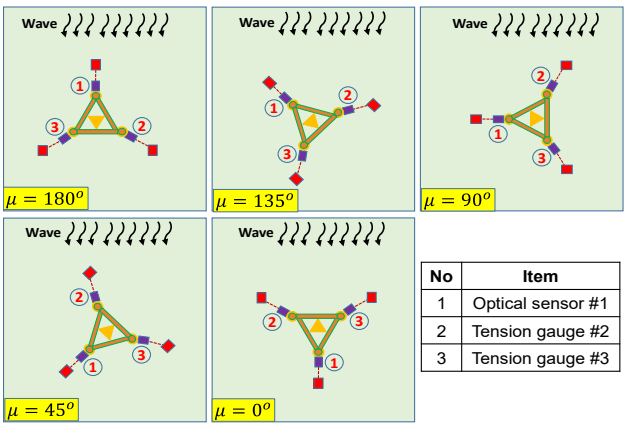

No	Item
1	Optical sensor #1
2	Tension gauge #2
3	Tension gauge #3

Fig. 11 Position of the mooring lines in the case of the triangle platform

3.4 Data Analysis

During the experiment, the signal of the mooring line's tension was recorded by the tension gauges and optical sensor. After each run, the data from tension gauges and optical sensor were checked in the time domain. Reruns were performed for the obvious error cases. The signal output from the tension gauge was converted from a voltage to the measured tension based on a calibration factor. The measured data from the tension gauges and optical fiber were analyzed using the maximum tension of the mooring lines in regular waves. In the case of irregular waves, the significant value of tension was estimated.

4. Result and Discussion

4.1 Performance of the Optical Sensor in Regular Waves

To investigate the effect of wave direction on the mooring dynamics, an experiment was carried out with regular waves and various wave directions. A model test was performed in regular waves to evaluate the tension of the mooring line of the semi-submersible and triangle platforms. Fig. 12 shows the maximum tension of mooring lines in various wave directions of the semi-submersible. The position of the mooring lines in the case of the semi-submersible when the wave direction changes are shown in Fig. 10. In head sea, the trend of tension gauge 1 (TG#1) and the optical sensor (OS#4) at the bow have almost the same trend. Tension gauge 2 (TG#2) and tension gauge 3 (TG#3) at the stern have a similar trend. In following sea, TG#1 and OS#4 change position for TG#2 and TG#3 in head sea. The trend of tension at the bow in head waves is the same as the tension at the bow in following sea. The maximum value of OS#4 has good agreement with TG#1 in head sea and following sea and with TG#3 in beam sea. Therefore, this proves the accuracy of the optical sensor in measuring the tension of the mooring line. In addition, the maximum tension of mooring lines occurs when the mooring lines are parallel to the wave propagation direction. Fig. 11 shows the position of the mooring lines in the case of the triangle platform when the wave direction changes. Fig. 13 shows the tension of the mooring lines in various wave directions and various wavelengths, where the wave direction has a dominant effect on the mooring dynamics. The maximum tension of mooring lines occurs when the mooring lines are parallel to the wave propagation direction. The tension of the mooring lines increases significantly at low frequency in all wave directions.

4.2 Performance of the Optical Sensor in Irregular Waves

The significant value of the tension in irregular waves was considered in this study. The significant value of mooring tension was used to find the dominant value of tension that occurs. In addition, the significant value of tension is an important parameter for the statistical distribution of the mooring tension. This implies that the highest tension is not encountered too frequently. Moreover, when we know the significant value of tension, the range of tension can be determined. Fig. 14 shows the significant value of the mooring line's tension of the semi-submersible in various wave directions.

The significant value of OS#4 is slightly greater than that of TG#1

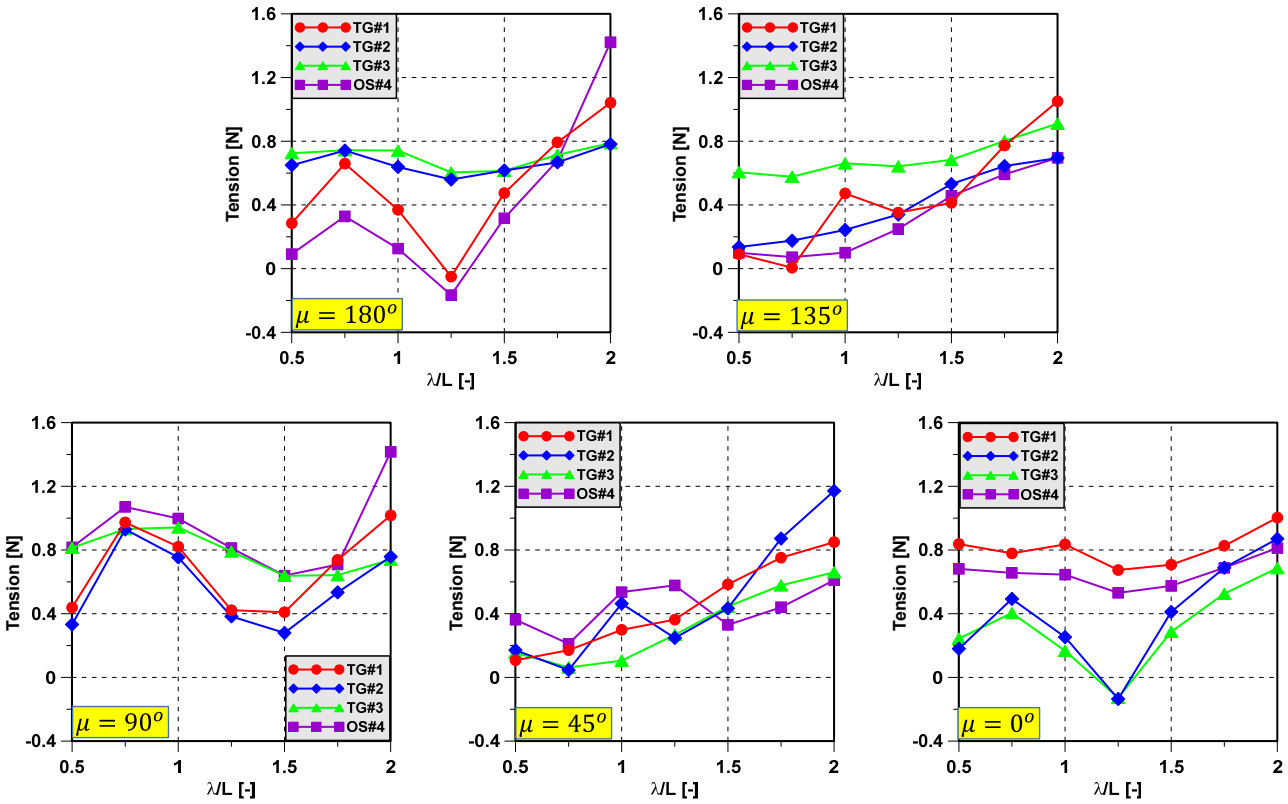

Fig. 12 Maximum tension of mooring lines of semi-submersible in various wave directions

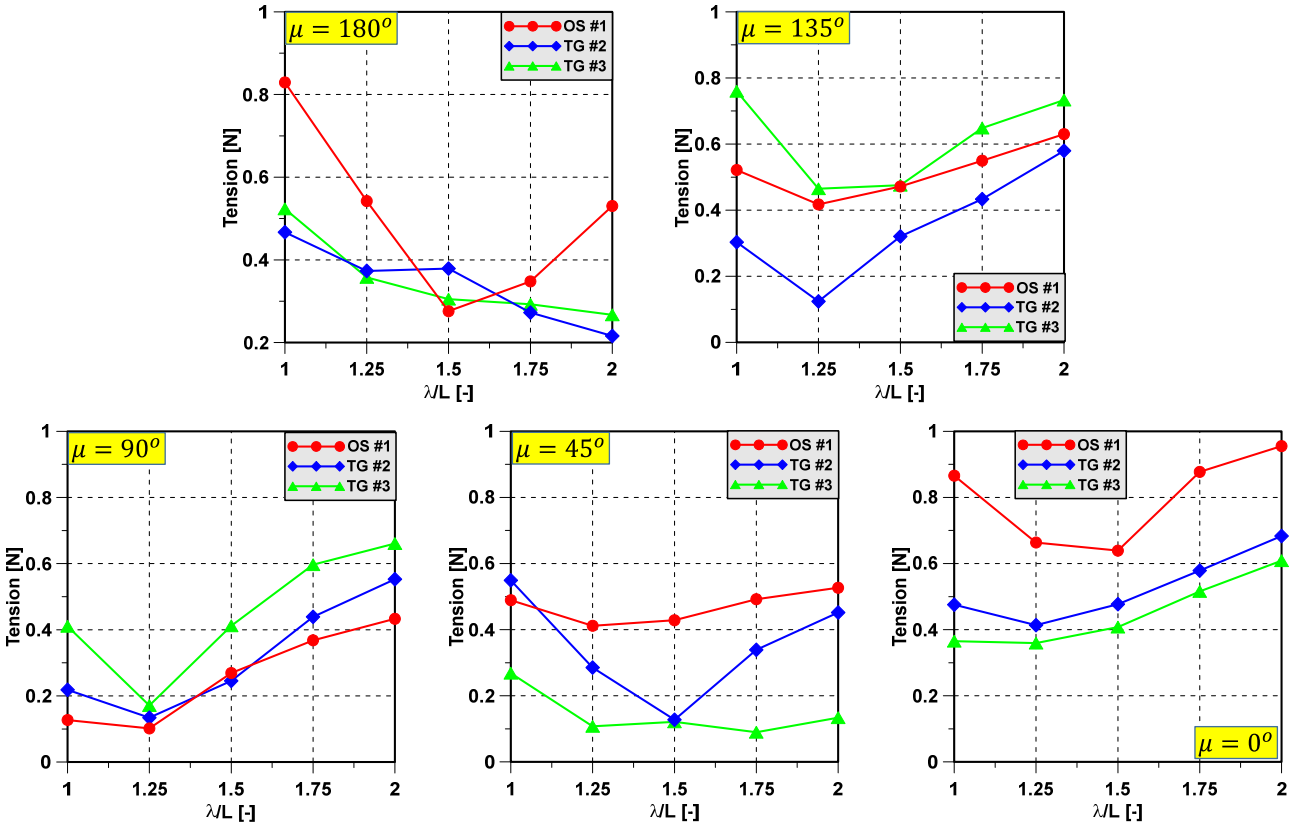

Fig. 13 Maximum tension of mooring lines of triangle platform in various wave directions

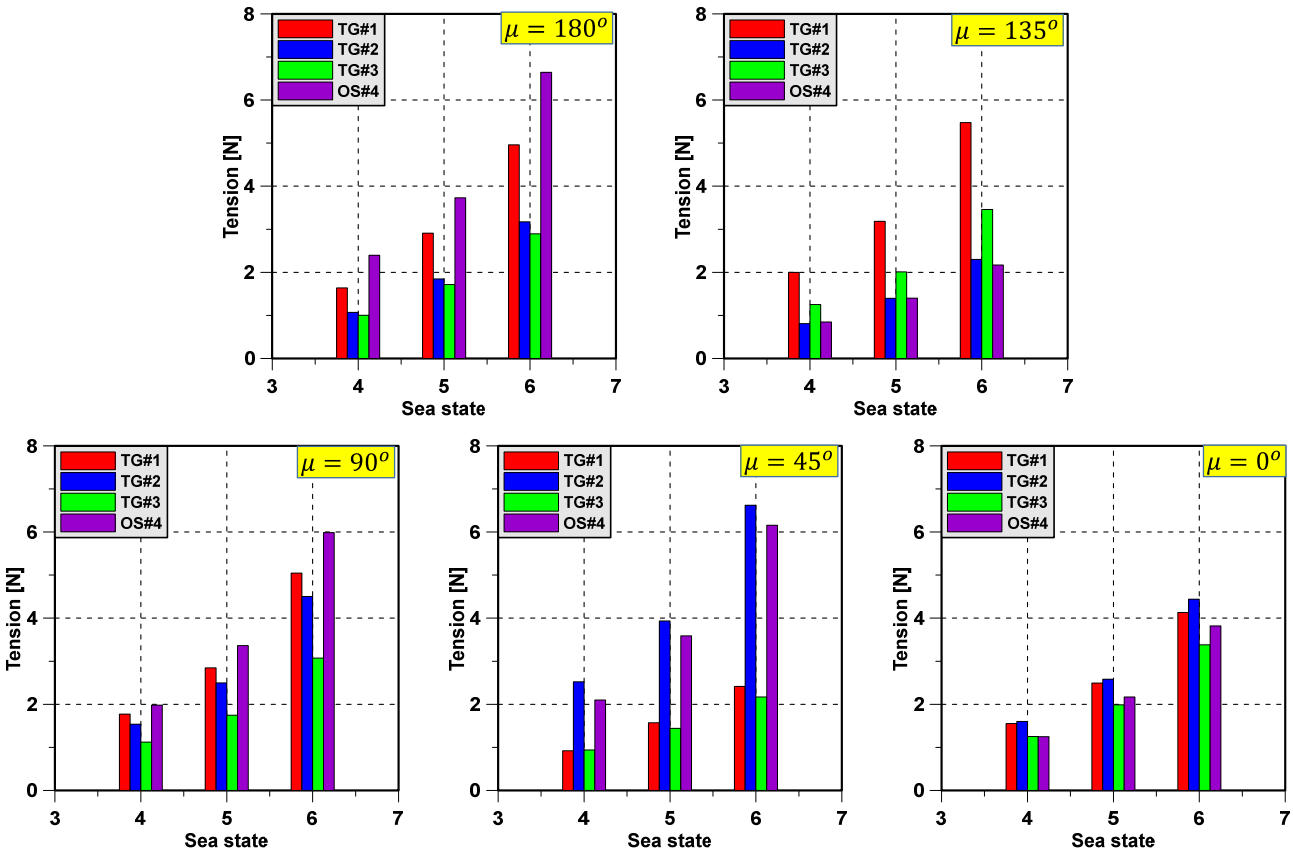

Fig. 14 Significant value of tension of mooring lines in case of semi-submersible in various wave directions

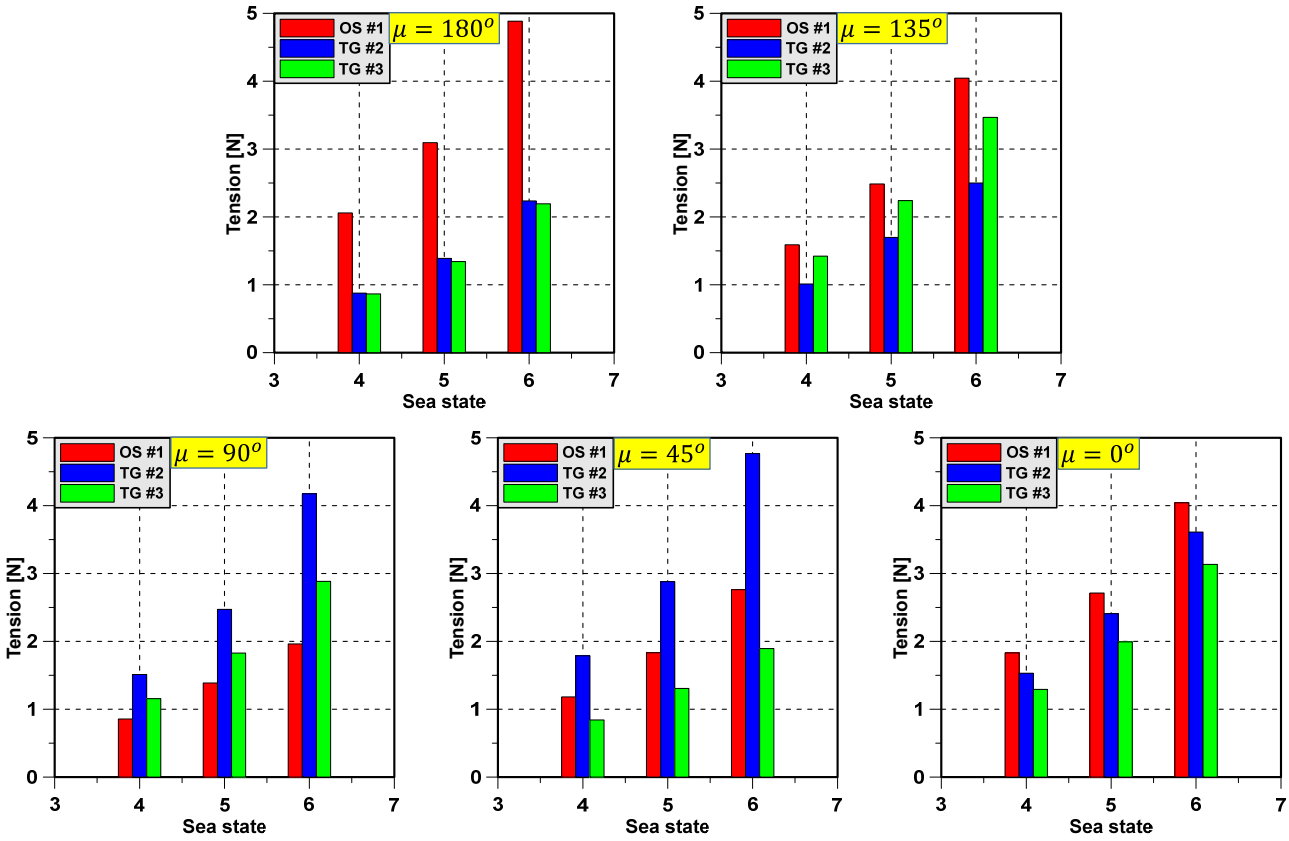

Fig. 15 Significant value of tension of mooring lines in case of triangle platform in various wave directions

in head sea. In the following sea, the significant values of OS#4 and TG#1 have a significant difference. TG#1 is dominant when the wave direction approaches 135 degrees. At that time, the significant values of TG#2 and OS#4 are the same and the smallest. TG#2 is dominant when the wave direction approaches 45 degrees. In this case, the significant values of TG#1 and TG#3 are the same due to the symmetric nature of the model test. Fig. 15 shows the significant value of the mooring line's tension of the triangle platform in various wave directions. The greatest significant value of mooring tension occurs when the mooring lines are parallel to the wave propagation direction. This happens because the wave direction has a direct effect on the motion response of the triangle platform. The extreme mooring tension depends on the type of sea state and wave direction.

5. Conclusion

In this study, experiments with semi-submersible and triangle platforms were carried out in the square wave tank at Changwon National University to investigate the tension of the mooring lines in various wave directions. An optical sensor was developed for estimating the tension of a mooring line. The concluding remarks are as follows.

First, the technical and operation details of the optical sensor were introduced. An optical sensor has several advantages in comparison with a conventional sensor due to light weight and small size.

Second, an experiment with a moored floating platform was performed to check the performance of the optical sensor. The optical sensor was effective in measuring the tension of the mooring lines.

Third, the maximum tension of the mooring lines was estimated to investigate the mooring dynamics due to the effect of the wave direction and wavelength in the regular waves. The maximum tension of mooring lines occurs when the mooring lines are parallel to the wave propagation direction. The tension of mooring lines increases significantly at low frequency in all wave directions.

Finally, the significant value of the mooring line's tension in various wave directions was estimated in irregular waves. The greatest significant value of mooring tension occurred when the mooring lines were parallel to the wave propagation direction. This happened because the wave direction has a direct effect on the motion response of the semi-submersible and triangle platforms. The extreme mooring tension depends on the type of sea state and wave direction.

Conflict of Interest

Hyeon Kyu Yoon serves as an editor of the Journal of Ocean Engineering and Technology but had no role in the decision to publish this article. No potential conflict of interest relevant to this article is reported.

Funding

This work was supported by the National Research Foundation of Korea (NRF) grant, which is funded by the Korean government (MSIT) (No. 2019R1F1A1057551).

References

Cevasco, D., Collu, M., Rizzo, C.M., & Hall, M. (2018). On Mooring Line Tension and Fatigue Prediction for Offshore Vertical Axis Wind Turbines: A Comparison of Lumped-mass and Quasi-static Approaches. Journal of Wind Engineering, 42(2), 97−107. https://doi.org/10.1177/0309524X18756962

Chung, J.C, Lee, M.M.S., & Kang, S.H. (2021). A Study of 100 tonf Tensile Load for SMART Mooring Line Monitoring System Considering Polymer Fiber Creep Characteristics. Journal of Ocean Engineering and Technology, 35(4), 266−272. https://doi.org/10.26748/KSOE.2021.009

Culshaw, B., & Kersey, A. (2008). Fiber-Optic Sensing: A Historical Perspective. Journal of Lightwave Technology, 26(9), 1064−1078. https://https://doi.org/10.1109/JLT.0082.921915

Jiang, C., Moctar, O., & Parades, G.M. (2020). Validation of a Dynamic Mooring Model Coupled with a RANS Solver. Marine Structures, 72, 102783. https://doi.org/10.1016/j.marstruc.2020.102783

Meltz, G., Morey, W.W., & Glenn, W.H. (1989). Formation of Bragg Gratings in Optical Fibers by Transverse Holographic Method. Optics Letters, 14(15), 823−825. https://doi.org/10.1364/OL.14.000823

Hill, K.O., & Meltz, G. (1997). Fiber Bragg Grating Technology Fundamentals and Overview. Journal of Lightwave Technology, 15(8), 1263−1276. https://doi.org/10.1109/50.618320

Lee, M., & Kim, H. (2011). Latest Development Status of FBG Sensors & Interrogator from Korea & Other Countries. Journal of Korean Society of Civil Engineers, 59, 84−90.

Kim, H.C., Kim, I., Kim, Y.Y., Youn, D.H., & Han, S. (2016). Simulation and Experimental Study of a TLP Type Floating Wind Turbine with Spoke Platform. Journal of Advanced Research in Ocean Engineering, 2(4), 179-191. https://doi.org/10.5574/JAROE.2016.2.4.179

Kim, M.H., Koo, B.J., Mercier R.M., & Ward, E.G. (2005). Vessel/Mooring/Riser Coupled Dynamic Analysis of a Turret-moored FPSO Compared with OTRC Experiment. Ocean Engineering, 32(14-15), 1780−1802. https://doi.org/10.1016/j.oceaneng.2004.12.013

Montasir, O.A., Yenduri, A., & Kurian, V.J. (2015). Effect of Mooring Line Configurations on the Dynamic Responses of Truss Spar Platforms. Ocean Engineering, 96, 161−172. https://doi.org/10.1016/j.oceaneng.2014.11.027

Natarajan, R., & Ganapathy, C. (1997). Model Experiments on Moored Ships. Ocean Engineering, 24(7), 665−676. https://doi.org/10.1016/S0029-8018(96)00006-6

Paduano, B., Giorgi, G., Gomes, R.P.G., Pasta, E., Henriques, J.C.C., Gato, L.M.C., & Mattiazzo, G. (2020). Experimental Validation and Comparison of Numerical Models for the Mooring System of a Floating Wave Energy Converter. Journal of Marine Science and Engineering, 8(8), 525. https://doi.org/10.3390/jmse8080565

Pan, W., Zhang, N., Huang, G., & Ma, X. (2018). Experimental Study on Motion Responses of a Moored Rectangular Cylinder under Freak Waves (I: Time-domain Study). Ocean Engineering, 153, 268−281. https://doi.org/10.1016/j.oceaneng.2018.01.084

Pan, W, Liang, C., Zhang, N., & Huang, G. (2021). Experimental Study on Hydrodynamic Characteristics of a Moored Square Cylinder under Freak Waves (II: Frequency-domain sSudy). Ocean Engineering, 219, 108452. https://doi.org/10.1016/j.oceaneng.2020.108452

Author ORCIDs

Author name	ORCID
Nguyen, Thi Thanh Diep	0000-0003-3521-6680
Park, Ji Won	0000-0001-8504-4747
Nguyen, Van Minh	0000-0002-0404-7952
Yoon, Hyeon Kyu	0000-0001-6639-0927
Jung, Joseph Chul	0000-0003-3240-0407
Lee, Michael Myung Sub	0000-0001-6483-7895

KSOE

Journal of Ocean Engineering and Technology 36(3), 161-167, June, 2022
https://doi.org/10.26748/KSOE.2022.008

pISSN 1225-0767
eISSN 2287-6715

Original Research Article

Shock-Resistance Responses of Frigate Equipments by Underwater Explosion

Hyunwoo Kim[1] and Joonmo Choung[2]

[1]*Graduate Student, Department of Naval Architecture and Ocean Engineering, Inha University, Incheon, Korea*
[2]*Professor, Department of Naval Architecture and Ocean Engineering, Inha University, Incheon, Korea*

KEY WORDS: UNDEX, Shock response, Acceleration, PVSS

ABSTRACT: *Three-dimensional finite element analysis (3D-FEA) models have been used to evaluate the shock-resistance responses of various equipments, including armaments mounted on a warship caused by underwater explosion (UNDEX). This paper aims to check the possibility of using one-dimensional (1D) FEA models for the shock-resistance responses. A frigate was chosen for the evaluation of the shock-resistance responses by the UNDEX. The frigate was divided into the thirteen discrete segments along the length of the ship. The 1D Timoshenko beam elements were used to model the frigate. The explosive charge mass and the stand-off distance were determined based on the ship length and the keel shock factor (KSF), respectively. The UNDEX pressure fields were generated using the Geers-Hunter doubly asymptotic model. The pseudo-velocity shock response spectrum (PVSS) for the 1D-FEA model (1D-PVSS) was calculated using the acceleration history at a concerned equipment position where the digital recursive filtering algorithm was used. The 1D-PVSS was compared with the 3D-PVSS that was taken from a reference, and a relatively good agreement was found. In addition, the 1D-PVSS was compared with the design criteria specified by the German Federal Armed forces, which is called the BV043. The 1D-PVSS was proven to be relatively reasonable, reducing the computing cost dramatically.*

1. Introduction

Among the many types of threats that occur during the battles of surface ships, the underwater explosion (UNDEX) causes structural and equipment damages and the even loss of the longitudinal strength of naval vessels. Therefore, in order to continue the battle and operational performance of naval ships, the shock-resistance against the UNDEX must be evaluated throughout the exploratory development stage and system development stage, respectively.

Naval ships are composed of hull structure, equipment, and crews. The shock-resistance evaluation is performed mainly on the most vulnerable installations and equipments. The shock-resistance responses for those installations and equipments are evaluated using experimental and numerical approaches. In general, the experimental method is recommended, but if there are experimental restrictions, such as the huge sizes, excessively heavy weights, and high costs, the computer-based numerical approach can be an alternative (BV, 1985).

The numerical approach includes the static acceleration method, the dynamic design analysis method (DDAM) suggested by the U.S. Naval Research Laboratory (NRL), and the BV043 method by the German Naval Regulations (BV, 1985).

Although the static acceleration method is relatively simple compared to other numerical methods, the Naval Sea System Command (NAVSEA) does not recommend to use it because it does not consider the dynamic responses. The DDAM evaluates the shock-resistances based on the spectral analyses (NAVSEA, 1995). The shock response spectrum (SRS) can be calculated using the BV043 based on the German Naval Regulations while the BV043 also provides the design criteria for the SRS. The BV043 provides guides to calculate the SRS depending on the installation locations of the equipments and the shock directions.

Lee and Choung (2020) confirmed that the fluid domain was not necessary condition to obtain the response history of the floating body subjected to the UNDEX loads. Kim et al. (2021) performed the inelastic whipping response analyses at the various stand-off distances using Timoshenko beam elements. Lee et al. (2010) applied the DDAM to analyze the shock responses of the large motors. Lee (2012) performed the shock-resistance response analyses of the ship steering system using the DDAM. Bae et al. (2009) and Seong et al. (2015) applied the BV043 to analyze the shock responses for the propulsion motor. Kim et al. (2017) evaluated the shock-resistance performance of the gas turbine package using the BV043.

Received 11 April 2022, revised 29 May 2022, accepted 13 June 2022
Corresponding author Joonmo Choung: +82-32-860-7346, heroeswise2@gmail.com

As can be seen from the reference surveys, the DDAM and BV043 methods have been used extensively to evaluate the shock-resistance performances of the equipments on naval ships.

After analyzing the 3-dimensional (3D) full ship shock responses, it is possible to evaluate the design integrity of the hull structures and equipment support structures. However, in the case of 3D full ship shock response analyses, it takes a considerable amount of time, hence it is often not possible to perform 3D full ship shock response analyses in the exploratory development stage. Therefore, the goal of this study was to check if the 1-dimensional (1D) shock response analysis model presents the reliable shock-resistance responses at the equipment supports.

The pseudo-velocity shock response spectrum (PVSS) obtained from the 1D shock response analysis (1D-PVSS) was compared with the PVSS of the 3D model (3D-PVSS). The 1D-PVSS was compared with the BV043 shock-resistance criteria. The effectiveness of the 1D model and the 1D-PVSS were validated.

2. Technical Background

2.1 UNDEX Model

When an explosion occurs in water, a primary shock wave faster than the speed of sound in water propagates from the source point, and a spherical gas bubble migrates to surface of the water, expanding and contracting repeatedly. Every time the gas bubble contracts to its minimum value, it spreads the strongest bubble pulse. (See Fig. 1.)

Geers and Hunter (2002) presented an UNDEX model that can consider the primary shock wave and the gas bubble wave in a single equation. The primary shock wave given in Eq. (1) that is a function of time t and stand-off distance R where the gas bubble volume acceleration $\ddot{V}$ is presented in Eq. (2).

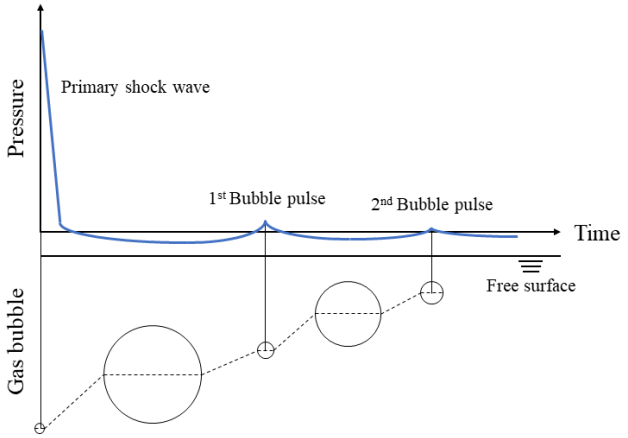

Fig. 1 Underwater explosion phenomenon

$$P(R,\,t)=\frac{\rho_l}{4\pi R}\left(\frac{a_c}{R}\right)^A \ddot{V}\left((a_c/R)^B t\right) \tag{1}$$

$$\ddot{V}(t)=\frac{4\pi a_c P_c}{\rho_l}\left\{0.8251\,e^{-1.338\,t/T_c}+0.1749e^{-0.1805\,t/T_c}\right\} \tag{2}$$

m_c : charge mass

a_c : initial radius of charge mass

ρ_l : water density

P_c : constants associated with initial pressure ($=K(\sqrt[3]{m_c}/a_c)^{1+A}$)

T_c : constants associated with initial time ($T_c=k\sqrt[3]{m_c}\left(a_c/\sqrt[3]{m_c}\right)^B$)

A, B, K, k : charge mass-dependent constant

Geers and Hunter (2002) presented an equation of motion with the radius, a, and vertical upward migration, u, of a gas bubble based on the doubly asymptotic approximation (DAA). The rates of the radius change and vertical displacement are given by Eqs. (3) and (4), respectively. In order to calculate the radius of the gas bubble and its migration, Eqs. (3) and (4) should be integrated with the seven initial conditions at $t_I=7T_c$. By integrating Eq. (2), the first condition of the initial radius of the gas bubble and second condition of the initial radial velocity of the gas bubble can be obtained. i.e., $a(t_I)=a_I=\dot{V}(t_I)/4\pi a^2(t_I)$ and $\dot{a}(t_I)=\dot{a}_I=\dot{V}(t_I)/4\pi a^2(t_I)$, respectively.

By combining Eqs. (3) and (5), the third condition, $\phi_{l0}(t_I)$, that is shown in Eq. (8) can be obtained. Similarly, Eqs. (4) and (7) produce the fourth condition of $\phi_{g1}(t_I)$, as given in Eq. (9). The fifth and sixth conditions are the initial location $u(t_I)=0$ and the initial velocity $\dot{u}(t_I)=0$. The last condition corresponds to the fluid potential $\phi_{l1}(t_I)=1/2(g/c_l)a_I^2$.

$$\dot{a}=-\frac{\phi_{l0}}{a}-\frac{1}{c_l}\left(\dot{\phi}_{l0}-\dot{a}^2-\frac{1}{3}\dot{u}^2-\frac{2}{3}\dot{u}\frac{\phi_{l1}}{a}\right) \tag{3}$$

$$\dot{u}=-2\frac{\phi_{l1}}{a}-\frac{1}{c_l}\left(\dot{\phi}_{l1}-2\dot{a}\dot{u}\right) \tag{4}$$

$$\dot{\phi}_{l0}=\frac{1}{1+\zeta}\left\{\left(\frac{1}{2}+\frac{1}{2}\frac{\rho_g}{\rho_l}+\zeta\right)\left(\dot{a}^2+\frac{1}{3}\dot{u}^2\right)-\frac{\rho_g}{\rho_l}c_g\frac{\phi_{l0}}{a}+\frac{2}{3}(1+\zeta)\dot{u}\frac{\phi_{l1}}{a}-Z\right\} \tag{5}$$

$$Z=\frac{1}{\rho_l}(P_g-p_I+\rho_l g u)+\frac{1}{3}\left\{\left(\frac{\phi_{l1}}{a}\right)^2-\frac{\rho_g}{\rho_l}\left(\frac{\phi_{g1}}{a}\right)^2\right\} \tag{6}$$

$$\dot{\phi}_{l1}=\frac{1}{1+\zeta}\left\{\left(1+\frac{\rho_g}{\rho_l}+2\zeta\right)\dot{a}\dot{u}-\left(1-\frac{\rho_g}{\rho_l}\right)ga-\frac{\rho_g}{\rho_l}c_g\left(2\frac{\phi_{l1}}{a}+\frac{\phi_{g1}}{a}\right)\right\} \tag{7}$$

$$\phi_{l0}(t_I)=-a_I\dot{a}\left\{1+\zeta_I-\frac{1}{2}\left(1-\frac{\rho_{gI}}{\rho_l}\right)\frac{\dot{a}_I}{c_l}\right\}+\frac{a_I}{c_l}Z_I \tag{8}$$

$$\phi_{g1}(t_I)=\frac{-1}{\zeta_I}\left(1-\frac{\rho_{gI}}{\rho_l}\right)\frac{g}{c_l}a_I^2 \tag{9}$$

ϕ_{l0} : fluid velocity potential corresp. to 3rd initial condition

ϕ_{l1} : fluid velocity potential corresp. to 4th initial condition

c_l : the speed of sound in the fluid
ϕ_{g1} : gas bubble potential
ρ_g : gas bubble density
P_g : gas bubble pressure constant ($=K_c(V_c/V)^{\gamma}$)
V_c : initial volume of the gas bubble
V : volume of gas the bubble
γ : specific heat ratio of the gas bubble
ζ : impedance ratio ($=\rho_g c_g/\rho_l c_l$)
K_c : adiabatic pressure constant
t_I : initial time
p_I : initial pressure at the source point ($=p_{atm}+\rho_l g d_I$)
d_I : initial depth of charge mass
p_{atm} : atmospheric pressure
g : gravitational constant0

The primary shock generated at the source point applies the impulsive pressure to the hull surface, while the bubble pressure field over space and time is estimated using the DAA model of Eq. (10). As shown in Eq. (11), the spatial pressure term, P_R, is determined using the stand-off distance, R, of Eq. (13), where $\boldsymbol{x_s}$ and $\boldsymbol{x_c}$ are the coordinates of the stand-off and charge points, respectively. The time pressure term, P_t, should be distinguished by the shock phases: the primary shock wave ($t_I \leqq 7T_c$) and the gas bubble wave ($t_I > 7T_c$). The charge constants are far smaller than unity, thus the stand-off distance has a minor effect for the primary shock wave phase, thus the stand-off distance may be often assumed to be constant.

$$P_I(R,\ t) = P_t P_R \tag{10}$$

$$P_R = \frac{1}{R} \tag{11}$$

$$P_t = \begin{cases} \dfrac{\rho_l}{4\pi}\left(\dfrac{a_c}{R}\right)^A \ddot{V}\left((a_c/R)^B t\right) & t_I \leqq 7T_c \\ \dfrac{\rho_l}{4\pi}\ddot{V}(t) = \rho_l(a^2\ddot{a}+2a\dot{a}^2) & t_I > 7T_c \end{cases} \tag{12}$$

$$R = \| \boldsymbol{x_c} - \boldsymbol{x_s} \| \tag{13}$$

2.2 Definition of PVSS

The SRS is given by a response chart to contain the maximum response at each frequency when an arbitrary shock load is applied to a single degree of freedom (SDOF) spring - mass - damper system, as depicted in Fig. 2. The acceleration is the input value for the SDOF system.

$$S_{pv} = 2\pi f_i \times S_d \tag{14}$$

According to the type of responses, a SRS is classified into an absolute acceleration type and a relative displacement type. The relative displacement type of Eq. (14) is used mainly for the shock-resistance design of naval ships. f_i and S_d in Eq. (14) are the

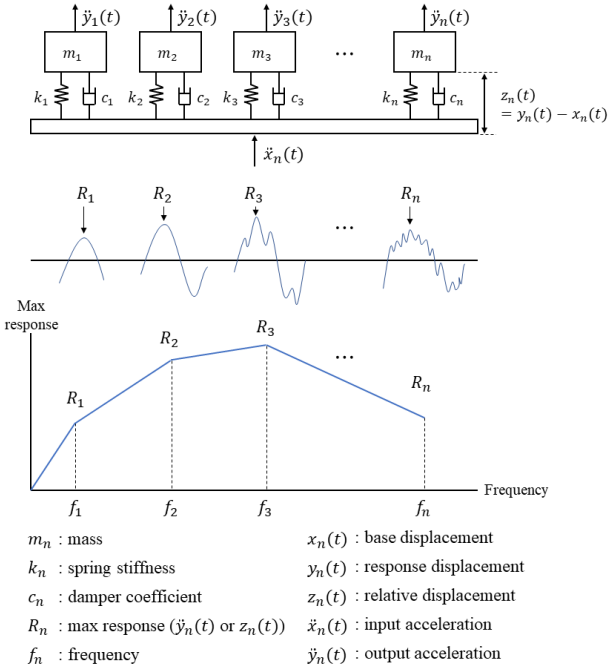

Fig. 2 Shock response spectrum

natural frequency and the SRS of the relative displacement, respectively. A PVSS, S_{pv}, can be calculated by multiplying the relative displacement for each frequency by the own frequency. The PVSS unit is the same as the units of velocity.

In this study, the digital recursive filter of Smallwood (1980) was used to calculate the relative displacement SRS. As shown in Eq. (15), the digital recursive filter is a transfer function, where $X(z)$ and $Y(z)$ are z transformations of the input acceleration $\ddot{x}(t)$ and the relative displacement response $z(t)$. The coefficients of b_0, b_1 and b_2 are dependent on the types of response, and they are determined using Eqs. (16), (17), and (18), respectively.

$$\tilde{H}(z) = \frac{Y(z)}{X(z)} = \frac{z[z(t)]}{z[\ddot{x}(t)]} = \frac{b_0 + b_1 z^{-1} + b_2 z^{-2}}{1 - 2Cz^{-1} + E^2 z^{-2}} \tag{15}$$

$$b_0 = \frac{1}{T\omega_n}\left[2\zeta(C-1) + \frac{(2\zeta^2-1)S}{\sqrt{1-\zeta^2}} + T\omega_n\right] \tag{16}$$

$$b_1 = \frac{1}{T\omega_n}\left[-2CT\omega_n + 2\zeta(1-E^2) - \frac{2(2\zeta^2-1)S}{\sqrt{1-\zeta^2}}\right] \tag{17}$$

$$b_2 = \frac{1}{T\omega_n}\left[E^2(T\omega_n + 2\zeta) - 2\zeta C + \frac{2(2\zeta^2-1)S}{\sqrt{1-\zeta^2}}\right] \tag{18}$$

T : sampling rate
ω_n : natural frequency
ω_d : damped natural frequency
ζ : critical damping ratio
E : sampling rate-dependent coefficient ($=e^{-\zeta\omega_n T}$)
C : sampling rate-dependent coefficient ($=E\cos T\omega_d$)
S : sampling rate-dependent coefficient ($=E\sin T\omega_d$)

2.3 PVSS Criteria

The BV043 specifies the PVSS criteria shown in Fig. 3, and they are dependent on the ship types (surface ships and submarines), ship displacements (less than 1,000 tons and larger than 2,000 tons), equipment locations (bottom, waterline, and above waterline), and the shock load directions (up/down, port/starboard, and stern/stem). There are three criteria of velocity, i.e. V_0, accleration A_0, and displacement D_0 in the BV043 criteria. Those criteria can be compared directly to the PVSS obtained through the experiments or numerical simulations. The BV043 specifies to use the standard shock accelerations of a half sine wave or a triangular wave, hence a consistent campaign of experiments has been possible.

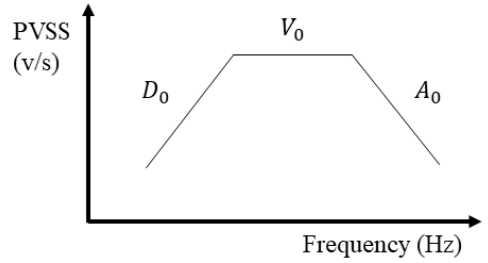

Fig. 3 PVSS criteria by BV043

3. UNDEX Shock Responses

3.1 UNDEX Conditions

A navy ship was chosen for the 1D and 3D shock response analyses with its main specifications summarized in Table 1. As shown in Eq. (19), a keel shock factor (KSF) is decided from the charge weight, w_c, stand-off distance, R, and wave incident angle, θ. In the case that the KSF is given, one of the unknows of charge mass, and incident angle, the stand-off distance can be determined.

The added mass $\triangle_a$ corresponding to the heave motion was determined from Eq. (20) based on a reference (ABS, 2021). Because the added mass is faily dependent on the hull form, more rigorous challeges are necessary to determine the added mass.

Table 1 Main dimensions of the naval ship

Item	Value
LOA L (m)	130.0
Breadth B (m)	15.0
Draft T (m)	4.5
Depth of main deck (m)	8.0
Displacement $\triangle$ (ton)	4,200.0
Added mass $\triangle_a$ (ton)	5,500.0
Young's modulus E (GPa)	206.0

$$KSF = \frac{\sqrt{w_c}}{R}\left(\frac{1+\sin\theta}{2}\right) \tag{19}$$

$$\triangle_a = (0.2 + B/3T)\triangle \tag{20}$$

Table 2 Charge properties of HBX-1

Item	Value	Item	Value
K	5.35E+7	g (m/s^2)	9.81
k	9.20E-5	p_{atm} (Pa)	101,325
A	0.144	c_l (m/s)	1,500
B	0.247	m_c (kg)	544.31
γ	1.35	ρ_c (kg/m^3)	1,720
K_c (Pa)	1.0E+9	ρ_l (kg/m^3)	1,025

NAVSEA (1976) recommended the charge mass and type as a function of the overall length of the ship. The overall length of 130 m produces w_c = 544.31 kg of the charge type HBX-1. The wave incident angle of θ = 90° was assumed to generate the worst UNDEX pressure field. With the charge mass, wave incident angle, and KSF, the stand-off distance of 43.1m was decided. The UNDEX model of Geers and Hunter (2002) was used to generate the primary and gas bubble pressure fields. The charge propeties are summarized in Table 2.

3.2 Analysis Models

3.2.1 1D model

As shown in Fig. 4, the overall ship length was divided into the eleven segments. There was a segment division where there are significant changes in the cross section areas or second moments of cross section areas. As shown in Table 3, it was assumed that each segment has a uniform cross section property along the segment length. The cross sectional area and the second moment of the cross sectional area were normalized by each maxima.

The 1D model for the UNDEX shock response analyses was generated with the Timoshenko beam elements without any fluid domain. The product of the elastic modulus and the cross section area was defined manually as the axial stiffness of the beam elements, while the vertical bending stiffness was the product of the elastic modulus and the second moment of the cross sectional area. The mass density of the steel hull was modified so that the total displacement included the added mass. There were no boundary conditions on the UNDEX model.

The BV043 specifies that a PVSS should be calculated for the frequency range of 3−500 Hz. The sampling rate should be over 10 times of the minimum period to avoid any probable distortion of the shock acceleration to use the PVSS input value (Scavuzzo and Pusey, 1996). The sampling rate corresponding to 10 times the maximum period was 2.00E-04 seconds.

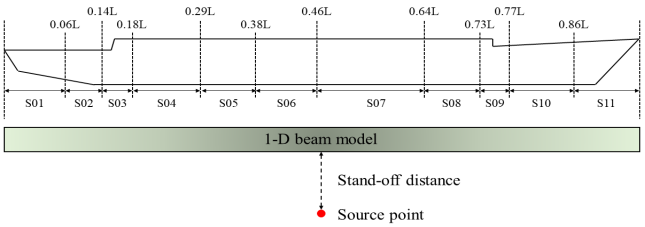

Fig. 4 1D model segments

Table 3 Section properties of the target ship

Segment	Range (x L)		Normalized cross section area	Normalized 2nd moment of area
	from	to		
1	0.00	0.06	0.60	0.07
2	0.06	0.14	0.62	0.27
3	0.14	0.18	0.90	0.83
4	0.18	0.29	0.87	1.03
5	0.29	0.38	0.88	1.06
6	0.38	0.46	0.95	1.04
7	0.46	0.64	1.00	1.00
8	0.64	0.73	0.91	0.92
9	0.73	0.77	0.52	0.24
10	0.77	0.86	0.48	0.27
11	0.86	1.00	0.38	0.23

The time increment to be used in the shock response analyses should be less than the sampling rate. The time increment of the finite element analysis is determined by Eqs. (21)–(22) (Simulia, 2018) where the time increment is controlled by the sound speed in the medium and the element length. Since the density of the analytical model, elastic modulus, and Poisson ratio have been already determined, the time increments smaller than the sampling rate can be obtained by reducing the size of the element.

$$\triangle t = \frac{l_e}{c_s} \tag{21}$$

$$c_s = \sqrt{\frac{E}{\rho_s (1-\nu^2)}} \tag{22}$$

$\triangle t$: time increment
l_e : minimum element length
c_s : sound speed in hull steel
ρ_s : density of hull steel
ν : Poisson ratio of hull steel

Table 4 shows the time increment according to the length of the beam element. When the length of the element was less than 1,000 mm, the time increment was smaller than the sampling rate of 2.00E-04 seconds. Therefore, an element length of 1,000 mm was applied to the 1D analysis model.

Table 4 Time increment according to element length

l_e (mm)	$\triangle t$ (s)	Frequency (Hz)
1300.00	2.41E-04	4146.10
1181.82	2.19E-04	4560.72
1083.33	2.01E-04	4975.33
1000.00	1.86E-04	5389.94
928.57	1.72E-04	5804.55
866.67	1.61E-04	6219.17

3.2.2 3D model

The 3D analysis was not conducted in this study, and the analysis information is just provided. The 3D analysis model is composed of shell elements and beam elements that constitute the hull and acoustic elements, respectively, to transmit the UNDEX loads. (See Fig. 5.) The total displacement was achieved by adjusting the density of the elements because the various weapon systems, engines, and supplies were not included in the 3D model. Mass elements were distributed uniformly over the length of the ship to realize the added mass.

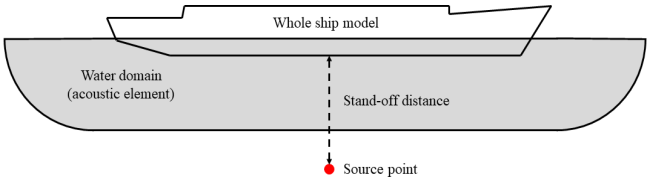

Fig. 5 Schematic of the 3D analysis model

3.3 Shock Response Analysis Results

3.3.1 Comparison between 1D-PVSS and 3D-PVSS

The 1D shock response analysis was performed up to 0.5 seconds. The vertical acceleration history was taken at the position of 0.64L where the propulsion motor was installed. Based on the acceleration, the 1D-PVSS was calculated at 1 Hz intervals in the frequency range of 3–500 Hz, and Fig. 6 shows the results. Although the 1D-PVSS and 3D-PVSS show a difference that cannot be neglected, it was confirmed that the overall PVSS patterns were similar. Therefore, the 1D-PVSS was judged to be relatively reliable. The very short computing duration of 426 seconds was necessary for the 1D shock response analysis, while the 3D shock response analysis took several hours. Therefore, a relatively reasonable 1D-PVSS can be estimated in the exploratory development phase of a naval ship.

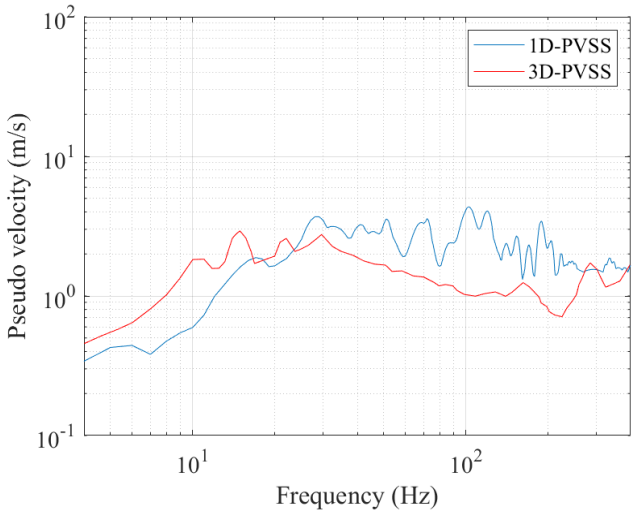

Fig. 6 Comparison of 1D-PVSS and 3D-PVSS

3.3.2 Comparison between 1D-PVSS and the design criteria

The 1D-PVSS and BV043 design criteria were compared to review the integrity of the shock response design. The conditions in Table 5 were applied to the BV043 to determine the shock response criteria. The PVSS criteria and 1D-PVSS are shown simultaneously in Fig. 7. The 1D-PVSS is within the design criteria in the 3–200 Hz frequency range but it exceeds the design criteria after 200 Hz.

Nevertheless, the 1D-PVSS has not been used even for the exploratory development phase because the local stiffnesses of the hull and elastic mounting system were not included in the 1D model. The introduction of some advanced numerical simulation techniques can improve the reliability of the 1D-PVSS. For example, if the global-local interaction technique is used, it is possible to improve the accuracy of the 1D-PVSS sufficiently. After the construction of a local 3D model with detailed mounting structures, the displacements obtained from the 1D model are used to prescribe the boundary conditions of the local 3D model. It is possible to obtain the 3D-PVSS, including the local stiffness effects without modeling of the full ship.

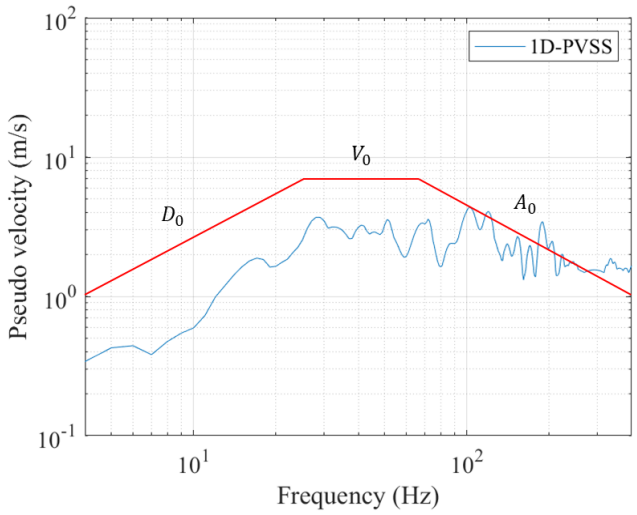

Fig. 7 Comparison between 1D-PVSS and the design criteria

Table 5 shock-resistance criteria by BV043

Mounting location	D_0 (mm)	V_0 (m/s)	A_0 (m/s^2)
Hull mounting	45	7.0	2,820

4. Conclusions

In this study, the shock response analysis by the underwater explosion was performed on the 1D model with the charge mass and stand-off distance according to the U.S. Navy's standards and regulations.

Based on the results of the analysis, the 1D-PVSS was derived and compared with the 3D-PVSS. There was a relatively consistent agreement at low frequencies, but a non-negligible difference occurred at high frequencies. This difference was estimated to be because the 3D model included the local stiffness of the equipment mount. Considering that the full ship 1D model requires less cost for modeling than the full ship 3D model and takes less time to analyze the shock responses, the full ship 1D model is predicted to show relatively good efficiency. As a result of comparing the 1D-PVSS and BV043 design criteria, the 1D-PVSS was out of the design criteria in the high frequency range of 200 Hz or higher. If the 1D model is applied in the exploratory development stage where the hull and equipment specifications are still under consideration, an evaluation of relatively quick and reasonabe shock-resistances is possible.

Because 1D models do not include local hull stiffness and elastic mount stiffness, only 3D models have been used even in the exploratory development stage. The 1D model-based PVSS can be improved by the introduction of a new numerical technique.

Authors' Contributions

Conceptualization, J.C.; methodology, J.C. and H.K.; software, H.K.; validation, J.C. and H.K; formal analysis, J.C. and H.K.; investigation, J.C. and H.K.; resources, J.C. and H.K.; writing original draft preparation, H.K.; writing review and editing, J.C.; visualization, H.K.; supervision, J.C.; project administration, J.C.; funding acquisition, J.C. All authors have read and agreed to the published version of the manuscript.

Conflict of Interest

Joonmo Choung serves as an editor in chief of the Journal of Ocean Engineering and Technology, but he had no role in the decision to publish this article. No potential conflict of interest relevant to this article was reported.

Funding

This work was supported by the Korea Environment Industry & Technology Institute which is funded by the Korea Ministry of Environment (No. 146836) and by the Korea Energy Technology Evaluation and Planning funded by the Ministry of Trade, Industry and Energy of Korea (No. 20213000000030).

References

American Bureau of Shipping (ABS). (2021). Guidance Notes on Ship Vibration. New York, USA: ABS.

Building Specification for Ships of the Federal Armed Forces (BV). (1985). Shock Resistance Experimental and Mathematical Proof (BV043).

Bae, S.W., Hong, J.S., Jeong, W.B., & Kim, J. (2009). Structural Safety Analysis of Propulsion Motors by BV043. Proceedings of the Korean Society for Noise and Vibration Engineering Conference, 254–255.

Geers, T.L., & Hunter, K.S. (2002). An Integrated Wave-Effects

Model for an Underwater Explosion Bubble. Journal of Acoustic Society of America, 111(4), 1584−1601. https://doi.org/10.1121/1.1458590

Kim, J.B., Park, Y.K., Park, M.S., Lee, J.H., & An, S.C. (2017). Evaluation of the Shock Resistance of a Gas Turbine Package. Transactions of the Korean Society of Mechanical Engineers A, 41(10), 1005−1009. https://doi.org/10.3795/KSME-A.2017.41.10.1005

Kim, H., Seo, J.H., & Choung, J. (2021). A Study on Inelastic Whipping Responses in a Navy Ship by Underwater Explosion. Journal of the Society of Naval Architects of Korea, 58(6), 400−406. https://doi.org/10.3744/SNAK.2021.58.6.400

Lee, S.W., Kim, J., & Kong, Y.K. (2010). A Shock-Proof Evaluation of a Naval Vessel Motor using DDAM and Transient Response Analysis. Journal of the Korean Society of Manufacturing Process Engineers, 9(5), 76−82.

Lee, J.B. (2012). A Study on Shock Resistance Evaluation of Steering Units for a War Vessel byUusing Dynamic Design Analysis Method (Master thesis). Changwon National University, Changwon, Korea.

Lee, J.B., & Choung, J. (2020). A Study on BEM-Based Numerical Simulation Technique for Underwater Explosions. Journal of the Society of Naval Architects of Korea, 57(5), 271−277.

Naval Sea System Command (NAVSEA). (1976). Test Plan for Routine Shock Testing of Ships. Washington, DC: NAVSEA.

Naval Sea System Command (NAVSEA). (1995). Shock Design Criteria for Surface Ships. Washington, DC: NAVSEA.

Scavuzzo, R.J., & Pusey, H.C. (1996). Principles and Techniques of Shock Data Analysis. Virginia: Booz Allen Hamilton.

Seong, J., Choi, J., Kim, J., & Baek, S. (2015). A Study on Shock Resistance Evaluation of Equipment for a Naval Ship by Using BV-043. The Korean Society of Mechanical Engineers, 1361−1366.

Simulia. (2018). Abaqus User Manual. Providence, RI: Dassault Systemes Simulia Corp.

Smallwood, D.O. (1980). An Improved Recursive Formula for Calculating Shock Response Spectra. Shock and Vibration Bulletin, 51(2), 211−217.

Author ORCIDs

Author name	ORCID
Kim, Hyunwoo	0000-0002-4333-8541
Choung, Joonmo	0000-0003-1407-9031

KSOE

Journal of Ocean Engineering and Technology 36(3), 168-180, June, 2022
https://doi.org/10.26748/KSOE.2022.006

pISSN 1225-0767
eISSN 2287-6715

Original Research Article

Onboard CO_2 Capture Process Design using Rigorous Rate-based Model

Jongyeon Jung[1] and Yutaek Seo[2]

[1]*Graduate student, Department of Naval Architecture and Ocean Engineering, Seoul National University, Korea*
[2]*Professor, Department of Naval Architecture and Ocean Engineering, Seoul National University, Korea*

KEY WORDS: On board carbon capture, MEA carbon capture process MEA, Rate based model, Process design

ABSTRACT: *The IMO has decided to proceed with the early introduction of EEDI Phase 3, a CO_2 emission regulation to prevent global warming. Measures to reduce CO_2 emissions for ships that can be applied immediately are required to achieve CO_2 reduction. We set six different CO_2 emission scenarios according to the type of ship and fuel, and designed a monoethanolamine-based CO_2 capture process for ships using a rate-based model of Aspen Plus v10. The simulation model using Aspen Plus was validated using pilot plant operation data. A ship inevitably tilts during operation, and the performance of a tilted column decreases as its height increases. When configuring the conventional CO_2 capture process, we considered that the required column heights were so high that performance degradation was unavoidable when the process was implemented on a ship. We applied a parallel column concept to lower the column height and to enable easy installation and operation on a ship. Simulations of the parallel column confirmed that the required column height was lowered to less than 3 TEU (7.8 m).*

1. Introduction

Efforts to respond to climate change are spreading to all industries around the world. In 2015, the Paris Agreement was adopted, aiming toward worldwide efforts to keep the global average temperature rise below 2 °C above the pre-industrial level and further limit the future temperature rise to below 1.5 °C (Bodansky, 2016). To implement this, the International Maritime Organization (IMO) has established and implemented regulations to reduce greenhouse gas (GHG) emissions from ships. According to the third IMO GHG study, CO_2 emitted from ships worldwide in 2012 accounted for 2.2% of the total CO_2 emissions (IMO, 2014). This exceeds the CO_2 emissions of Germany, Canada, and Korea (Olivier et al., 2017). According to the fourth IMO GHG study, CO_2 emitted from ships worldwide in 2018 accounted for 2.89% of the total CO_2 emissions, showing an increasing trend of the proportion of CO_2 emissions from ships. To respond to this, the 2019 Marine Environment Protection Committee (MEPC) 74 determined the introduction time of the Energy Efficiency Design Index (EEDI) Phase 3. The EEDI is an operational efficiency indicator for ships and refers to the CO_2 emission when 1 ton of a ship operates for 1 sea mile (1.852 km). The EEDI Phase 3 requires a reduction of 30% or more of CO_2 emissions from ships from 2025 to 2030 compared with 2008, and Phase 4, which will be applied after 2030, requires a CO_2 reduction of more than 40%. However, the MEPC 75 in 2020 proposed to reinforce emission regulations. Accordingly, part of the EEDI Phase 3, which was originally scheduled to be introduced in 2025, was moved forward to 2022.

Various methods are being devised to reduce GHGs emitted from ships to achieve the IMO's CO_2 emission reduction strategy. According to DNV-GL (2017), the main CO_2 reduction methods that have been attempted so far are classified into the following four categories: liquefied natural gas (LNG) with the use of alternative fuels e.g., hydrogen, increased energy efficiency, the reduction of navigation speed, and carbon pricing. Among alternative fuels, LNG is a representative fuel, and extensive reviews have been reported on liquefied petroleum gas, biodiesel, bio methanol, liquefied biogas, hydrogen, and nuclear power. Methods to increase energy efficiency include the development of a new hull form, recycling waste heat, engine overhaul, the development of a hybrid engine, and main engine air lubrication. Combining all these methods can achieve fuel savings of 21% to 37% per ship (Kristensen, 2012). The energy efficiency improvement of ships will continue to rise gradually until 2050 considering improvement measures, such as hull form improvement, the optimization of ship speed and operation, propulsion system, and

Received 15 March 2022, revised 5 June 2022, accepted 8 June 2022
Corresponding author Yutaek Seo: +82-2-880-7329, yutaek.seo@snu.ac.kr

low/zero-carbon fuels. However, from an operational point of view, the energy efficiency improvement is expected to peak in 2035, and carbon reduction by alternative fuels will dominate afterward (DNV-GL, 2018). Excluding alternative fuels, it is estimated that 20%–30% of current CO_2 emissions can be reduced by currently applicable technical and operational measures. In the future, carbon reduction by alternative fuels, such as hydrogen, ammonia, and biodiesel, should be promoted. However, developing and applying related technologies are currently challenging tasks, and the corresponding infrastructure is also insufficient. Therefore, as the effective date of the EEDI Phase 3 has been partially advanced to 2022, an onboard CO_2 capture technology that can be applied immediately is required to achieve the target CO_2 emission reduction.

Several researchers have studied onboard CO_2 capture technology in various ways. Zhou and Wang (2014) proposed a method for capturing and fixing CO_2 as calcium carbonate using calcium hydroxide solution and sodium hydroxide. This method was applied to a bulk carrier with an 18,660 kW engine, and the effectiveness and economic feasibility were evaluated. Luo and Wang (2017) simulated the monoethanolamine (MEA)-based post-combustion CO_2 capture process and the CO_2 storage liquefaction process for a cargo ship with a 17 MW engine. They observed that the carbon reduction rate could only reach 73% when conventional marine energy systems were integrated with the CO_2 capture process owing to the limited heat and electricity supply to the CO_2 capture process. They also observed that the cost of CO_2 capture more than doubled when an additional gas turbine was installed to achieve a carbon reduction rate of 90%. Feenstra et al. (2019) simulated the CO_2 capture process based on MEA and piperazine (PZ) using Aspen Plus for 1,280 kW and 3,000 kW class marine engines. Furthermore, they calculated the capital expenditure and operating expenditure required to capture CO_2 from ship exhaust gas through the process and suggested the addition of a CO_2 capture process and a CO_2 storage tank to the existing cargo ship design. Lee et al. (2021) proposed a new EEDI estimation method considering the CO_2 capture process and applied it to a 53,200 DWT class ship. They simulated the N-methyldiethanolamine- and PZ-based CO_2 capture process and the liquefaction process of the captured CO_2 using Aspen Plus and considered a design that placed a liquefied CO_2 storage tank on a ship. The calculation results confirmed that the carbon capture ratio required in the CO_2 capture process was higher than the actual EEDI reduction rate.

2. Process Model Framework

2.1 Rate-based Model

In this study, the CO_2 capture process based on an MEA solution was simulated using Aspen Plus v10, a commercial process simulator. Moreover, simulation was performed using a rate-based model for better accuracy. The conventional equilibrium model commonly used for distillation column simulation assumes that gas and liquid phases reach complete equilibrium at each stage and adjusts the performance

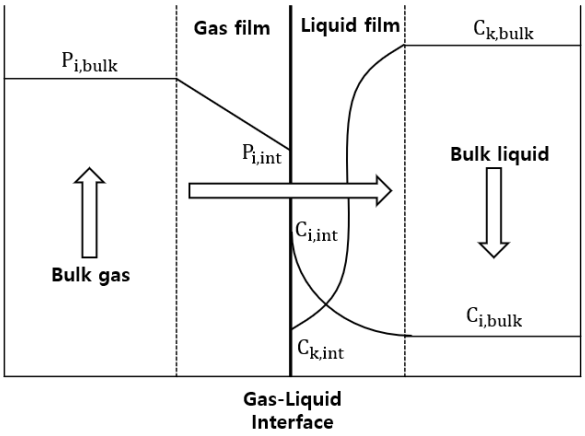

Fig. 1 Schematic of the behaviors of the liquid and gas phases of the inner stage of the absorber through the film theory

of the distillation column by introducing an efficiency correction factor in each phase. However, such perfect gas-phase and liquid-phase equilibrium states are rare in actual processes. In contrast, the rate-based model assumes that there are several layers of thin film at the gas–liquid interface according to the film theory as shown in Fig. 1. The Maxwell–Stefan equation is calculated for this thin film to actualize the realistic heat and mass transfer process at the gas–liquid interface (Al-Baghli, 2001). Through this process, the rate-based model can more closely simulate the chemical reaction in the actual tray column or packed column. When simulating processes with active chemical reactions, such as the CO_2 capture process using amines, the rate-based model shows higher reproducibility than the equilibrium model (Zhang and Chen, 2013).

2.2 Thermodynamic Model

Chemical reactions in the liquid phase must be considered to simulate the chemical equilibrium between gas and liquid accurately. The CO_2 capture process using amines shows a nonideal behavior owing to its own chemical reaction and ions participating in the reaction. The electrolyte nonrandom two-liquid Redlich–Kwong state equation model was used to simulate the activity coefficient, Gibbs energy, enthalpy, and entropy of the liquid phase. Furthermore, the fugacity coefficient of the weather (Agbonghae et al., 2014) was simulated using the perturbed-chain statistical associating fluid theory model. The CO_2 absorption reaction using MEA is expressed by the equilibrium equations Eqs. (1)–(5) below.

$$2H_2O \leftrightarrow H_3O^+ + OH^- \quad (1)$$

$$2H_2O + CO_2 \leftrightarrow HCO_3^- + H_3O^+ \quad (2)$$

$$H_2O + HCO_3^- \leftrightarrow CO_3^{2-} + H_3O^+ \quad (3)$$

$$MEAH^+ + H_2O \leftrightarrow MEA + H_3O^+ \quad (4)$$

$$MEACOO^- + H_2O \leftrightarrow MEA + HCO_3^- \quad (5)$$

2.3 Reaction Kinetic Model

In Aspen Plus, the reaction rate r_j of a chemical reaction is expressed using a power law as follows:

$$r_j = k_j^0 \exp\left(-\frac{\epsilon_j}{R}\left[\frac{1}{T}-\frac{1}{298.15}\right]\right)\prod_{i=1}^{N} a_i^{\alpha_{ij}} \quad (6)$$

where r_j is the reaction rate of the chemical reaction, k_j^0 is the pre-exponential factor, ϵ_j is the activation energy, R is the gas constant, T is the absolute temperature of the system, a_i is the activity coefficient, and α_{ij} is the reaction order.

The chemical reaction equations of carbamate and bicarbonate formed by the CO_2 absorption reaction using MEA are shown in Eqs. (7)–(10).

$$MEA + CO_2 + H_2O \leftrightarrow MEACOO^- + H_3O^+ \quad (7)$$

$$MEACOO^- + H_3O^+ \leftrightarrow MEA + CO_2 + H_2O \quad (8)$$

$$CO_2 + OH^- \leftrightarrow HCO_3^- \quad (9)$$

$$HCO_3^- \leftrightarrow CO_2 + OH^- \quad (10)$$

Zhang et al. (2009) converted the molarity-based speed constant to activation-based speed constant through the experimental data of Hikita et al. (1979) and Pinsent et al. (1956). Therefore, the calculation method of the equilibrium constant is based on "mole gamma." This result is summarized in Table 1.

Table 1 Reaction rates and pre-exponential factors for the absorption of CO_2 using MEA

Related species	Reaction Direction	k_j^0 (kmol/m^{3}s)	ϵ_j (kJ/mol)
$MEACOO^-$	Forward	3.02×10^{14}	41.20
	Reverse (absorber, 303–353K)	5.52×10^{23}	69.05
	Reverse (stripper, 363–393K)	6.56×10^{27}	95.24
HCO_3^-	Forward	1.33×10^{17}	55.38
	Reverse	6.63×10^{16}	107.24

3. Validation of Process Simulation

3.1 Target Plant for Simulation Validation

The CO_2 capture process was simulated based on pilot plant operational data (Stec et al., 2015) to validate the process simulation prior to simulating the onboard CO_2 capture process. The pilot plant to be verified implements a post-combustion carbon capture process based on a 30 wt% MEA solution. Table 2 lists the physical quantities and composition of the acid gas, Table 3 lists the physical quantities of the aqueous amine solution, and Table 4 lists the detailed operating characteristics of the absorber and stripper. The acid gas contains 13.5 mol% of CO_2, and the flow rate can be changed in the range of 200–400 kg/h. The absorber is a packed column with a diameter of 0.33 m and a height of 5.1 m filled with Sulzer Mellapak 500Y and 750Y. The stripper is a packed column with a diameter of 0.28 m and a height of 4.3 m filled with Sulzer Mellapak 750Y. The pilot plant was operated by applying various process improvement methods. The process simulation was validated using the amine process operation data of the most popular standard method.

Table 2 Properties of the acid gas for the pilot plant

Acid gas properties		
Pressure	(bar)	1.05
	(kPa)	206.3
Temperature (℃)		45
Flow rate (kg/h)		289
Compositions (mol fraction)		
CO_2		0.135
H_2O		0.055
N_2		0.7
O_2		0.11

Table 3 Properties of lean solvent for pilot plant

Properties of lean MEA solvent		
Pressure	(bar)	2.0
	(kPa)	301.3
Temperature (℃)		40
Flow rate (kg/h)		1358.3
MEA concentration (wt%)		30
CO_2 loading (mol CO_2/mol MEA)		0.36

Table 4 Specifications of columns

	Absorber	Stripper
Diameter (mm)	330	280
Height (mm)	8400	4300
Segment number	20	20
Packing type	Sulzer Mellapak 500Y, 750Y	Sulzer Mellapak 750Y
Reboiler temperature (℃)	-	108

3.2 Result of Simulation Validation

Various correction coefficients, correlation coefficients, and correlation methods of the rate-based model should be carefully selected and adjusted to construct a realistic process model that simulates real chemical reactions well. Table 5 summarizes the main tunable parameters and correlation method of the Aspen Plus rate-based model used to simulate pilot plant operation data. According to Zhang et al. (2009), when the Onda correlation method

Table 5 Design parameters of the columns

		Absorber	Stripper
Global tuning factors	Reaction condition factor	0.9	0.9
	Film discretization ratio	5	5
	Flow model	Vplug	Vplug
	Interfacial area	1.4	1.1
Liquid phase	Film resistance	Discretize film	Discretize film
	Number of discretization points	5	5
	Liquid holdup	Stichlmair89	Stichlmair89
Vapor phase	Film resistance	Consider film	Consider film
	Mass transfer coefficient	Brf-85	Brf-85
Correlation methods	Heat transfer coefficient	Chilton and Colburn	Chilton and Colburn
	Interfacial area	Brf-85	Brf-85

Table 6 Operating conditions of columns

		Pilot plant	Aspen Plus model
Absorber	Diameter (mm)	330	330
	Height (mm)	8400	8400
Stripper	Diameter (mm)	280	280
	Height (mm)	4300	4300
Lean solvent loading	mol CO_2/mol MEA	0.36	0.36
Rich solvent loading	mol CO_2/mol MEA	0.50	0.503
CO_2 removal rate	%	84	86.1
Stripper reboiler duty	GJ/t CO_2	3.98	4.05
Stripper reboiler temperature	℃	108	108

(Onda et al., 1968) is used, there is a possibility of underestimating the interfacial area. Therefore, the Bravo correlation method (Bravo et al., 1985) was used instead of the Onda correlation method which is generally used as the interfacial area method and mass transfer coefficient method. (Agbonghae et al., 2014). The Stichlmair method (Stichlmair et al., 1989) was used for liquid holdup, and the heat transfer coefficient was used by the Chilton and Colburn method (Chilton and Colburn, 1934). According to Zhang et al. (2009), the prediction accuracy of the countercurrent flow model is the highest, but this model requires a large number of calculations and sometimes shows unstable calculation results. Therefore, the Vplug flow model, which produces stable results, was used.

Table 6 lists the simulation results based on the configuration of the Aspen Plus model described above in comparison with the pilot data. Fig. 2 compares the temperature profile inside the actual pilot plant absorber with that of the simulation. The temperature decrease at the fourth stage of the pilot plant absorber could not be simulated. However, it can be seen that the maximum temperature bulge of 7th to 9th stages formed by the CO_2 absorption reaction of the amine aqueous solution and the overall temperature trend were well simulated. From the above results, it can be confirmed that the simulation method predict the actual data from pilot-plant very well.

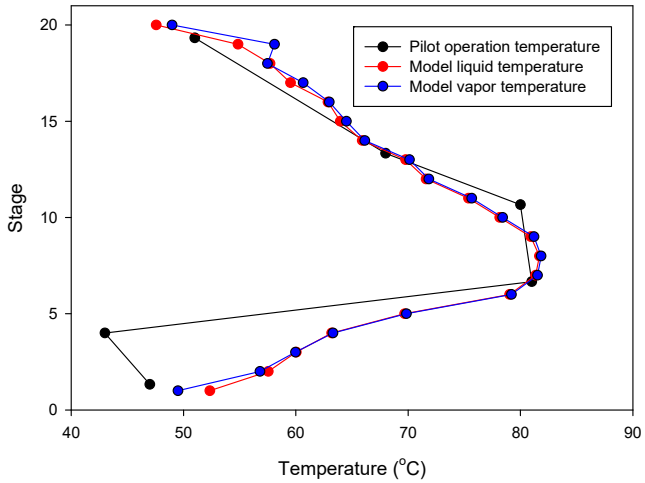

Fig. 2 Absorber temperature profile of the pilot plant

4. Simulation Result of Onboard Carbon Capture Process

4.1 Selection of Onboard CO_2 Emission Scenarios

The EEDI is an efficiency indicator determined as follows. First, the CO_2 emissions from the main engine, the CO_2 from the auxiliary

$$EEDI = \frac{(\prod_{j=1}^{n} f_j)(\sum_{i=1}^{nME} P_{ME(i)} \times C_{FME(i)} \times SFC_{ME(i)}) + (P_{AE} \times C_{FAE} \times SFC_{AE}) + PTI + EFF}{f_i \times f_c \times Capacity \times f_w \times V_{ref}} \quad (11)$$

$$EEDI(modified) = \frac{(\prod_{j=1}^{n} f_j)(\sum_{i=1}^{nME} P_{ME(i)} \times (C_{FME(i)} \times f_{CO_2(i)}) \times SFC_{ME(i)}) + (P_{AE} \times C_{FAE} \times SFC_{AE}) + PTI + EFF}{f \times Capacity \times V_{ref}} \quad (12)$$

engines, and the additional CO_2 from power take-in (PTI) are added together. Then, this value minus the CO_2 reduction by energy abatement devices, such as waste heat recovery system, is divided by the size and speed of the ship (Eq. (11)). P denotes the output of the engine (kW), and ME and AE denote the main and auxiliary engines, respectively. SFC refers to the fuel consumption rate (g/kWh) of an engine, and C_F refers to the tonnage of CO_2 emitted from the ship when 1 ton of specific fuel is consumed. Capacity refers to deadweight tonnage, and V_{ref} refers to the standard speed of the ship (knot). Finally, f is the efficiency index of the ship by ship type. Detailed figures and explanations related to each item in the equation can be found in IMO (2018). According to the current EEDI calculation method, even if CO_2 is directly captured and removed from the ship exhaust gas, this figure is not reflected in the EEDI of the ship. Lee et al. (2021) proposed an improved EEDI calculation method as expressed in Eqs. (12) and (13), which reflects the amount of removed CO_2 in EEDI when CO_2 contained in exhaust gas emitted from a ship to the atmosphere is removed using the onboard carbon capture process. In this method, the carbon capture process can be reflected in the EEDI by adding Eq. (13) for the CO_2 reduction rate to the term denoting the CO_2 emission from the main engine. $m_{capture}$ refers to the mass of CO_2 removed, and $m_{exhaust}$ refers to the mass of total CO_2 included in the exhaust gas. In this study, the EEDI of a ship was calculated using the EEDI calculation method proposed by Lee et al. (2021). All the EEDI calculations below have been performed according to the calculation method of Lee et al. (2021).

$$f_{CO_2} = 1 - \frac{m_{capture}}{m_{exhaust}} \quad (13)$$

The CO_2 emitted from ships can be estimated using the following equation:

$$E = P_j \times LF_j \times EF_j \quad (14)$$

where E is the hourly CO_2 emissions (kg/h), P_j is the average maximum output of the engine by ship type (kW), LF_j is the load factor of the engine by ship type, and EF_j is the emission factor (g/kWh) of the engine according to the exhaust gas composition. Tables 7, 8, and 9 show the average maximum output (kW) of diesel engines by ship type, the average load factor of diesel engines by ship type, and the emission factor according to fuel, respectively. Table 10

Table 7 Average power of diesel engines by ship type (kW) (U.S. Environmental Protection Agency, 2009)

Bulk carrier	Container ship	Passenger ship	General cargo	RORO	Tanker	Reefer
8,000	30,900	39,600	9,300	11,000	9,400	9,600

Table 8 Average load factor of diesel engines by ship type (U.S. Environmental protection Agency, 2009; ENTEC, 2007)

Bulk carrier	Container ship	Passenger ship	General cargo	RORO	Tanker	Reefer
0.75	0.80	0.5	0.80	0.80	0.75	0.80

Table 9 CO_2 emission factor of four-stroke engine (g/kWh) (Kristensen, 2012)

Fuels	MDO (Marine Diesel Oil)	LNG (Liquified Natural Gas)
Emission factor (g/kwh)	609	426

Table 10 Flue gas compositions of MAN B&W ME-GI engine (Kristensen, 2012)

Composition	Unit	Diesel mode (MDO)	Gas mode (LNG)
N_2	mol%	80.21	81.83
O_2	mol%	15.05	14.65
CO_2	mol%	4.74	3.52
CO	ppm	51.0	55.0
HC	ppmC	46.5	143.5
NO_x	ppm	1002	1044

Table 11 EEDI reference line (MEPC 215(63); IMO, 2012)

Reference line $= a \times b^{-c}$			
Ship type	a	b	c
Bulk carrier	961.79	Deadweight tonnage (DWT)	0.477
Gas carrier	1120.00		0.456
Tanker	1218.80		0.488
Container ship	174.22		0.201
General cargo	107.48		0.216
Reefer	227.01		0.244
RORO	1405.15		0.498

Table 12 Required EEDI for phase 3 (MEPC 75/18; IMO, 2020)

Ship type	Bulk carrier		Tanker		Container ship					
DWT	20,000–	10,000–20,000	20,000–	4,000–20,000	200,000–	120,000–200,000	80,000–120,000	40,000–80,000	15,000–40,000	10,000–15,000
reduction rate (%)	30	0–30	30	0–30	50	45	40	35	30	15–30

summarizes the composition of exhaust gas discharged from MAN B&W's ME-GI (main engine electronic control gas injection) engine.

The IMO presented the EEDI reference line as an exponential function as shown in Table 11 according to the ship type and tonnage, and specified the target reduction rate compared with the EEDI reference line according to the ship type and tonnage. Table 12 summarizes the EEDI Phase 3 target reduction rates by major ship type.

According to the third IMG GHG study, three ship types, i.e., bulk carrier, tanker, and container ship, account for 60% of the total onboard carbon emissions. Therefore, a total of six onboard emission scenarios were selected for the case of using diesel and LNG as fuel for each of the three ship types: bulk carrier, tanker, and container ship. Scenarios 1, 2, and 3 were selected for bulk carriers, container ships, and tankers using diesel as fuel, respectively. In addition, scenarios 4, 5, and 6 were selected for bulk carriers, container ships, and tankers using LNG as fuel, respectively. Table 13 lists the EEDI values for each of the six scenarios based on the above data related to CO_2 emission from ships. The tonnage of the ship used in the EEDI calculation was interpolated using the tonnage-engine output data of the Environmental Protection Agency (2009). For the V_{ref} of the ship, the speed of the ship was set to 0.75 MCR (maximum continuous rated) proposed by Notteboom and Carriou (2009). Furthermore, the EEDI reference according to the tonnage and ship type for each scenario was calculated. Finally, the target EEDI required for the EEDI Phase 3 was calculated, and the required CO_2 reduction rate to

Table 13 EEDI by ship emission scenario

Case No.	Fuel	Ship type	Capacity (DWT)	V_{ref}	EEDI	EEDI reference	EEDI phase 3	Required CO_2 reduction rate
1	Diesel (MDO)	Bulk carrier	45688	14.5	6.250	5.759	4.031 (-30%)	43.9%
2		Container ship	47213	24	21.59	20.03	13.02 (-35%)	45.2%
3		Tanker	63750	12	6.323	5.512	3.859 (-30%)	40.2%
4	Gas (LNG)	Bulk carrier	45688	14.5	5.029	5.759	4.031 (-30%)	28.5%
5		Container ship	47213	24	17.37	20.03	13.02 (-35%)	22.5%
6		Tanker	63750	12	5.088	5.512	3.859 (-30%)	27.2%

Table 14 CO_2 emissions and exhaust gas flow rate by scenarios

Case No.	CO_2 emissions (kg/h)	Exhaust gas flow rate (kg/h)	Target CO_2 reduction rate	Target CO_2 reduction (kg/h)
1	3564.0	51447.4	50%	1782.0
2	15054.5	211963.3		7527.3
3	4293.4	60450.7		2146.7
4	2940.0	55341.2	30%	882.0
5	12112.8	228005.6		3633.8
6	3454.5	65025.9		1036.4

achieve this goal is listed in Table 13.

Then, based on the above data on ship CO_2 emissions, the CO_2 emissions and total exhaust gas flow rate of each scenario were calculated and summarized in Table 14. As listed in Table 13, the CO_2 reduction rate required in the scenario using diesel as fuel is 40%–50%. Hence, the target CO_2 reduction rate in the diesel scenario was set to 50%. Similarly, the CO_2 reduction rate was set to 30% because the CO_2 reduction rate required in the scenario where LNG is used as fuel is 20%–30%. The target CO_2 reduction rates for each scenario are summarized in Table 14.

4.2 Simulation of Single Packed Column Process

Fig. 3 shows a flowchart of the simplest and most traditional type of CO_2 capture process using an aqueous amine solution. The process consists of two packed columns or tray columns and a heat exchanger. As the aqueous amine solution (lean amine) passes through the absorber, it absorbs CO_2 from the acid gas. The aqueous amine solution that has absorbed CO_2 (rich amine) is introduced into the stripper through the heat exchanger. The reboiler of the stripper performs high-temperature distillation to separate CO_2, which is then discharged to the top of the stripper. The regenerated aqueous amine solution passes through the heat exchanger and returns to the absorber.

For six onboard CO_2 emission scenarios, an onboard CO_2 capture process that removes 70% to 80% of CO_2 trapped in acid gas using a 30 wt% MEA solution was simulated based on the various coefficients and methods of the rate-based model used for simulation validation in the previous section. The removal rate of the CO_2 capture process using the MEA solution is generally set to 90%. However, when the removal rate is decreased, the amount of fluid flowing into the absorber increases. Hence, the diameter of the absorber increases, whereas the height of the absorber decreases. A removal rate lower than 90% was set to design an absorber with a lower height, and the reason will be described below. The absorber is packed with the filler material of Mellapak 250Y, and both diesel and LNG fuel usage scenarios are packed to 7.8 m. The exhaust gas cooled to 40 ℃ flows into the bottom of the absorber, and the MEA solution cooled to 45 ℃ flows into the top of the absorber. The stripper is packed with Mellapak 250Y to 4.1 m in the diesel scenario and 4.0 m in the LNG scenario. The MEA solution is heated to 109.5 ℃ through the reboiler at the bottom of the stripper. For both absorber and stripper, the maximum flooding rate was set to 75%. Detailed operation information of each column is summarized in Table 15, and the process operation flow rates and target CO_2 removals are summarized in Table 16. The composition of flue gas CO_2 of diesel fuel is 4.74 mol%, and the composition of flue gas CO_2 of LNG fuel is 3.52 mol% (Table 10). When diesel is used as fuel, the flow rate of flue gas and CO_2 emission are higher than those when LNG is used as fuel.

Table 15 Design specifications for single column

	Absorber	Stripper
Packing type	Mellapak 250Y	Mellapak 250Y
Pressure	1.1 barg (210.3 kPa)	0.2 barg (121.3 kPa) (min.) 0.8 barg (181.3 kPa) (max.)
Temperature	42.7 ℃ (min.) 73.3 ℃ (max.)	85 ℃ (condenser) 109.5 ℃ (reboiler)
Lean solvent loading	0.19	-
Rich solvent loading	0.324 (Diesel) 0.310 (LNG)	- -
CO_2 removal rate	78.6% (Diesel) 70.1% (LNG)	- -
Packing height	7.8 m	4.1 m (Diesel) 4.0 m (LNG)
L/G ratio	2 (Diesel) 1.4 (LNG)	- -
Reboiler duty	-	3.80 GJ/t CO_2

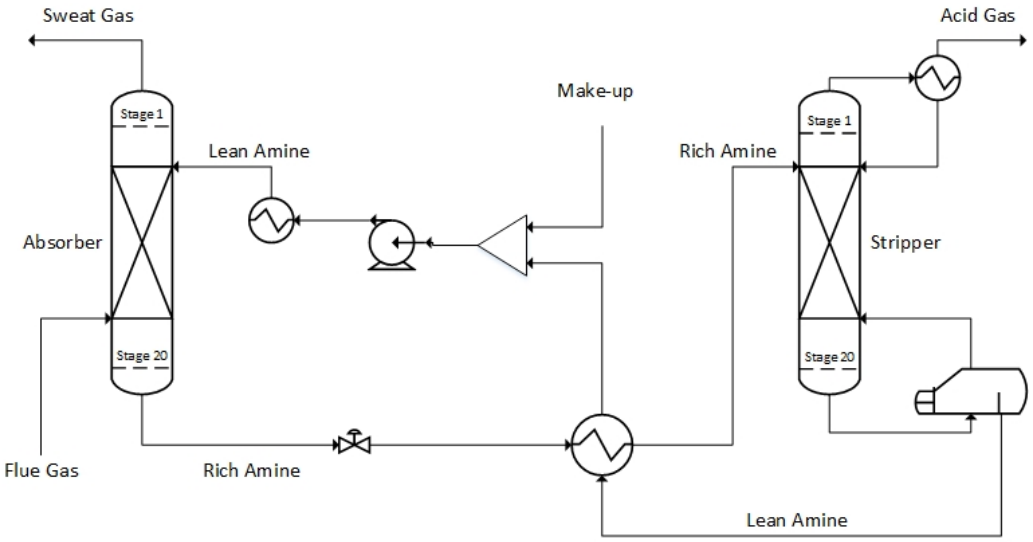

Fig. 3 Conventional CO_2 capture process based on aqueous amine solution

Table 16 Operating conditions for a single column

Case No.	Target CO_2 reduction (kg/h)	CO_2 removal rate in absorber	Process inlet CO_2 flow rate (kg/h)	Process inlet exhaust gas flow rate (kg/h)
1	1782.0		2267.2	32727.8
2	7527.3	78.6%	9576.7	138244.8
3	2146.7		2731.2	39425.8
4	882.0		1258.2	23683.9
5	3633.8	70.1%	5183.7	97576.4
6	1036.4		1478.5	27829.9

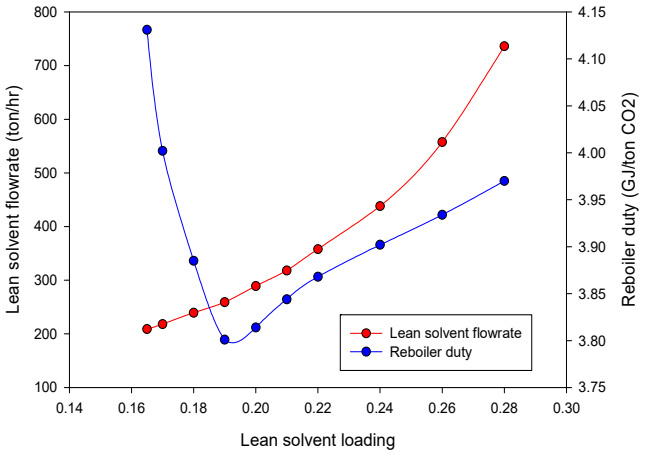

Fig. 4 Effect of lean loading on the MEA solution flow rate (red line) and reboiler duty (blue line)

The lean loading (mol CO_2/mol MEA) of the MEA solution flowing into the absorber should be considered carefully because it is one of the major factors influencing the overall process, including the flow rate of the MEA solution, the size of the absorber and stripper, and the amount of heat consumed in the reboiler of the stripper. Fig. 4 shows the effect of lean loading on the flow rate of the MEA solution required and the amount of heat consumed in the reboiler. The lowest energy consumption is 3.80 GJ/t CO_2 for the lean loading of 0.19 mol CO_2/mol MEA. Therefore, the lean loading of the MEA solution simulating the onboard CO_2 capture process was fixed at 0.19 mol CO_2/mol MEA, which requires the lowest amount of energy. At a lean loading below 0.19 mol, the required flow rate of the MEA solution decreases, whereas the CO_2 absorption performance and speed increase; however, the amount of heat consumed to regenerate the MEA solution increases exponentially. This is because more energy is required to achieve a lower level of CO_2 loading when rich MEA that has absorbed CO_2 is regenerated in the stripper. If the lean loading increases, the required flow rate of the MEA solution increases. This in turn increases sensible heat, the overall size of the equipment, and the risk of column flooding.

Table 17 lists the size results of simulating the CO_2 capture process according to the aforementioned six onboard CO_2 emission scenarios. The size simulation of the device was performed using the Aspen process economic analyzer installed as an add-on of Aspen Plus. The flow rate of exhaust gas varied considerably according to each scenario, and the column diameter changed significantly as a result. In both the diesel and LNG scenarios, the absorber height was the same at approximately 12.2 m. The height of the stripper was approximately 8.5 m for the diesel scenario and approximately 8.4 m for the LNG scenario. This is because the lean solvent loading was the same in both scenarios, but the partial pressure of CO_2 of the aqueous amine solution flowing into the stripper was different. Furthermore, the overall column height was significantly increased by additional devices installed in the columns compared with the height of the filler in each case.

The onboard CO_2 capture process assumed in this study aims to demonstrate the possibility of implementing a simple CO_2 capture process without extensive remodeling for ships beyond EEDI Phase 3 among existing ships. However, the calculated column height exceeded 8 m in all scenarios, and the height of the absorber in particular reached 12.2 m. Assuming that all the above scenarios are for small- and medium-sized ships, there is a possibility that such a high column height may exceed the height of the engine room or the height of the stack. This indicates that, to implement the CO_2 capture process, extensive repair and maintenance of the ship are required, such as making a hole in the ship's deck or expanding the stack.

Table 17 Simulation result of single column

Case No.	Absorber diameter (m)	Absorber height (m)	Stripper diameter (m)	Stripper height (m)
1	1.7760		1.4340	
2	3.6342	12.192	2.9473	8.5344
3	1.9408		1.5740	
4	0.9604		0.7482	
5	1.9880	12.192	1.5188	8.3820
6	1.0562		0.8190	

Moreover, the hull is inevitably inclined owing to six-degree-of-freedom motions, such as roll, pitch, and yaw, which is unavoidable for the ships floating on the water during operation. Consequently, as the absorber installed on the ship is tilted, it is likely that the CO_2 absorption performance will decrease (Di et al., 2018). According to Son et al. (2017), maldistribution of liquid inside a tilted column increases significantly as the packed column height increases. This interferes with smooth process operation and decreases column performance. Therefore, in this study, a parallel column CO_2 capture process with two absorbers and two strippers was newly simulated with the objective of implementing a CO_2 capture process in which the height does not exceed 3 TEU (TEU indicates the size of a standard container, and the height of 3 TEU is 7.8 m).

4.3 Simulation of Parallel Packed Column Process

Absorber intercooling is an improved absorber process operation method widely used to increase the efficiency of the on-shore CO_2 capture process using amines. This method forms a temperature imbalance inside the absorber because the CO_2 absorption reaction by amines is an exothermic reaction. In general, the highest temperature in the absorber is generated in the middle part of the absorber. The absorber intercooling process decreases the overall temperature of the fluid inside the absorber by installing a cooler in this highest-temperature part to provide a cooling circulating flow inside it. CO_2 absorption reaction using amines occurs more actively in an environment with a low temperature owing to the solubility of gas. Hence, the installation of an intercooler increases the CO_2 absorption capacity of the aqueous amine solution. Therefore, the intercooling process can have positive effects, such as reductions in the flow rate of the aqueous amine solution required for CO_2 capture, the overall size of the equipment, the energy consumption of the reboiler, and process operation cost.

A parallel absorber using an intercooling device was devised to lower the column height required for the onboard CO_2 capture process based on the basic concept of the absorber intercooling process. As shown in Fig. 5(a), the regenerated aqueous amine solution flows into the upper part of the first absorber, and the gas from which CO_2 is removed is discharged through the upper part of the first absorber. The aqueous amine solution that has slightly absorbed CO_2 comes out from the bottom of the first absorber, passes through the cooler, and flows

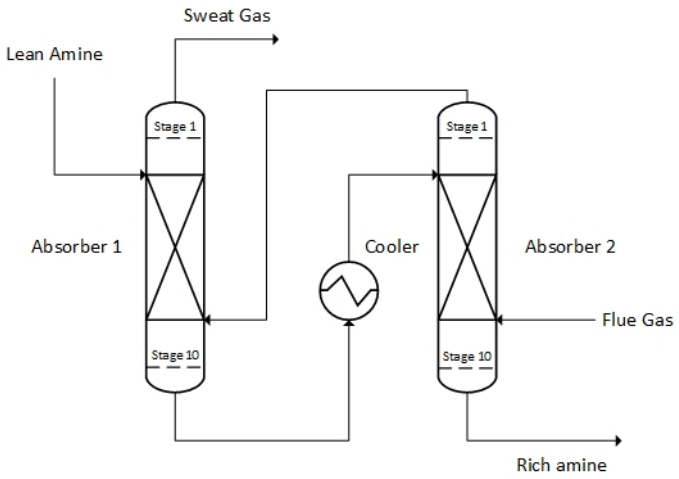

(a) Process flow diagram for parallel absorbers

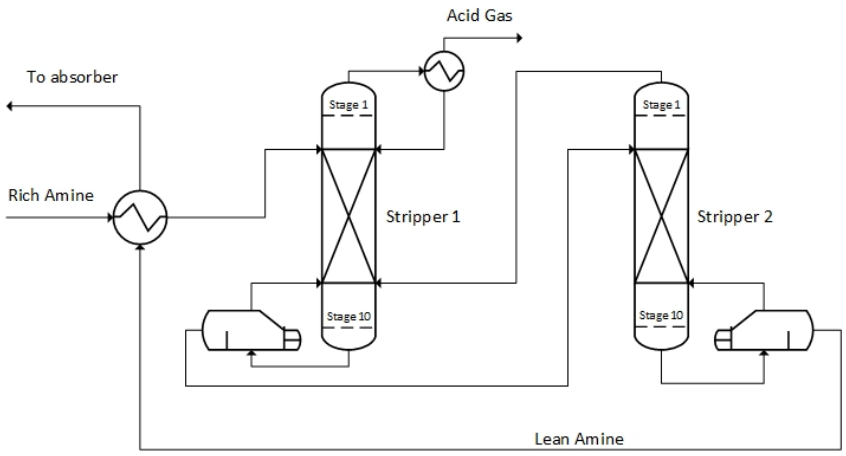

(b) Process flow diagram for parallel strippers

Fig. 5 Process flow diagram of CO_2 capture process using parallel columns

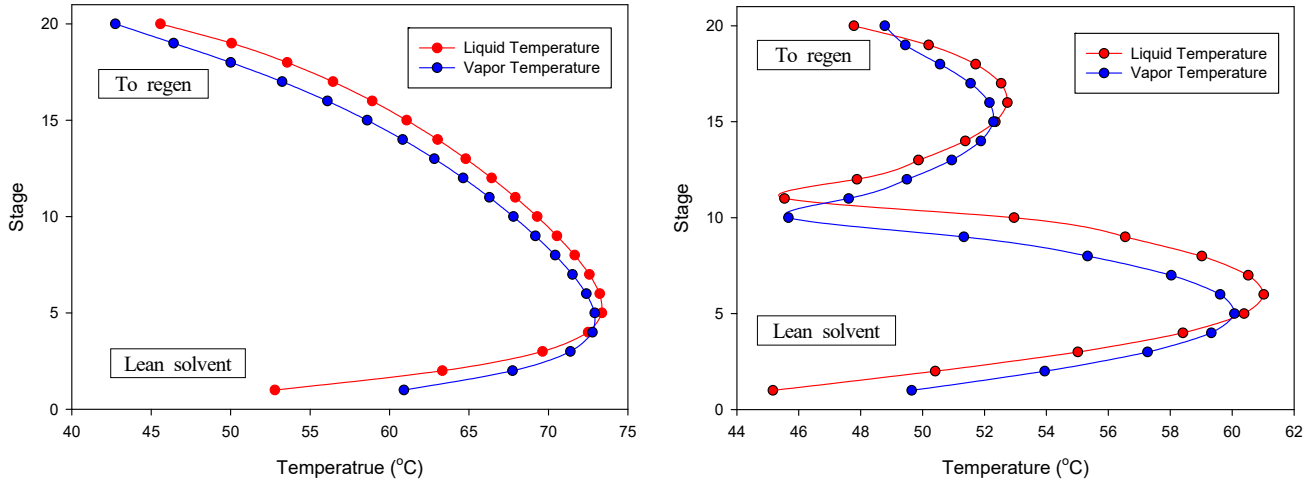

(a) Temperature profile of a single absorber (b) Temperature profile of parallel absorbers

Fig. 6 Temperature profiles of absorbers

into the top of the second absorber at a low temperature. The exhaust gas flows into the bottom of the second absorber, and the aqueous amine solution that has completely absorbed CO_2 is discharged from the bottom of the second absorber.

Fig. 6(a) shows the temperature gradient inside the absorber in a single absorber process. A relatively low temperature is maintained at the top and bottom of the absorber because the inflow of the low-temperature MEA solution and exhaust gas continues. However, the temperature of the fluid inside the absorber rises owing to the CO_2 absorption reaction of MEA, which is an exothermic reaction, and the highest temperature of 72.5 ℃ can be observed near stage 5. Fig. 6(b) shows the temperature gradient inside the absorber in the parallel absorber process. Stages 1 to 10 represent the first absorber, and stages 11 to 20 represent the second absorber. A low temperature is maintained in stages 1 and 20, where the MEA solution and exhaust gas are introduced, as well as in stages 10 and 11, which pass through the cooler. Hence, the maximum temperature of the entire absorber remains at approximately 61 ℃. The absorption performance of the MEA solution also increased, which was able to reduce the total MEA solution flow rate by 12%.

In Figs. 6 (a) and (b), the temperature of the incoming MEA solution is 40 ℃ in both cases. However, the temperatures of the single absorber in stage 1 are 52.8 ℃ (liquid) and 60.8 ℃ (gas), and the temperatures of the parallel absorber in stage 1 are 45.2 ℃ (liquid) and 49.6 ℃ (gas). This is because stage 5, the point at which the reaction occurs most actively in the absorber, is close to stage 1, the inlet of the MEA solution; therefore, the temperature of stage 1 changes relatively significantly according to the maximum internal temperature of the absorber. As the maximum temperatures inside the single absorber and the parallel absorber differ by approximately 10 ℃, the temperature of stage 1, which is close to temperature bulge, also shows a difference of approximately 5–10 ℃. The basic concept of stripper interheating is the same as that of absorber intercooling. A heater is installed in the middle of the stripper to raise the overall temperature of the stripper. The amine solution that absorbs CO_2 is heated in the stripper to separate the absorbed CO_2. The regeneration efficiency increases if a higher temperature is maintained up to the top of the stripper. This can be expected to reduce the energy consumption in the reboiler and the size of the stripper. Based on this concept, the rich MEA solution is introduced at the top of the first stripper and the separated CO_2 is discharged as shown in Fig. 5(b). The MEA solution heated by the reboiler at the bottom of the first stripper flows into the top of the second stripper. At the bottom of the second stripper, the MEA solution after CO_2 separation flows to the absorber through the heat exchanger.

Fig. 7 shows the energy consumption required to achieve the same lean CO_2 loading according to the ratio of energy consumed by the reboiler of each stripper. The x-axis represents the ratio of energy consumption of the reboiler of the second stripper to the total energy consumption. The y-axis represents the total energy consumption. The amounts of energy consumed by the first and second reboilers, respectively, are shown in different colors. A relatively high energy

Table 18 Design specifications for parallel absorbers

	Absorber 1	Absorber 2
Packing type	Mellapak 250Y	Mellapak 250Y
Pressure	1.05 barg (206.3 kPa)	0.97 barg (198.3 kPa)
Temperature	45.2 ℃ (min) 61.0 ℃ (max)	48.0 ℃ (min) 53.1 ℃ (max)
Lean solvent loading	0.19	
Rich solvent loading	0.346 (Diesel) 0.331 (LNG)	
CO_2 removal rate	79.1% (Diesel) 70.6% (LNG)	
Packing height	4.0 m	
L/G ratio	1.7 (Diesel) 1.3 (LNG)	

Table 19 Design specifications for parallel strippers

	Stripper 1	Stripper 2
Packing type	Mellapak 250Y	Mellapak 250Y
Pressure	0.2 barg (121.3 kPa) (min)	0.7 barg (171.3 kPa) (min)
	0.68 barg (169.3 kPa) (max)	0.9 barg (191.3. kPa) (max)
Temperature	99.7 ℃ (min)	118.2 ℃ (min)
	118.6 ℃ (max)	121 ℃ (max)
Packing height	2.3 m (Diesel)	
	2.2 m (LNG)	
Reboiler duty	3.76 GJ/t CO_2	
	3.55 GJ/t CO_2	

consumption can be observed at 0%–10% when the reboiler of the second stripper is used less or is not used. This indicates that inefficient energy input is required to heat the bottom of the second stripper sufficiently only with the reboiler of the first stripper. The overall energy consumption decreases as the proportion of energy consumption of the reboiler of the second stripper gradually increases, reaching a minimum of 3.76 GJ/t CO_2 at 60%. Beyond the proportion of 60%, the total energy consumption increases again. This appears to be because a relatively large amount of energy is input to heat the top of the first stripper sufficiently with the reboiler of the second stripper. Therefore, in the parallel absorber process, the ratio of energy consumption of the reboiler of the first stripper and the reboiler of the second stripper was simulated as 4:6. Tables 18 and 19 list the detailed operational information of the parallel packed column process.

Table 20 lists the process simulation size results for the six scenarios of the CO_2 capture process for parallel packed columns. The diameters of both the absorber and stripper changed according to the flow rate of each scenario. When compared with the single absorber process, the flow rate of the MEA solution decreased, and the overall diameter of the column decreased as a result. The absorber heights in both

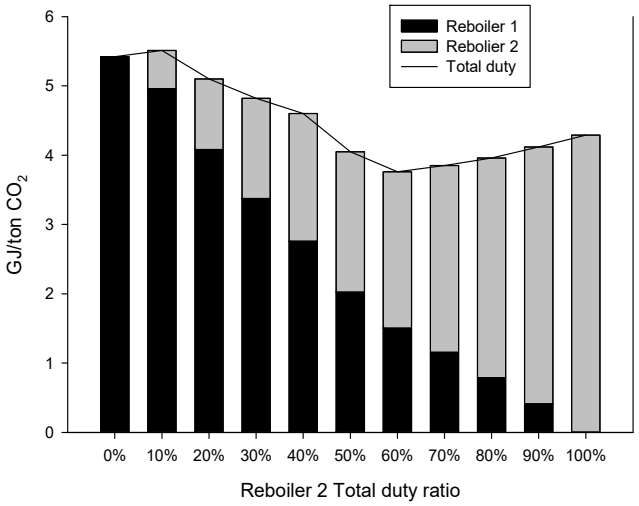

Fig. 7 Total duty change according to reboiler duty ratio

Table 20 Simulation results of parallel columns

Case No.	Absorber diameter (m)	Absorber height (m)	Stripper diameter (m)	Stripper height (m)
1	1.7052	7.5820	1.3452	6.5360
2	3.4878		2.7648	
3	1.8626		1.4764	
4	0.9394		0.7019	6.4196
5	1.9066		1.4247	
6	1.0182		0.7608	

scenarios were approximately 7.6 m, which were much lower than the height of the single packed column, i.e., 12.2 m. Thus, the column height was simulated to be lower than the intended height of 3 TEU (7.8 m). The height of the stripper was simulated as approximately 6.5 m in the diesel scenario and approximately 6.4 m in the LNG scenario, which were lower than 8.5 m and 8.4 m for the single packed column, respectively, and also lower than the target height of 3 TEU.

4. Conclusions

A technology to reduce CO_2 emissions that can be immediately applied is required owing to the expedited implementation of the EEDI Phase 3. Thus, in this study, an MEA-based onboard CO_2 capture process was simulated and the required column size was examined. Before the simulation, the average CO_2 emission according to the ship type was calculated, and the amount of CO_2 reduction required for the implementation of the EEDI Phase 3 was calculated. Six scenarios were defined according to ship type and fuel, and the MEA-based onboard CO_2 capture process required for these scenarios was simulated. The process simulation was conducted using the rate-based model of Aspen Plus v10, a commercial process simulator. The operational data of the pilot plant were used to verify the accuracy and reproducibility of the process simulation. Various correction factors and correlation methods of the rate-based model were carefully adjusted and selected based on the operation data of the pilot plant. The results of process simulation were validated by comparing them with the operation data. The MEA-based CO_2 capture process required for the six onboard CO_2 emission scenarios selected above was simulated through the adjusted rate-based model. The onboard CO_2 capture process was designed to include the most widely used basic types of absorber, stripper, and heat exchanger. Furthermore, the CO_2 reduction rate of 70%–80% was targeted based on lean loading with the minimum energy consumption in the reboiler. The result of process simulation confirmed that an absorber and a stripper with a diameter of approximately 0.7 m–3.6 m and a height of 8.4 m–12.2 m were required depending on the scenario.

A lower column height in the onboard CO_2 capture process is more advantageous owing to the characteristics of ships. The column height of up to 12.2 m in the onboard CO_2 capture process simulated above was too high for implementation on a ship. Therefore, to lower the

column height, an onboard CO_2 capture process using parallel packed columns was newly designed and simulated. Both the absorber and stripper were designed to have two parallel columns, and each column was connected by applying the intercooling and interheating concepts. Consequently, the onboard CO_2 capture process could be configured with columns having a diameter of approximately 0.7 m–3.5 m and a height of 6.4 m–7.6 m. Therefore, immediate onboard application would be possible because the column height is less than 3 TEU or 7.8 m. However, the CO_2 capture process with parallel packed columns increases the space required for installation, as the required number of columns increases compared with that in the conventional process. This is a disadvantage, as ships have several spatial constraints. Therefore, the size of the engine room, the location of the stack, and the arrangement of the deck structure should be carefully considered to apply the parallel column process to an actual ship.

The CO_2 capture process using amines requires a considerable amount of heat to regenerate the aqueous amine solution owing to the nature of the process. It is assumed that the thermal energy required for the onboard amine CO_2 capture process is supplied through the waste heat of the engine and exhaust gas. However, an auxiliary engine is required to generate additional power if sufficient waste heat is not supplied to regenerate all the aqueous amine solution. This additional power generation results in higher CO_2 emissions than before. Therefore, the target CO_2 removal to achieve the EEDI Phase 3 will be higher than that initially calculated. This aspect requires a close review because it leads to additional increases in load and size in the capture process. Therefore, further studies are required to optimize the energy flow of the process and to design the process considering the additional energy required by the implementation of the onboard CO_2 capture process.

Conflict of Interest

No potential conflict of interest relevant to this article was reported.

Funding

This research was supported by a grant (RS-2022-00143644) funded by Ministry of Land, Infrastructure and Transport of Korean government.

References

Agbonghae, E.O., Hughes, K.J., Ingham, D.B., Ma, L., & Pourkashanian, M. (2014). Optimal Process Design of Commercial-Scale Amine-Based CO_2 Capture Plants. Industrial & Engineering Chemistry Research, 53(38), 14815–14829. https://doi.org/10.1021/ie5023767

Al-Baghli, N.A., Pruess, S.A., Yesavage, V.F., & Selim, M.S. (2001). A Rate-based Model for the Design of Gas Absorbers for the Removal of CO_2 and H2S Using Aqueous Solutions of MEA and DEA. Fluid Phase Equilibria, 185(1–2), 31–43. https://doi.org/10.1016/S0378-3812(01)00454-X

Bodansky, D. (2016). The Legal Character of the Paris Agreement. Review of European, Comparative & International Environmental Law, 25(2), 142–150. https://doi.org/10.1111/reel.12154

Bravo, J.L., Rocha, J.A., & Fair, J.R. (1985). Mass Transfer in Gauze Packings. Hydrocarbon Processing (International ed.), 64(1), 91–95.

Chilton, T.H., & Colburn, A.P. (1934). Mass Transfer (Absorption) Coefficients Prediction from Data on Heat Transfer and Fluid Friction. Industrial & Engineering Chemistry, 26(11), 1183–1187. https://doi.org/10.1021/ie50299a012

DNV GL. (2017). Low Carbon Shipping Towards 2050.

DNV GL. (2018). Emission Pathway 2015–2030.

Di, X.N., Wang, W.H., Chen, S.J., & Huang, Y. (2018). Effect of Tilt on Mass Transfer and Hydrodynamic Performance in a Packing Column. Chemical Engineering and Processing - Process Intensification, 123, 89-99. https://doi.org/10.1016/j.cep.2017.10.028

ENTEC. (2007). Ship Emissions Inventory – Mediterranean Sea, Final Report. Entec Limited, London.

Environmental Protection Agency (EPA). (2009). Proposal to Designate an Emission Control Area for Nitrogen Oxides, Sulfur Oxides and Particulate Matter. USA: Environmental Protection Agency.

Feenstra, M., Monteiro, J., Akker, J.T., Abu-Zahra, M.R.M., Gilling, E., & Goetheer, E., (2019). Ship-based Carbon Capture Onboard of Diesel or LNG-fuelled Ships. International Journal of Greenhouse Gas Control, 85, 1–10. https://doi.org/10.1016/j.ijggc.2019.03.008

Hikita, H., Asai, S., Katsu, Y., & Ikuno, S. (1979). Absorption of Carbon Dioxide into Aqueous Monoethanolamine Solutions. AIChE Journal, 25(5), 793–800. https://doi.org/10.1002/aic.690250507

IMO. (2012). Guidelines for Calculation of Reference Lines for Use with the Energy Efficiency Design Index (EEDI). Resolution MEPC 215(63), International Maritime Organization, London.

IMO. (2014). Greenhouse Gas Study 2014, Executive Summary and Final Report. International Maritime Organization, London.

IMO. (2018). Guidelines on the Method of Calculation of the Attained Energy Efficiency Index (EEDI) for New Ships. Resolution MEPC 308(73), International Maritime Organization, London.

IMO. (2020). Fourth IMO GHG Study 2020 – Final Report. MEPC 75/18, International Maritime Organization, London.

Kristensen, H.O. (2012). Energy Demand and Exhaust Gas Emissions of Marine Engines. Clean Shipping Currents, 1(6), 18–26.

Lee, S., Yoo, S., Park, H., Ahn, J., & Chang, D. (2021). Novel Methodology for EEDI Calculation Considering Onboard Carbon Capture and Storage System. International Journal of Greenhouse Gas Control, 105, 103241. https://doi.org/10.1016/j.ijggc.2020.103241

Luo, X., & Wang, M. (2017). Study of Solvent-based Carbon Capture for Cargo Ships through Process Modelling and Simulation. Applied Energy, 195, 402−413. https://doi.org/10.1016/j.apenergy.2017.03.027

Notteboom, T., & Carriou, P., (2009). Fuel Surcharge Practices of Container Shipping Lines: Is It About Cost Recovery or Revenue Mking? Proceedings of the International Association of Maritime Economists (IAME) Conference, Copenhagen, Denmark.

Olivier, J.G.J, Schure, K.M., & Peters, J.A.H.W. (2017). Trends in Gloval CO2 and Total Greenhous Gas Emissions. PBL Netherlands Environmental Assessment Agency.

Onda, K., Takeuchi, H., & Okumoto, Y. (1968). Mass Transfer Coefficients between Gas and Liquid Phases in Packed Columns. Journal of Chemical Engineering of Japan, 1(1), 56−62. https://doi.org/10.1252/jcej.1.56

Pinsent, B.R.W., Pearson, L., & Roughton, F.J.W. (1956). The Kinetics of Combination of Carbon Dioxide with Hydroxide Ions. Transactions of the Faraday Society, 52, 1512−1520. https://doi.org/10.1039/TF9565201512

Son, Y., Kim, G., Lee, S., Kim, H., Min, K., & Lee, K.S. (2017). Experimental Investigation of Liquid Distribution in a Packed Column with Structured Packing under Permanent Tilt and Roll Motions Using Electrical Resistance Tomography. Chemical Engineering Science, 166, 168−180. https://doi.org/10.1016/j.ces.2017.03.044

Stec, M., Tatarczuk, A., Więcław-Solny, L., Krótki, A., Ściążko, M., & Tokarski, S. (2015). Pilot Plant Results for Advanced CO_2 Capture Process Using Amine Scrubbing at the Jaworzno II Power Plant in Poland. Fuel, 151, 50−56. https://doi.org/10.1016/j.fuel.2015.01.014

Stichlmair, J., Bravo, J.L., & Fair, J.R. (1989). General Model for Prediction of Pressure Drop and Capacity of Countercurrent Gas/Liquid Packed Columns. Gas Separation & Purification, 3(1), 19−28. https://doi.org/10.1016/0950-4214(89)80016-7

Zhang, Y., & Chen, C.C. (2013). Modeling CO_2 Absorption and Desorption by Aqueous Monoethanolamine Solution with Aspen Rate-based Model. Energy Procedia, 37, 1584−1596. https://doi.org/10.1016/j.egypro.2013.06.034

Zhang, Y., Chen, H., Chen, C.C., Plaza, J.M., Dugas, R., & Rochelle, G.T. (2009). Rate-Based Process Modeling Study of CO2 Capture with Aqueous Monoethanolamine Solution. Industrial & Engineering Chemistry Research, 48(20), 9233−9246. https://doi.org/10.1021/ie900068k

Zhou, P., & Wang, H. (2014). Carbon Capture and Storage—Solidification and Storage of Carbon Dioxide Captured on Ships. Ocean Engineering, 91, 172−180. https://doi.org/10.1016/j.oceaneng.2014.09.006

Author ORCIDs

Author name	ORCID
Jung, Jongyeon	0000-0002-7557-6587
Seo, Yutaek	0000-0001-8537-579X

KSOE

Journal of Ocean Engineering and Technology 36(3), 181-193, June, 2022
https://doi.org/10.26748/KSOE.2022.001

pISSN 1225-0767
eISSN 2287-6715

Original Research Article

Mission Management Technique for Multi-sensor-based AUV Docking

Hyungjoo Kang[1], Gun Rae Cho[2], Min-Gyu Kim[3], Mun-Jik Lee[1], Ji-Hong Li[4], Ho Sung Kim[5], Hansol Lee[6] and Gwonsoo Lee[7]

[1]*Senior Researcher, Intelligent Robotics R&D Division, Korea Institute of Robotics & Technology Convergence, Pohang, Korea*
[2]*Principal Researcher, Intelligent Robotics R&D Division, Korea Institute of Robotics & Technology Convergence, Pohang, Korea*
[3]*Researcher, Intelligent Robotics R&D Division, Korea Institute of Robotics & Technology Convergence, Pohang, Korea*
[4]*Chief Researcher, Intelligent Robotics R&D Division, Korea Institute of Robotics & Technology Convergence, Pohang, Korea*
[5]*Senior Engineer, Naval System Team 2 / Naval R&D Center, Hanwha Systems, Gumi, Korea*
[6]*Engineer, Naval System Team 2 / Naval R&D Center, Hanwha Systems, Gumi, Korea*
[7]*Doctorate Course, Mechatronics Engineering, Chungnam National University, Daejeon, Korea*

KEY WORDS: Autonomous underwater vehicle (AUV), Mission management, Multi-sensor-based docking, Feasible initial area (FIA), Terminal guidance, Docking station (DS)

ABSTRACT: *This study presents a mission management technique that is a key component of underwater docking system used to expand the operating range of autonomous underwater vehicle (AUV). We analyzed the docking scenario and AUV operating environment, defining the feasible initial area (FIA) level, event level, and global path (GP) command to improve the rate of docking success and AUV safety. Non-holonomic constraints, mounted sensor characteristic, AUV and mission state, and AUV behavior were considered. Using AUV and docking station, we conducted experiments on land and at sea. The first test was conducted on land to prevent loss and damage of the AUV and verify stability and interconnection with other algorithms; it performed well in normal and abnormal situations. Subsequently, we attempted to dock under the sea and verified its performance; it also worked well in a sea environment. In this study, we presented the mission management technique and showed its performance. We demonstrated AUV docking with this algorithm and verified that the rate of docking success was higher compared to those obtained in other studies.*

1. Introduction

Mission and operating environments are becoming more diverse and complex as the demand for operating autonomous underwater vehicles (AUVs) in the marine sector increases (Cho et al., 2019; Kim et al., 2021). However, when AUVs perform missions, such as exploring submarine topography/resources, inspecting marine structures, and monitoring the ocean, they must be recovered after a certain period of operation for recharging and backing up data because they are not supplied with external power and communication modules, resulting in considerable ship operation and launch or recovery costs and times, while making it impossible to perform launch or recovery missions under poor weather conditions. As a result, AUVs have several limitations in terms of operating range and time (Cho et al., 2019; Cho et al., 2020a).

Underwater docking technology is one methods for addressing these problems of AUVs. The operating range and time of AUVs can be increased by installing a docking station (DS) that receives power and communication lines from the land at an arbitrary underwater location and docking the AUVs at the docking station. To guide an AUV for docking, it is essential to develop a technique to estimate the relative distance and angle between the AUV and docking station, a terminal guidance control technique to precisely guide the AUV to the docking cone, and a mission management technique to increase the mission success rate and operational stability of the AUV (Park et al., 2019). Therefore, developed maritime countries, such as the United States and Japan, have been investigating various docking methods since the 2000s, including the hooking mechanism (Fukasawa et al., 2003; Kimball et al., 2018) and cone mechanism (Hobson et al., 2007; Zhang et al., 2017). Allen (2006) attempted docking in a cone-shaped station using the AUV remote environmental monitoring units (REMUS)-100 and successfully docked 17 times out of 29 attempts (approximately

Received 12 January 2022, revised 14 March 2022, accepted 31 March 2022
Corresponding author Hyungjoo Kang: +82-54-279-0461, hjkang@kiro.re.kr

59%); however, this docking success rate needs to be improved for application in an actual system (Allen et al., 2006). Li et al. (2015) conducted a study on docking using WL3-AUV in a water tank environment, succeeding in docking at a rate of approximately 80% using a camera and light-emitting diode (LED). However, they reported that problems such as image processing and LED brightness control would need to be resolved before applying in an actual sea environment (Li et al., 2015).

A mission management technique based on various data, such as the AUV's status information and information from multiple types of guidance sensors, is required to increase the success rate for docking an AUV in the actual sea environment. As the types of sensors increase, the hardware and software systems of the AUV become more complex, with different algorithms required to be used in combination. The mission management technique uses information from the sensors mounted on the AUV to continuously manage the status, location, attitude, and mission performance status of the AUV, while aiming to increase the efficiency and stability over the operating time and path. As a relevant previous study, Wolf et al. (2017) successfully demonstrated the execution of missions, such as reconnaissance, tracking, and inspections, by applying the control architecture for robotic agent command and sensing (CARACaS) in a number of unmanned surface vehicles (USVs). However, it appears that the application in an underwater system still needs to be supplemented because the study is limited to USVs with readily available data communication, with the system only allowing a restrictive intervention by the operator in emergency situations. Albiez et al. (2010) applied the mission management architecture developed for the AUV 'AVALON' equipped with six thrusters and successfully performed the exploration and tracking missions for underwater pipelines, but reported that further research would be necessary on the application in complex missions and systems. Barrouil and Lemaire (1999) developed the general-purpose programming and execution monitoring of autonomous systems (ProCoSA) and verified its suitable application in the AUV system through simulation; however, additional validation is required for actual underwater AUV systems. In addition, Pinto et al. (2012) designed and demonstrated a mission planning architecture for light AUV (LAUV)-Seacon AUV using teleo-reactive executive (T-REX) and confirmed that, although there was a problem in selecting the optimal sequence of actions, the architecture worked properly. Xue and Lekkas (2020) simulated T-REX and the robot operating system plan (ROSPlan) and compared and analyzed the performances, confirming their adequate operation despite each having its own strengths and weaknesses. Papadimitriou and Lane (2014) simulated a mission planning algorithm for performing a mine countermeasure (MCM) mission using a planning domain definition language (PDDL), confirming that the mission was successfully performed in a dynamic environment. An artificial intelligence (AI) planner of this type can reliably perform a given mission; however, it requires time and cost for initial installation and integration with existing systems. In addition, owing to hardware and software limitations in the manufactured AUV, the algorithm was not applied to this mission management technique.

In most of these existing studies, mission management systems have been developed with similar architectural structures, while the stability, efficiency, and scalability considering the performance of missions were emphasized. However, studies are being conducted on the use of USVs, where operators are allowed to intervene under certain conditions. In the case of AUVs, no external intervention is allowed during a mission, owing to the nature of the environment, making application and verification in an actual system difficult. In addition, as the demand for performing various missions increases, the AUV system is gradually becoming more complex, highlighting the significance of a relevant mission management technique.

In this study, we propose a mission management technique for the underwater docking of an AUV using multiple sensors. The proposed algorithm was applied to an AUV equipped with multiple guidance and inertial sensors to verify the operational performance on land and in an actual sea environment. The unmanned vehicle is operated with a single thruster and four control panels, and has the characteristics of a non-holonomic system (Kim et al., 2018). In the proposed mission management technique, the feasible initial area (FIA) level, event level, and global path (GP) command were defined to reflect the operating environment and docking scenarios of the AUV. To effectively utilize the multiple sensors and increase the docking success rate, the FIA level was defined in three stages considering the characteristics of the AUV and mounted sensors. In addition, the event level was specified based on the hardware and mission performance status of the AUV to ensure the stability in the mission performance of the AUV. Finally, the behavior of the AUV, depending on the situation, was defined by the GP command to allow autonomous responses to various situations that could occur during docking. Experiments were conducted on land and in the actual sea environment to verify the developed algorithm and confirm adequate operation based on the situation.

In Section 2 of this paper, the AUV and docking station used to validate the performance of the mission management technique are described. In Sections 3 and 4, the proposed mission management technique and performance verification experiments are described. Finally, the conclusions are summarized in Section 5.

2. Test-bed System

2.1 AUV and Docking Station

An AUV and a docking station were constructed, as shown in Figs. 1 and 2, to verify the performance of the underwater docking technique. The AUV is designed in the shape of a torpedo and consists of a bow, hull, and stern. The bow is equipped with guidance sensors, such as an inverted ultrashort baseline (iUSBL) transponder and forward-looking sonar (FLS), as well as navigation sensors, such as an inertial measurement unit (IMU), Doppler velocity log (DVL), and digital compass (DCS). The hull houses an electric unit, a battery,

Fig. 1 Test-bed AUV

Fig. 2 Docking station

communication equipment, among other components, while the stern houses a driving unit, including one thruster and four rudders. The AUV has the characteristics of an underactuated system, i.e., a non-holonomic system that must implement six degrees of freedom using a forward-direction thrust and pitch and yaw motion controls, requiring a terminal guidance control technique, and relative distance and direction estimation technique (Li and Lee, 2009). The docking station is a device capable of charging a battery and backing up data by docking the AUV and is shaped like a cone with unidirectional access. The docking station consists of a platform, power system, control unit, and guidance unit. An acoustic Doppler current profiler (ADCP) is installed on the platform to measure the direction of currents. The control unit can control the azimuth and altitude of the platform, and the guidance unit, including an optical guidance device and iUSBL transceiver, is installed in the docking cone where the AUV is received. Using this setup, the attitude of the docking station was corrected based on the seabed terrain, with the direction of the docking cone entrance adjusted to the direction of the current flowing to improve battery operation efficiency and docking success rate of the AUV (Kim, 2019).

2.2 AUV Navigation and Control

As mentioned above, underwater docking is an essential technology to overcome the limitations of the AUV in battery capacity and underwater communication. Implementing this technology requires (1) estimating the relative distance and direction between the AUV and docking station by combining the data from multiple sensors mounted on the AUV, (2) high-precision AUV terminal guidance control, and (3) docking mission management.

Hybrid underwater navigation estimates the accurate attitude of an AUV, with a Kalman filter constructed with navigation sensors to estimate IMU, DVL, and DCS, and the linear velocity, linear acceleration, and angular velocity of the AUV. In addition, a mechanical model is built using the AUV's altitude information, and the location and altitude of the AUV in navigation coordinates are estimated by integrating the linear velocity, linear acceleration, and angular velocity (Choo et al., 2020). Based on the estimated location and altitude information of the AUV, the relative distance and direction to the docking station with its location inputted in advance are estimated. A robust trajectory estimation control technique is used for precise terminal guidance control of AUV. The AUV used in the experiment has nonlinear dynamics combining rigid body dynamics and hydrodynamics. With the AUV's underactuated system, it is difficult to directly control all state variables, with restrictions between the state variables. In addition, disturbances, such as currents, on both sides of the AUV affect the uncontrollable state variables. Therefore, an attempt has been made to estimate and compensate for the nonlinear dynamics of the AUV using the time delay estimation technique and to overcome the characteristics of the underactuated system through the design of reference error dynamics (Cho et al., 2020b). The docking mission management technique is described in detail in the following section.

3. Mission Management Technique Design

3.1 Problem Statement

The AUV must perform underwater docking missions in the absence of external monitoring and intervention. In previous studies, USVs were used to perform specific missions, such as port monitoring and reconnaissance, assuming that an operator was present to monitor the performance of missions and the status of the USVs. Decisions regarding the selection of missions and methods were made by the algorithm, but the operator was allowed to intervene in emergency situations, such as damage. However, in the case of the AUV, communication with the outside is limited, with external intervention not allowed during the mission, owing to the nature of the underwater environment. In addition, because the experimental environment is poor, verifying the performance in an actual sea environment is challenging, making it necessary to prepare for emergency situations, such as the loss of the AUV.

As the guidance accuracy of the AUV increases, multiple guidance and navigation sensors must be adequately managed and utilized. In contrast to other general missions, such as exploration, docking missions require precise location estimation and maneuver, with the AUV equipped with multiple guidance and navigation sensors. Moreover, several detection sensors are installed to check for water leaks and other conditions inside the AUV. Based on these data, the

AUV and mission status should be monitored, guiding the AUV based on the situation. However, considering the vast amount of information to manage with an interrelated structure, it is difficult to respond appropriately to changes, such as system expansion or mission addition, by simply implementing the mission management concept through integrated software; the docking success rate decreases without appropriate management of the situation. In addition, considering the characteristics of each guidance sensor, the operating distance and resolution for optimal performance vary, which requires adequate management.

To address these problems, a mission management technique was implemented in this study by analyzing the operating environment and docking scenarios of the AUV and the characteristics of each guidance and inertial navigation sensor. The FIA level was defined in consideration of the characteristics of the AUV and mounted sensors, and the docking success rate was improved by effectively utilizing multiple sensors. The stability in the mission performance of the AUV was ensured by specifying the event level according to the AUV hardware and mission status. In addition, the behavior of the AUV was defined by the GP command to allow autonomous responses to various situations that could occur during docking.

3.2 Design

In this study, to implement the mission management technique for docking, the operating environment and docking scenarios of the AUV and characteristics of the navigation and guidance sensors were analyzed and classified by the FIA level, event level, and GP command. Figs. 3 and 4 show the normal or abnormal scenarios for docking the AUV. The AUV, which performs a specific mission, begins docking at the docking station or travels to an assigned point when an abnormal situation occurs, such as a missed waypoint or an abnormality in the state of the AUV, to terminate the mission or re-attempt docking.

3.2.1 FIA level

As shown in Fig. 3, the docking process of the AUV was divided into FIA stages 1 to 3. The relative distance for each stage was defined to reflect the characteristics and operating distance of the mounted guidance and inertial sensors. Based on the non-holonomic characteristics of the AUV, its attitude at the time of entering each stage was defined to increase the underwater docking success rate As shown in Fig. 4, when the AUV cannot enter a stage owing to currents, it returns to the assigned point and reattempts docking. When enteringFIA 2, the relative distance and azimuth between the AUV and

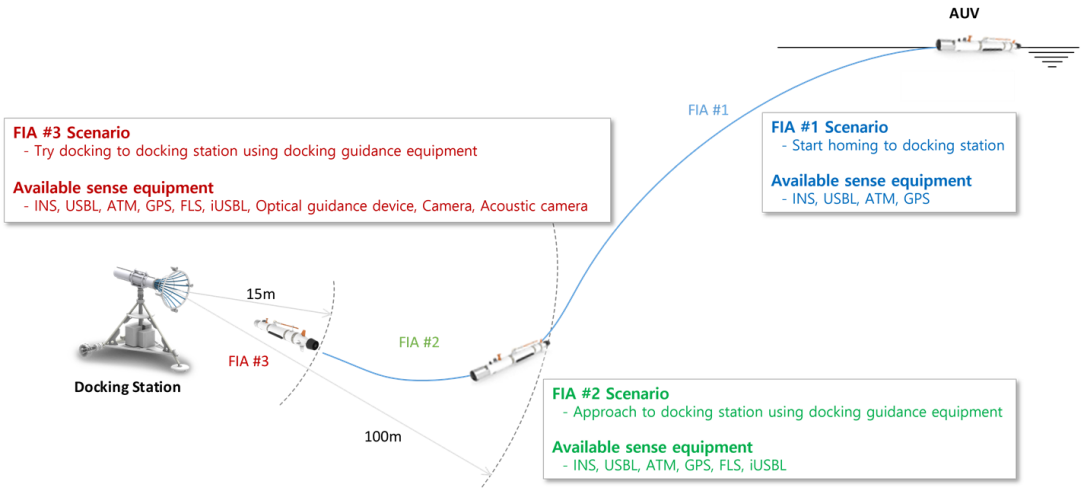

Fig. 3 Docking scenario of AUV (normal case)

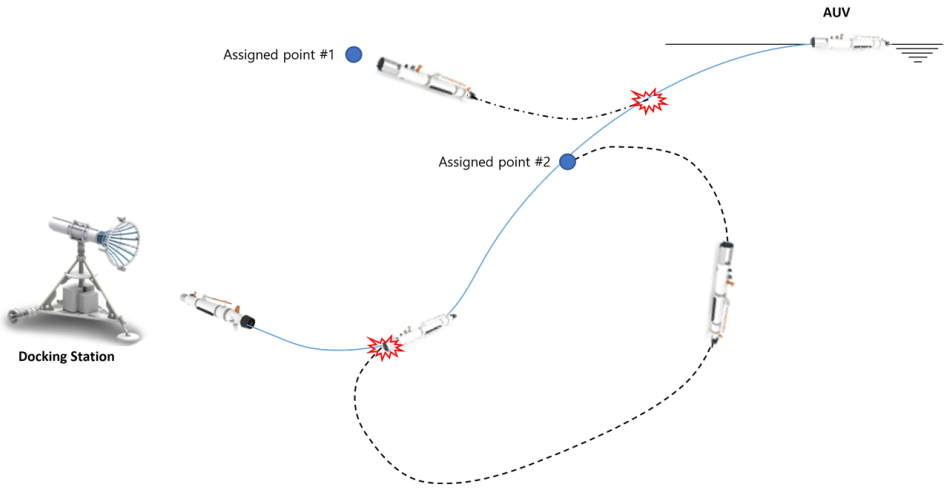

Fig. 4 Docking scenario of AUV (abnormal case)

Table 1 Definition of FIA Level up condition

Level	Level up condition
FIA 1 → FIA 2	<= 100 m, dist AUV-DS < 10 deg, ang AUV-DS Same depth with DS
FIA 2 → FIA 3	<= 15 m, dist AUV-DS < 5 deg, ang AUV-DS Same depth with DS

docking station must be 100 m and 10° or less, respectively, and the water depth must be the same. When entering FIA 3, the relative distance and azimuth must be 15 m and 5° or less, respectively, and the water depth must be the same. In the FIA 2 and 3 stages, the docking success rate is calculated at each sampling time to determine whether to attempt docking. When the success rate is calculated to be less than 80%, the AUV returns to the assigned point and reattempts docking. Table 1 lists the entry conditions for each stage.

In FIA stage 1, the AUV terminates its mission at a certain location and starts homing to a pre-specified docking station. For the approach to the docking station, the AUV estimates the location using sensors, such as the inertial navigation system (INS), ultrashort baseline (USBL), and underwater acoustic modem (ATM), while control and navigation errors are allowed at a certain level. In FIA stage 2, the AUV approaches the docking station closely using the installed guidance sensors to confirm the exact location of the docking station and maintain the accurate navigation performance for increased control precision. The docking station is detected by FLS mounted on the AUV at the relative distance of approximately 100 m, with the relative distance and azimuth estimated and corrected using iUSBL at approximately 30 m for the approach to the docking station. In FIA stage 3, the AUV attempts to dock at the docking station, requiring accurate navigation performance and precise control performance. The relative distance and azimuth between the AUV and docking station are accurately estimated and guided using precise guidance sensors, such as an optical guidance device and acoustic camera mounted on the docking station. The final call for docking is made using a camera and docking switch installed on the docking station. The sensors used in each stage are turned on/off to minimize the power consumption of the AUV.

3.2.2 Event level

The status of the AUV and mission performance were checked constantly during docking to ensure the safety of the AUV and increase the docking success rate. As listed in Table 2, the event level was defined to determine the point of return or homing in an abnormal situation, as shown in Fig. 4. Depending on the degree of damage, the priority was specified in the order of "deadly damage," "damage," "return," and "keep going." "Deadly damage" is a stage where a mission becomes impossible owing to damage to the thruster or major sensors, and the entire system stops and floats with its own buoyancy. A temporary safety function was added for the stability of the experiment, which prevented the AUV from diving into deep water owing to malfunction of the algorithm under development, rolled the AUV from the experiment support ship for a forced roll limit, and allowed the AUV to terminate the mission and float with its own buoyancy after a certain operation time to prevent its loss. "Damage" is a stage where the AUV can be operated temporarily but must be moved quickly to an assigned point owing to problems such as leaks. The AUV is moved from the current location to the surface or start point over the shortest distance to prevent accidents, such as the loss of the AUV. "Return" is when the AUV is rebooted or returned to the previous waypoint because the arrival conditions for each FIA level or waypoint are not satisfied. The number of attempts to return is set to one, which can be adjusted depending on the situation. "Keep going" is a stage in which all conditions of the AUV are acceptable, and the mission continues. A path is generated at the start of the docking mission; once a waypoint is reached, the next waypoint is updated. The GP command called at each event level is described in the following section.

A waypoint is considered to have been reached when Eq. (1) is satisfied. The distance between the AUV and current waypoint ($distanceToFrontPoint$), the distance between the AUV location and previous waypoint ($distanceToRearPoint$), and distance between the current waypoint and previous waypoint ($distanceToBetPoint$) are calculated using the Euclidean norm. $circleSize$ indicates the AUV arrival radius defined at each waypoint, which can be flexibly adjusted based on the given path. The AUV is considered to have reached the waypoint when $circleSize$ is greater than $distanceToFrontPoint$, whereas the AUV is considered to have gone past the waypoint when $distanceToRearPoint$ is greater than $distanceToBetPoint$.

Table 2 Definition of Event level

Definition	Level	Situation	Reaction
Deadly demage	Event 0	Hardware demage (actuator, equipment, etc) Operation time, roll angle, depth excess	Finish docking mission
Demage	Event 1	Water leak, collision	Move to surface point
		Low battery	Move to start point
Return	Event 2	Actuator, sensor error	Init waypoint
	Event 3	Missing waypoint and FIA level, failure docking and FIA3 entry try	Move to assigned point
Keep going	Event 4	Good condition	Keep going, Change waypoint ID, Generate waypoint

$$passCondition = \begin{cases} true, & distanceToFrontPoint \leq circleSize \\ false, & distanceToRearPoint > distanceBetPoint \end{cases} \quad (1)$$

$$distanceToFrontPoint = \| Pos_{auv} - Pos_{waypoint(ID)} \|$$
$$distanceToRearPoint = \| Pos_{auv} - Pos_{waypoint(ID-1)} \|$$
$$distanceBetPoint = \| Pos_{waypoint(ID)} - Pos_{waypoint(ID-1)} \|$$

3.2.3 GP command

Based on the state of the FIA and event levels, the behavior of the AUV was defined as listed in Table 3. Several situations that may occur during underwater docking missions were predefined, allowing the AUV to respond to each situation according to a consistent set of rules. GP 0 is called when there is no problem during docking, GP 2 is called when the target position is reached during the mission, and GP 1 is called at the end of the mission. GP 3 and GP 4 are called when a new waypoint is generated and updated, respectively, while GP 5~9 are called when the AUV must move to an assigned point. A new return point or state can be defined additionally.

Fig. 5 shows the diagram of the mission management algorithm. The state of the AUV is updated, with the FIA level checked at every moment. In addition, the status of the AUV and mission performance are confirmed, and the corresponding GP command is called. The mission continues when GP 0, 2, 3, 4, 7, 8, or 9 is called. Finally, the mission is terminated upon successful docking.

Table 3 Definition of GP command

GP command	Behavior
0	AUV initialization, keep moving
1	Stop the mission
2	Update waypoint
3	Generation of waypoint
4	Initialization of waypoint
5	Go to the surface directly with max RPM and stern angle
6	Go to the start point
7	Go to the start waypoint of FIA1
8	Go to the start waypoint of FIA2
9	Go to the start waypoint of FIA3

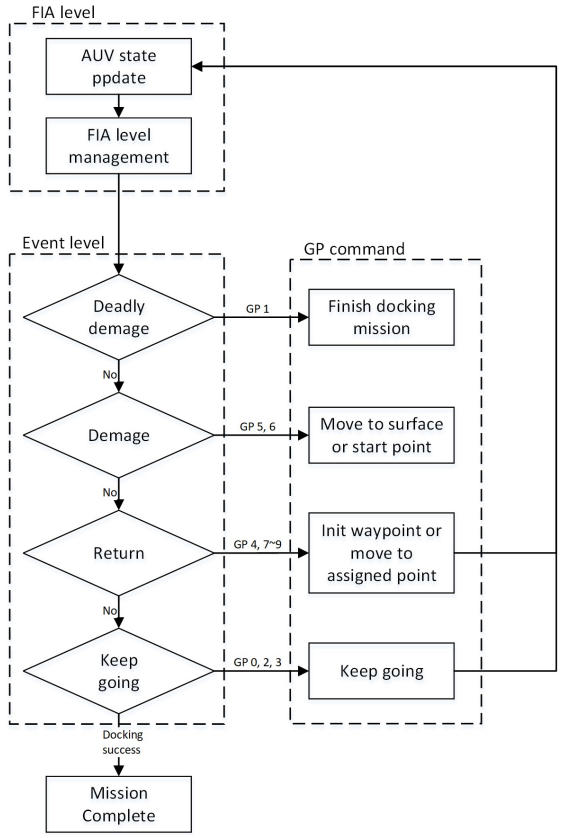

Fig. 5 Diagram of mission management

4. Experimental Studies

Experiments were conducted on land and in the actual sea environment to verify the mission management algorithm. Algorithm stability was pre-verified by simulating the sea environment on land to minimize the risk of loss or collision that could occur in the actual sea environment and verify the interconnection between the algorithms. For the convenience of the experiment in the sea environment, a simple docking station was installed to conduct the underwater docking experiment. The simple docking station simplifies the system based on the experimental environment, consisting only a docking cone and frame that holds the docking cone, making the system lightweight for easy installation and recovery.

4.1 Ground Test

An experiment was conducted on land to verify the performance and interconnection stability of the mission management algorithm in a land environment where the safety of the AUV would be guaranteed. The results of the operational decisions according to the relative distance between the AUV and docking station and the occurrence of abnormal situations were confirmed. In the experimental method, the AUV was fixed on a trolley and manually moved along seven arbitrarily determined waypoints in a straight line, as shown in Fig. 6, to simulate a normal and an abnormal movement situation (an unreached waypoint). The location of the AUV was updated using GPS instead of INS.

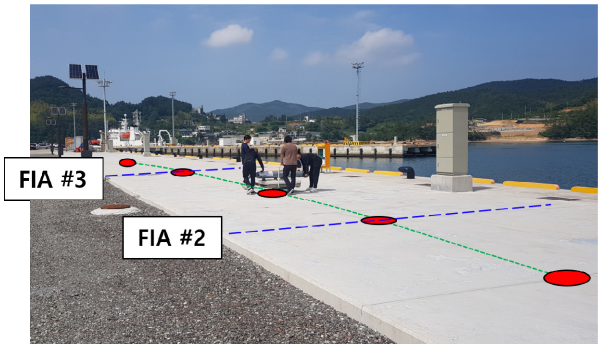

Fig. 6 Field experiment site and its method

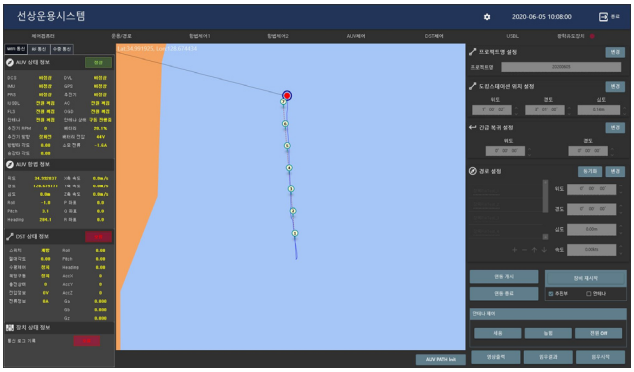

Fig. 7 Operation console for normal state

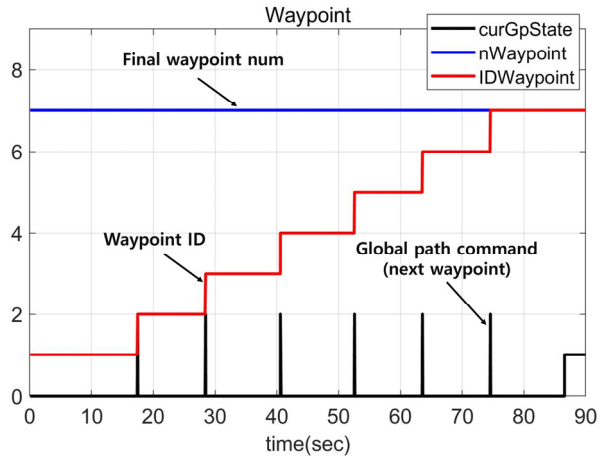

Fig. 8 Waypoint and GP command

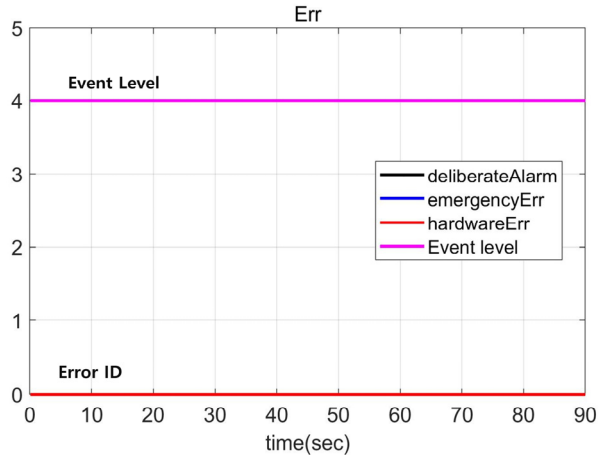

Fig. 10 Event level and error ID

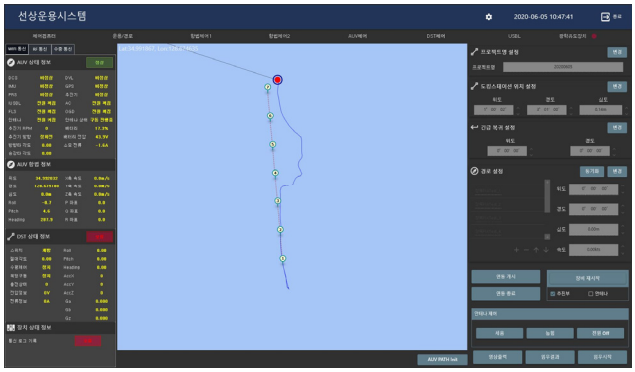

Fig. 11 Operation console for abnormal state

Fig. 7 shows the operation console used to confirm the set waypoints and path of the AUV movement. The figure shows that the AUV was moved appropriately along the preset path. The distance at each FIA stage was adjusted to 30 m owing to the limited test environment. The operation console is a system for controlling the AUV, where parameters, such as the movement path and control of the AUV, can bespecified, and the status can be monitored.

Fig. 8 shows the waypoint ID and GP command based on the distance. As the AUV passes each waypoint, GP 2 is called, and the waypoint ID is updated. Once the last waypoint is reached, GP 1 is called, and the mission is terminated. Fig. 9 shows that each sensor is turned on/off depending on the FIA level and relative distance. Fig. 10 shows the event level and error ID. DeliberateAlarm and HardwareErr correspond to the "deadly damage" stage of the event level, and EmergencyErr refers to the "damage" and "return" stages. Considering the AUV is operating normally along the specified path, Event 4 is called until the mission is completed.

Fig. 11 shows the result of simulating the abnormal state in which

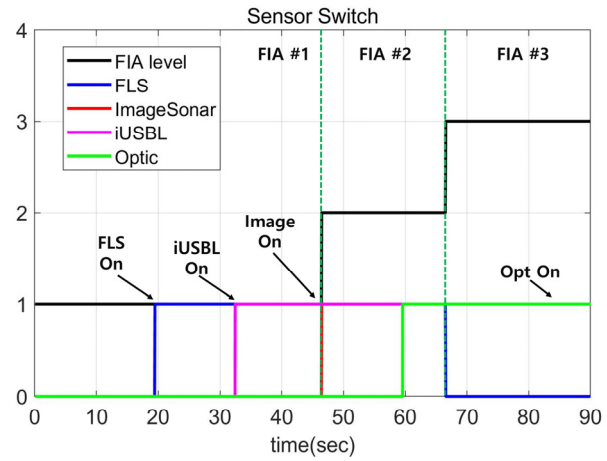

Fig. 9 Sensor activation depending on FIA and range

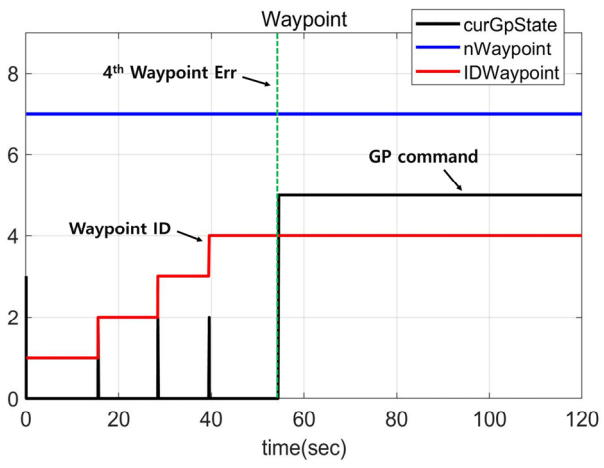

Fig. 12 Waypoint and GP command

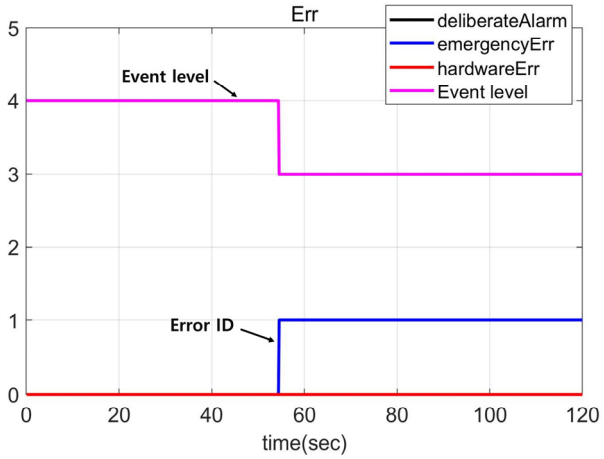

Fig. 13 Event level and error ID

the AUV does not pass a set waypoint. As shown in Fig. 12, because waypoint #4 is not reached, the waypoint ID is maintained at 4. The algorithm determines that the AUV has missed waypoint #4 and calls GP 5. As shown in Fig. 13, the errorID for an unreached waypoint (emergencyErr) is triggered, and Event 3 is called. The algorithm was partially modified later to allow the AUV to float to the surface if a waypoint was not reached to prevent the loss of the AUV in the subsequent underwater experiment.

As a result of testing the mission management algorithm on land, the adequate interconnection of the algorithm with the other algorithms was confirmed, with the FIA level, event level, and GP command accurately determined based on the situation.

4.2 Sea Test

After verifying the performance of interconnection with the internal software of the AUV and the basic operational performance on land, an experiment was conducted in the actual sea environment, as shown in Fig. 14, to verify the docking performance of the AUV. To prevent the loss of the AUV, the AUV was attached to fishing lines, followed by the experiment support ship.

Fig. 14 Real sea experiment site

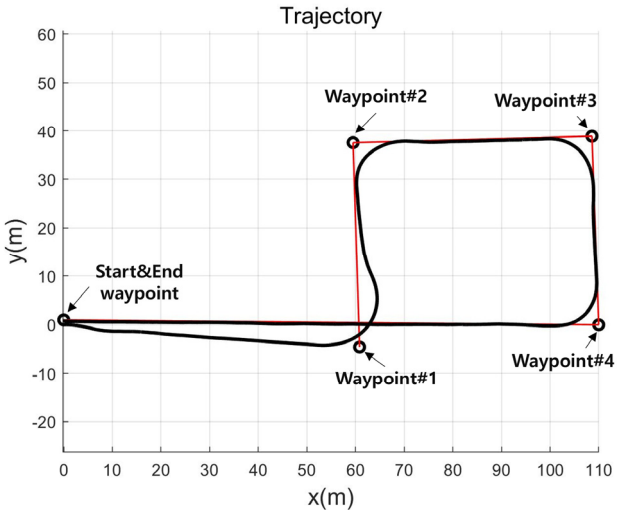

Fig. 15 Waypoint and trajectory of AUV

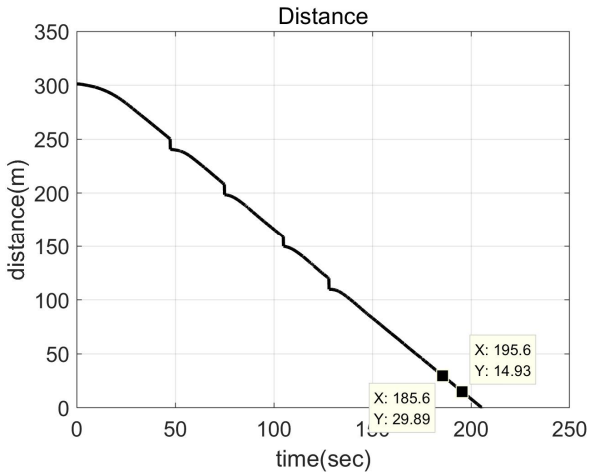

(a)

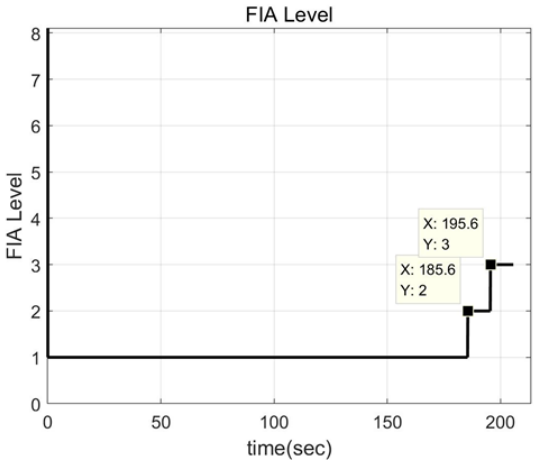

(b)

Fig. 16 Distance between AUV and docking station

As shown in Fig. 15, five waypoints in the shape of a square, excluding the start point, were considered as the waypoints for the AUV. The AUV arrived at the final location without deviating or

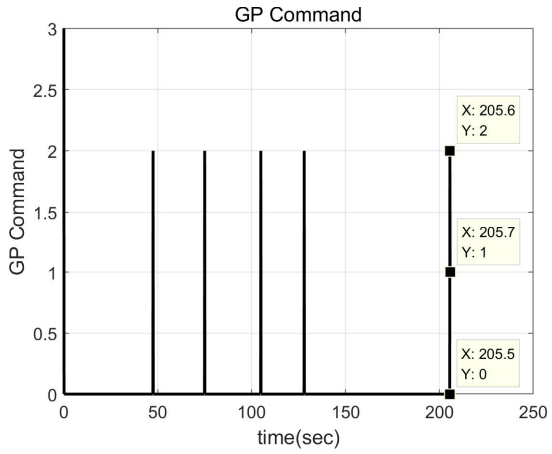

Fig. 17 GP command

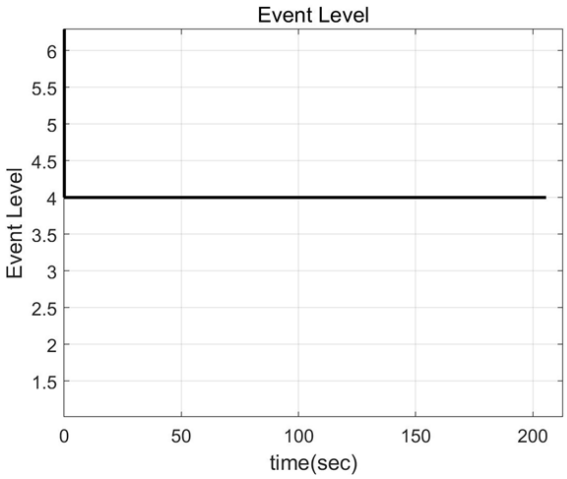

Fig. 18 Event level

missing a waypoint. Eq. (1) was used to determine the arrival at each waypoint, and , which refers to the arrival radius at each waypoint, $circleSize$ was separately defined. Waypoint#1 to waypoint#4 were set to 10 m to consider the operating conditions, such as the AUV's rotation radius and movement stability, and end waypoint was set to 0.2 m to consider the size of the docking cone as the final docking point.

Subsequent to the input of the preset initial value shown in Fig. 16 (a), the FIA level was observed to be properly managed according to the distance between the AUV and final waypoint (docking station), as shown in Fig. 16 (b). The AUV entered the 30 m radius in 185.6 s, with the FIA level was changed to FIA 2. When the AUV entered the 15 m radius at 195.6 s, the FIA level was changed to FIA 3. Fig. 17 shows the adequate management of the GP command as the AUV passed through the specified waypoints. The change of the waypoints and the normal operation were confirmed until 205.5 s, with the arrival at the last waypoint confirmed at 205.6 s. At 205.7 s, the mission complete GP command was called. Fig. 18 shows that the event level was properly managed during the docking mission. After setting the initial value, the normal state of the AUV was maintained.

As a result of testing the mission management algorithm in the actual sea environment, it was confirmed that the FIA level, event level, and GP command were accurately determined based on the situation. In the actual sea experiment, the abnormal state was not tested owing to safety issues of the AUV.

When the adequate operation of the mission management algorithm was confirmed, five differently shaped paths were each attempted twice with a total of 10 docking attempts (Fig. 19). As a result, docking was successful in all the attempts, achieving a success rate of 100%.

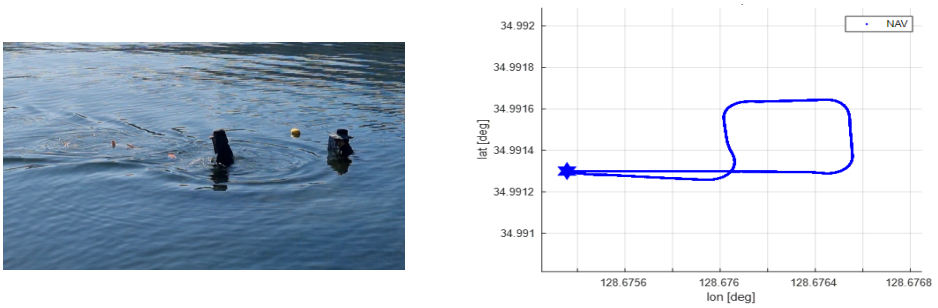

1st docking try (success)

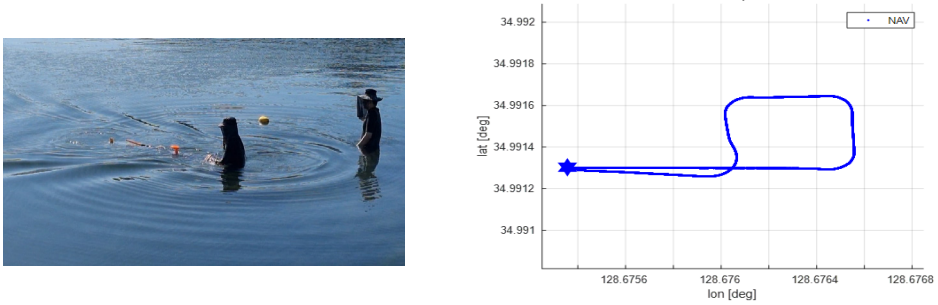

2nd docking try (success)

Fig. 19 Docking try

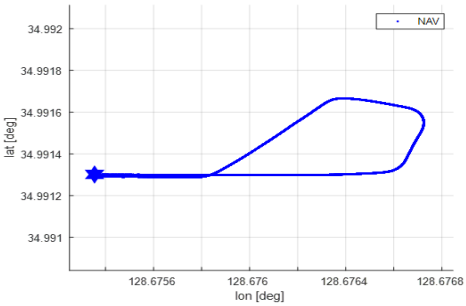

3rd docking try (success)

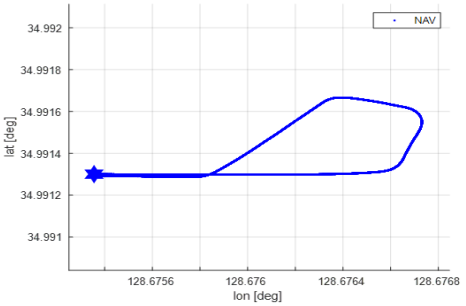

4th docking try (success)

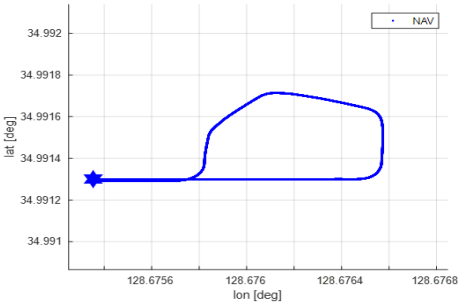

5th docking try (success)

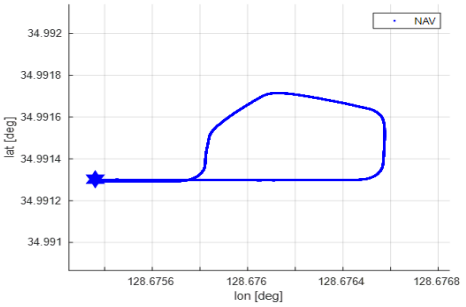

6th docking try (success)

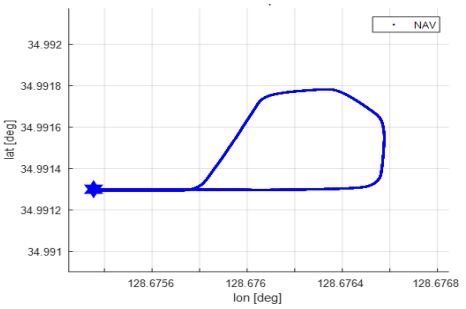

7th docking try (success)

Fig. 19 Docking try (Continuation)

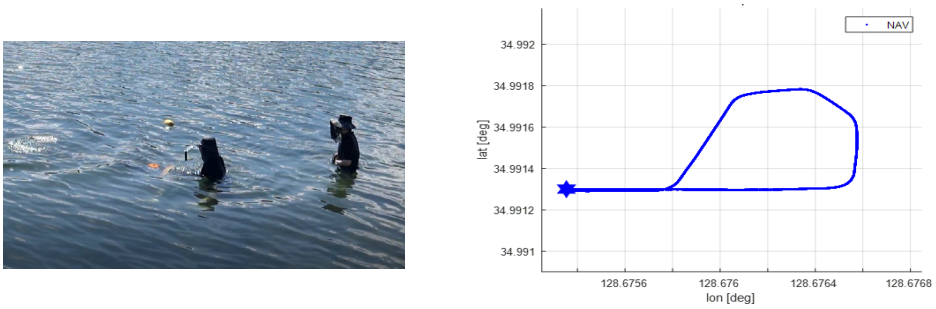

8th docking try (success)

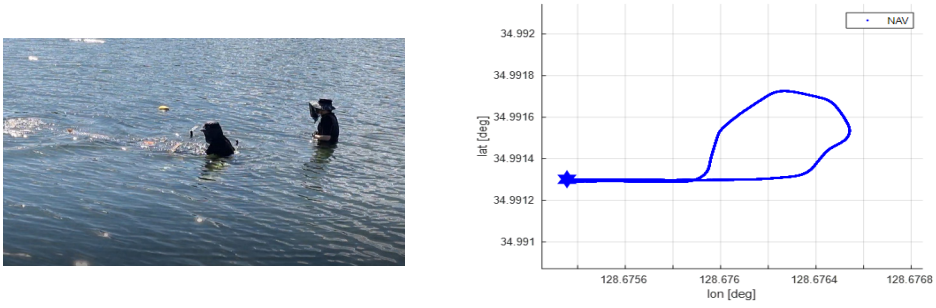

9th docking try (success)

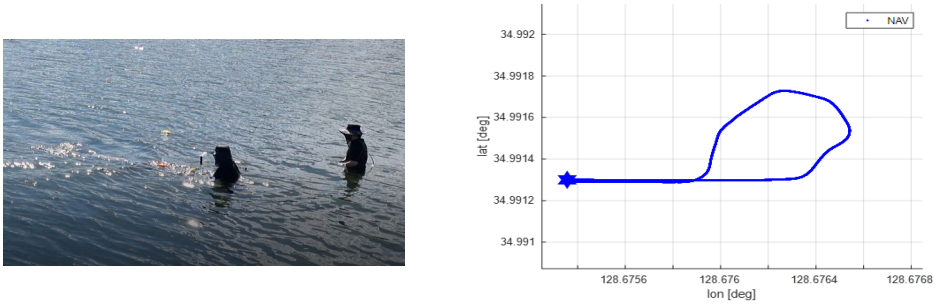

10th docking try (success)

Fig. 19 Docking try (Continuation)

5. Conclusions

While AUVs must perform missions without external intervention given the constraints of the operating environment, USVs have been used in previous studies to allow operators to intervene under limited conditions. In addition, considering the nature of docking missions that require precise location estimation and maneuver, AUVs are equipped with multiple guidance and navigation sensors and state detection sensors, making the hardware and software structures of the AUVs complex, in contrast to those of conventional AUVs. The AI planner was not used in the mission management technique in this study because it would involve several constraints for the application in the AUV used in the experiment. In this study, a mission management technique was introduced to efficiently utilize and manage various sensors to perform docking missions without external intervention. The proposed technique defined the FIA level, event level, and GP command by reflecting the operating environment and docking scenarios of the AUV. The different sensors were effectively utilized, and the docking success rate was increased by defining the FIA level based on the characteristics of the AUV and mounted sensors. In addition, the event level was specified based on the hardware and mission status of the AUV to ensure stability in the mission performance of the AUV. Finally, it was possible to autonomously respond to various situations that could occur during docking by defining the behavior of the AUV with the GP command based on the situation. The adequate operation of the proposed algorithm was verified on land and in a real sea environment. In addition, by achieving a docking success rate of 100% (10 out of 10 attempts) in the sea environment, the problem of low docking success rates observed in previous studies was addressed, while the operability in an actual sea environment was demonstrated. However, given the safety issues of the AUV, certain situations were excluded and not verified experimentally. We plan to supplement the algorithm and verify the stability of the mission management algorithm under various conditions through additional experimental scenarios by February 2022.

Conflict of Interest

No potential conflict of interest relevant to this article was reported.

Funding

This research was supported by the project No. 17-CM-RB-16 titled “Development of Multi-sensor Fusion based AUV’s Terminal Guidance and Docking Technology,” funded by the Agency for Defense Development (ADD) in the Korea; in addition, it was partially supported by the project titled 'Development of unmanned remotely construction aided system for harbor infrastructure', funded by the Ministry of Oceans and Fisheries, Korea.

References

Cho, G.R., Kang, H., Lee, M. J., & Li, J.H. (2019). Heading Control of URI-T, an Underwater Cable Burying ROV: Theory and Sea Trial Verification. Journal of Ocean Engineering and Technology, 33(2), 178–188. https://doi.org/10.26748/KSOE.2019.010

Kim, M.G., Kang, H., Lee, M.J., Cho, G.R., Li, J.H., & Kim, C. (2021). UUV Platform Optimal Design for Overcoming Strong Current. Journal of Ocean Engineering and Technology, 35(6), 434-445. https://doi.org/10.26748/KSOE.2021.069

Cho, Y., Kim, J., Kim, J., Jo, Y., & Ryu, J. (2019). Behavior-based Control Considering the Interaction Between a Human Operator and an Autonomous Surface Vehicle. Journal of Ocean Engineering and Technology, 33(6), 620–626.

Cho, G.R., Kang, H.J., Lee, G.H., & Lee, P.Y. (2020a). Underwater Docking and Control Strategy for Torpedo-type Autonomous Underwater Vehicle. Bulletin of the Society of Naval Architects of Korea, 57(3), 19–23.

Park, D.G., Cho, G.R., Kang, H.J., Li, J.H., Lee, P.Y., Kim, H.S., & Lee, H.S. (2019). Waypoint Tracking Control Using Line of Sight Guidance Law for Torpedo Type AUV. Proceedings of Fall Conference 2019 of the Korean Marine Robot Technology Society, 61–63.

Fukasawa, T., Noguchi, T., Kawasaki, T., & Baino, M. (2003). “MARINE BIRD”, a New Experimental AUV with Underwater Docking and Recharging System. In Oceans 2003. Celebrating the Past... Teaming Toward the Future (IEEE Cat. No. 03CH37492), 4, 2195–2200. https://doi.org/10.1109/OCEANS.2003.178242

Kimball, P.W., Clark, E.B., Scully, M., Richmond, K., Flesher, C., Lindzey, L.E., ... & Stone, W.C. (2018). The ARTEMIS Under-Ice AUV Docking System. Journal of field robotics, 35(2), 299–308. https://doi.org/10.1002/rob.21740

Hobson, B.W., McEwen, R.S., Erickson, J., Hoover, T., McBride, L., Shane, F., & Bellingham, J.G. (2007). The Development and Ocean Testing of an AUV Docking Station for a 21" AUV. In OCEANS 2007, 1–6. https://doi.org/10.1109/OCEANS.2007.4449318.

Zhang, T., Li, D., & Yang, C. (2017). Study on Impact Process of AUV Underwater Docking with a Cone-Shaped Dock. Ocean Engineering, 130, 176–187. https://doi.org/10.1016/j.oceaneng.2016.12.002

Allen, B., Austin, T., Forrester, N., Goldsborough, R., Kukulya, A., Packard, G., ... & Stokey, R. (2006). Autonomous Docking Demonstrations with Enhanced REMUS Technology. In OCEANS 2006, 1–6. 10. https://doi.org/1109/OCEANS.2006.306952.

Li, Y., Jiang, Y., Cao, J., Wang, B., & Li, Y. (2015). AUV Docking Experiments Based on Vision Positioning Using Two Cameras. Ocean Engineering, 110, 163–173. https://doi.org/10.1016/j.oceaneng.2015.10.015

Wolf, M.T., Rahmani, A., de la Croix, J.P., Woodward, G., Vander Hook, J., Brown, D., ... & Sandoval, M. (2017, May). CARACaS Multi-Agent Maritime Autonomy for Unmanned Surface Vehicles in the Swarm II Harbor Patrol Demonstration. Proceedings of SPIE 10195, Unmanned Systems Technology XIX, 101950O. https://doi.org/10.1117/12.2262067

Albiez, J., Joyeux, S., & Hildebrandt, M. (2010, September). Adaptive AUV Mission Management in Under-Informed Situations. In OCEANS 2010 MTS/IEEE SEATTLE, 1–10. https://doi.org/10.1109/OCEANS.2010.5664350

Barrouil, C., & Lemaire, J. (1999, September). Advanced Real-Time Mission Management for an AUV. In SCI NATO RESTRICTED Symposium on Advanced Mission Management and System Integration Technologies for Improved Tactical Operations, 114.

Pinto, J., Sousa, J., Py, F., & Rajan, K. (2012, October). Experiments with Deliberative Planning on Autonomous Underwater Vehicles. In IROS 2012 Workshop on Robotics for Environmental Monitoring, Vilamoura, Portugal.

Xue, L., & Lekkas, A.M. (2020, October). Comparison of AI Planning Frameworks for Underwater Intervention Drones. In Global Oceans 2020: Singapore–U.S. Gulf Coast, 1–9. https://doi.org/10.1109/IEEECONF38699.2020.9388994.

Papadimitriou, G., & Lane, D. (2014) Semantic Based Knowledge Representation and Adaptive Mission Planning for MCM Missions Using AUVs. In OCEANS 2014-TAIPEI, 1–8, https://doi.org/10.1109/OCEANS-TAIPEI.2014.6964477

Kim, H.S., Lee, H.S., Lee, P.Y., & Choi, D.H. (2018). UUV and underwater navigation system design for guiding UUV to Docking-Station. Proceedings of Korea Institute of Military Science and Technology Conference 2018.

Li, J.H., & Lee, P.M. (2009, August). Path Tracking in Dive Plane for a Class of Torpedo-Type Underactuated AUVs. Proceedings of 2009 7th Asian Control Conference, 360–365.

Kim, H.S., Lee, H.S., Lee, P.Y., Kim, Y.G., Cho, G.R., Park, D.G., ... Choi, H.S. (2019). Development and Test of UUV Docking

Technology. Korean Marine Robot Technology Society Conference 2019.

Choo, J., Lee, G., Lee, P.Y., Kim, H.S., Lee, H., Park, D., & Lee, J. (2020). Position Based In-Motion Alignment Method for an AUV. Journal of Institute of Control, Robotics and Systems, 26(8), 649–659.

Cho, G.R., Li, J.H., Park, D., & Jung, J.H. (2020b). Robust Trajectory Tracking of Autonomous Underwater Vehicles Using Back-Stepping Control and Time Delay Estimation. Ocean Engineering, 201, 107131. https://doi.org/10.1016/j.oceaneng.2020.107131

Author ORCIDs

Author name	ORCID
Kang, Hyungjoo	0000-0001-8838-3285
Cho, Gun Rae	0000-0002-8536-4844
Kim, Min-Gyu	0000-0001-8517-6352
Lee, Mun-Jik	0000-0001-7806-3237
Li, Ji-Hong	0000-0002-5162-2737
Kim, Ho Sung	0000-0002-5706-3163
Lee, Hansol	0000-0003-4367-5035
Lee, Gwonsoo	0000-0002-0507-7758

KSOE

Review Article

Journal of Ocean Engineering and Technology 36(3), 194-210, June, 2022
https://doi.org/10.26748/KSOE.2022.007

pISSN 1225-0767
eISSN 2287-6715

Review on Applications of Machine Learning in Coastal and Ocean Engineering

Taeyoon Kim[1] and Woo-Dong Lee[2]

[1]*Research Professor, Institute of Marine Industry, Gyeongsang National University, Tongyeong, Korea*
[2]*Associate Professor, Department of Ocean Civil Engineering, Gyeongsang National University, Tongyeong, Korea*

KEY WORDS: Machine learning, Data-driven model, Coastal engineering, Prediction, Sensitivity analysis

ABSTRACT: *Recently, an analysis method using machine learning for solving problems in coastal and ocean engineering has been highlighted. Machine learning models are effective modeling tools for predicting specific parameters by learning complex relationships based on a specified dataset. In coastal and ocean engineering, various studies have been conducted to predict dependent variables such as wave parameters, tides, storm surges, design parameters, and shoreline fluctuations. Herein, we introduce and describe the application trend of machine learning models in coastal and ocean engineering. Based on the results of various studies, machine learning models are an effective alternative to approaches involving data requirements, time-consuming fluid dynamics, and numerical models. In addition, machine learning can be successfully applied for solving various problems in coastal and ocean engineering. However, to achieve accurate predictions, model development should be conducted in addition to data preprocessing and cost calculation. Furthermore, applicability to various systems and quantifiable evaluations of uncertainty should be considered.*

1. Introduction

Humans have attempted to understand various phenomena that occur in the sea many years ago. However, these phenomena are difficult to elucidate even after several centuries because of complex interactions involving physical, chemical, and biological processes (Dawarakish et al., 2013). Hence, various methods have been formulated through statistical analysis, spectrum analysis, time series analysis, empirical formulas based on mathematical model experiments, and other mathematical and physical analyses. However, the derivation of accurate results is limited owing to the complex interrelationships among numerous parameters in nature (Goldstein et al., 2019).

As we enter the era of the Fourth Industrial Revolution, machine learning (ML) models that identify and predict statistical structures from input and output data using computers to solve numerous engineering problems in the natural world are garnering significant attention. ML, a field of artificial intelligence (AI), is an inductive method that identifies rules through learning using data and results, instead of using a conventional program method that derives results from rules and data. ML techniques can easily solve complex engineering problems and enable the regression analysis of nonlinear relationships. ML demonstrates clear advantages over other conventional regression methods because it adopts a specific algorithm that can learn from the input data and provides accurate results via the output (Salehi and Burgueño, 2018). ML-based predictive models include various algorithms such as neural networks, decision trees, support vector machines (SVM), and gradient boosting (GBR). In coastal engineering, studies based on ML-based algorithms are increasingly conducted to predict wave formation, wave breaking, tidal changes, hydraulic properties around structures, and changes in beach profiles (Deo and Jagdale, 2003; Panizzo and Briganti, 2007; Kankal and Yuksek, 2012).

This paper introduces ML models and reviews various studies that predict significant parameters in coastal engineering such as waves, wave breaking, hydraulic properties around structures, and beach profile changes. This paper focuses on regression analysis studies that involve continuous variables for parameters during the supervised learning of ML models, whereas studies pertaining to classification involving categorical variables are omitted. Furthermore, the basic concepts and basic contents of various ML models are introduced, and the technological trends and application examples of ML models in the coastal engineering field are described.

Received 30 March 2022, revised 26 April 2022, accepted 26 May 2022
Corresponding author Woo-Dong Lee: +82-55-772-9126, wdlee@gnu.ac.kr

2. Machine Learning Model

As we enter the era of the Fourth Industrial Revolution, interest in AI and ML is increasing. ML, which is a field of AI, trains computers human thinking and cognition methods such that the computers can perform recognition and inference on their own without preset judgment criteria for all variables. General ML algorithms include supervised learning, unsupervised learning, and reinforcement learning (Fig. 1). Two supervised learning models exist: regression and classification. Data classification and prediction are determined based on the characteristics of both the input and dependent variables. Representative supervised learning algorithms include artificial neural network (ANN), SVM, and random forest (RF). Unsupervised learning is a method of predicting results for new data by clustering patterns or features from unlabeled data. It is primarily used for clustering and dimensionality reduction, e.g., k-means clustering and principal component analysis. This paper focuses on the application cases of coastal and marine engineering for supervised learning among ML algorithms.

2.1 Linear Regression (LR) Model

The LR model uses linear parameters and offers easy and quick analyses. The LR model was developed more than a century ago and has been widely used over the past few decades. However, it yields low accuracy results for data that exhibit nonlinear relationships. LR generates a regression model using one or more features and obtains parameters w and b that minimize the mean squared error (MSE) between the experimental value (y) and predicted value ($\hat{y}$) (Eqs. (1)–(2)).

$$\hat{y} = w[0] \times x[0] + w[1] \times x[1] + \ldots + w[p] \times x[p] + b \tag{1}$$

$$MSE = \frac{1}{n}\sum_{i=1}^{n}\left(y_i - \hat{y}_i\right)^2 \tag{2}$$

2.1.1 Lasso regression

In some cases, the conventional LR method results in overfitting, i.e., the predictive performance is unsatisfactory when new data are provided. Hence, lasso regression was developed, which limits models by force using the L1 regulation, as follows (Eq. (3)):

$$E = MSE + penalty = \frac{1}{n}\sum_{i=1}^{n}\left(y_i - \hat{y}_i\right)^2 + \alpha\sum_{j=1}^{m}\left|w_j\right| \tag{3}$$

where m is the number of weights, and α is the $penalty$ parameter. This equation obtains w and b that minimize the sum of the MSE and $penalty$.

2.1.2 Ridge regression

Ridge regression is a model in which the L2 regulation term is added to solve the overfitting problem of the LR model. This model not only fits the data of the learning algorithm, but also ensures that the weights of the model are minimized (Eq. (4)).

$$E = MSE + penalty = \frac{1}{n}\sum_{i=1}^{n}\left(y_i - \hat{y}_i\right)^2 + \alpha\frac{1}{2}\sum_{j=1}^{m}\left|w_j\right|^2 \tag{4}$$

The difference between lasso regression and ridge regression is that the weights are zero in lasso, whereas in ridge, the weights are approximately zero but not exactly zero. Hence, the lasso regression offers high accuracy only if some of the input variables are important, whereas the accuracy of the ridge model will be high if the importance of the input variables is similar in general.

2.2 ANN

An ANN is an information processing structure in the form of a network modeled based on the human nervous system, where simple functional processors are interconnected on a large scale. The

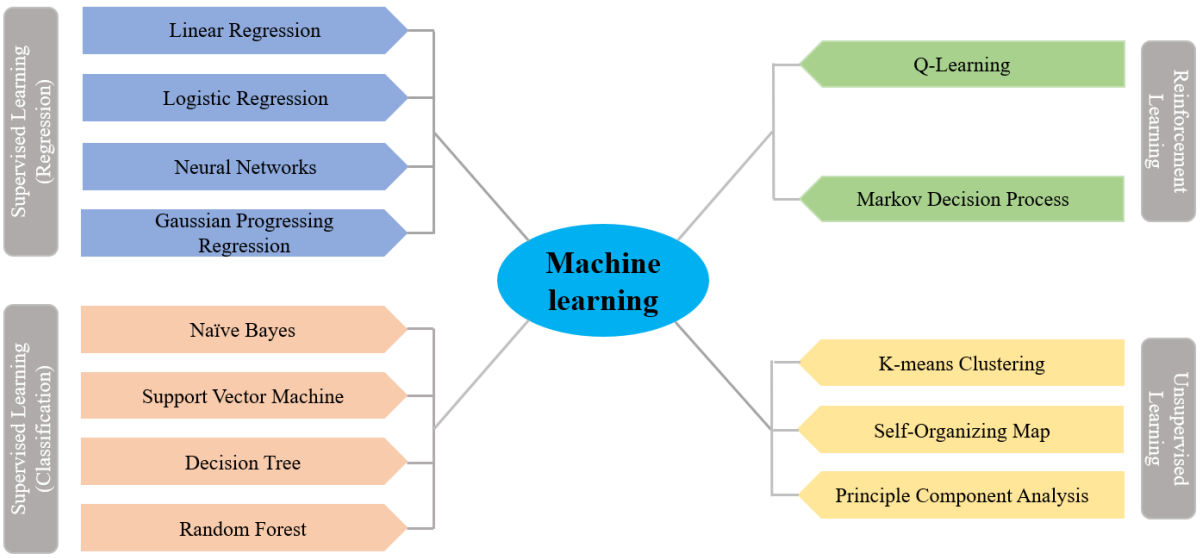

Fig. 1 Machine learning algorithms (Liu et al., 2021)

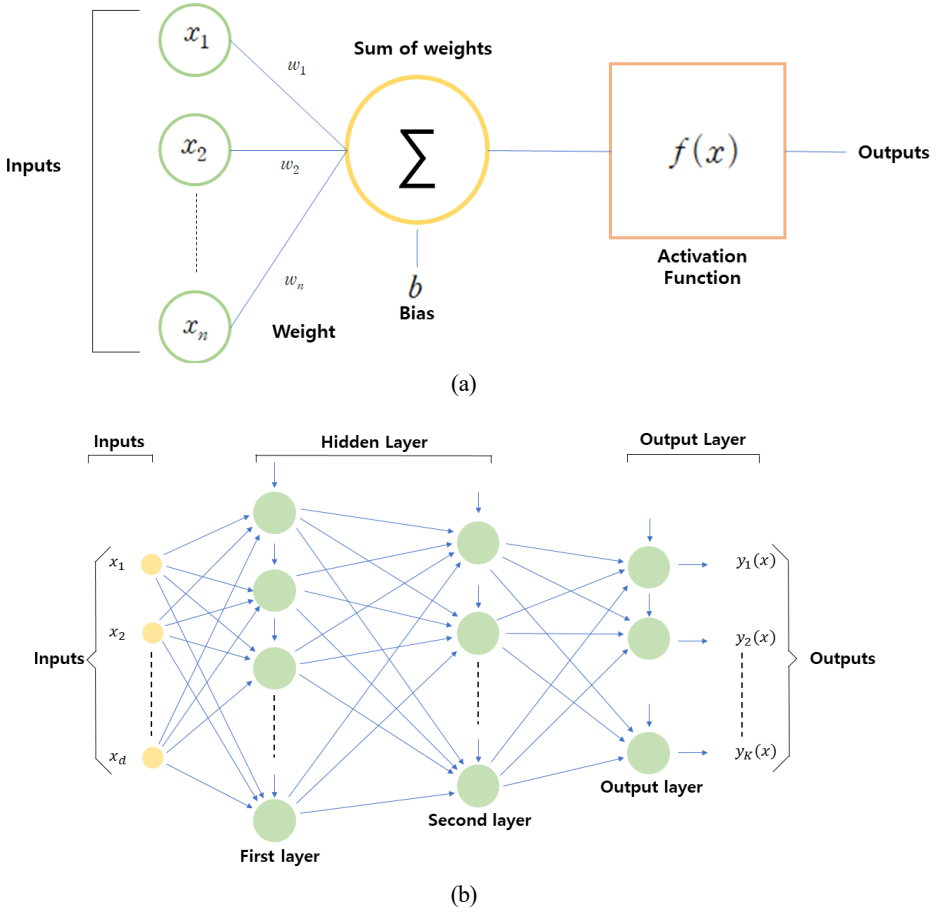

Fig. 2 Artificial neural network: (a) Neural network diagram of element; (b) typical layout of neural network

perceptron, which is the basis of deep learning, is a structure designed to deliver information based on a threshold by issuing a weighting signal for input values through the imitation of neuron behaviors in brain cells. Fig. 2 shows the structure of a neural network. A neural network comprises an input layer, a hidden layer, and an output layer, and its nodes are interconnected by weights. In an ANN, the values are transmitted from the input layer to all nodes of the hidden layer in a feedforward method. Moreover, the output values of all nodes of the hidden layer are transmitted to all nodes via the coupling and activation functions. Learning proceeds by redistributing weights between neurons through the backpropagation algorithm such that they converge in a direction in which the errors are reduced to minimize the difference between the predicted and experimental values.

In the data processing process of the neural network, each node multiplies the input value by a weight and then passes the output value through the activation function to the next node to output the result, as expressed in Eq. (5).

$$N_j = \sum_{i=1}^{N_i} w_{ij} x_i + \theta_j \tag{5}$$

where w is the weight, θ the bias, and x the input value.

The activation function renders the neural network nonlinear and enables a nonlinear analysis of the result calculated from the coupling function via the calculation of the activation function, which is a nonlinear function. Furthermore, the activation function is key for adjusting the gradient during activation training. Various activation functions are used in neural networks, including the linear, sigmoid, tanh, exponential, softmax, rectified linear unit (ReLU), ELU (Exponential Linear Unit), and SELU(Scaled Exponential Linear Unit) functions.

2.3 SVM

The SVM was introduced by Boser et al. (1992), who were inspired by the concept of statistical learning theory. SVM regression performs training to include the maximum amount of data within the specified margin error limit line. The limit line adjusts the width of the margin based on the hyperparameter. Here, the margin implies the distance between the grain boundary and support vector. The procedure of applying the SVM to the regression problem is as follows (Eqs. (6)–(7)). First, the dataset for training is distinguished.

$$\{(x_1, y_1), \ldots (x_n, y_n)\},\ x \in R_n,\ y \in r \tag{6}$$

where x is the input variable, y the output variable, R_n the n-dimensional vector space, and r the one-dimensional vector space.

The loss function of $\varepsilon^{\in sensitive}$ can be expressed as follows:

$$L_{\varepsilon}(y)=0 \text{ For } |f(x)-y|<\varepsilon \text{ or } L_{\varepsilon}(y)=|f(x)-y|-\varepsilon \tag{7}$$

Based on the equation above, if the predicted value is within the expected range, then the loss function is 0; if the predicted value is outside the expected range, then the loss function of $\varepsilon^{\in sensitive}$ is defined such that the loss is equal to the absolute value of the standard deviation minus ε. The main purpose of the vector machine is to provide the deviation of ε in the actual output value and to obtain a uniform function $f(x)$.

Finally, $f(x)$ can be expressed as follows (Eqs. (8)–(9)):

$$f(x)=\sum_{i=1}^{nsv}(\alpha_i-\alpha_i^*)K(x_i,x_j)+b \tag{8}$$

$$K(x_i,x_j)=\exp\left(-\frac{\|x_i-x_j\|^2}{2\sigma^2}\right) \tag{9}$$

where α_i and α_i^* are Lagrangian coefficients, and $K(x_i,x_j)$ represents the kernel function. In general, homogeneous polynomials, polynomial kernels, Gaussian radial basis functions, and hyperbolic tangent functions are used as the kernel function.

2.4 Gaussian Process Regression (GPR)

The Gaussian process regression (GPR) model is a probability model based on nonparameteric kernels. The Gaussian process $f(x)$ is a set of random variables $f(x)$ in the range of $\{(x_i,y_i);\, x_i\in R^d\}$, where a finite number of randomly selected variables, $f(x_1),\ldots,f(x_m)$, among them exhibits a combined Gaussian density (Na et al., 2017). The GPR model for the new input vector ($x_{\neq w}$) and training data predicts $y_{\neq w}$. The linear regression model is expressed as follows:

$$y=x^{\top}\beta+\varepsilon \tag{10}$$

where $\varepsilon\sim N(0,\sigma^2)$, and the error variance (σ^2) and coefficient (β) are calculated based on data. The GPR model describes predictions by introducing potential variables in the Gaussian process $f(x_i)$, $i=1,2,\ldots,n$ and the explicit basic function $h(x)$. The covariance function of the hidden variable provides flexibility to the response, and the basic function transmits the input of x to the p-dimensional feature space. The Gaussian process is a random variable set that comprises a finite number of Gauss distributions. If $\{f(x),\ x_i\in R^d\}$ is a Gaussian process and n contains the observed values $x_1,x_2,\ldots,x_n$, then the random variables $f(x_1),f(x_2),\ldots,f(x_n)$ exhibits a Gaussian distribution. The Gaussian process is defined by the mean function ($m(x)$) and covariance function ($k(x,x')$).

$$m(x)=E(f(x)) \tag{11}$$

$$k(x,x')=E[(f(x)-m(x))(f(x')-m(x'))] \tag{12}$$

$$f(x)\sim GP(m(x),k(x,x')) \tag{13}$$

$$h(x)^{\top}\beta+F(x) \tag{14}$$

Here, $h(x)$ is a basic function set that transmits the existing feature vector x of R^d to the new feature vector $h(x)$.

$$P(y_i|f(x_i),x_i)\sim N(y_i|h(x_i)^{\top}\beta+f(x_i),\sigma^2) \tag{15}$$

Therefore, the GPR model can be represented as a probabilistic model as in Eq. (15), and the hidden variable $f(x_i)$ is introduced to observe each x_i (Koo et al., 2016).

2.5 Ensemble Method

The ensemble method is developed to improve the performance of the classification and regression tree. It generates an accurate prediction model by creating several classifiers and combining their predictions. In other words, it is a method of deriving a high-accuracy prediction model by combining several weak classifier models, instead of using a single strong model.

The ensemble models can be primarily categorized into bagging and boosting models. Bagging is a method of reducing variance using the averaging or voting method on the results predicted using various models, whereas boosting is a method of creating strong classifiers by combining weak classifiers.

2.5.1 RF

RF is a method of improving the large variance of the decision tree and the large performance fluctuation range. It combines the concept and properties of bagging with randomized node optimization to overcome the disadvantages of existing decision trees and improves generalization. The process of extracting bootstrap samples and generating a decision tree for each bootstrap sample is similar to bagging. However, it is different from the conventional decision tree in that a method of randomly extracting predictors and creating an optimal split within the extracted variables is used instead of selecting the optimal split within all predictors for each node (Kim et al., 2020). In other words, RF combines the randomization of predictors while determining slightly different training data through bootstrap to obtain maximum randomness. Hence, several low-importance learners are created. The important hyperparameters used in an RF include max_features, bootstrap, and n_estimator. The max_features parameter refers to the maximum number of features to be used in each node. The bootstrap allows redundancy in data sampling conditions for each classification model. The n_estimator refers to the number of trees to be created in the model (Kim and Kim, 2020).

2.5.2 Boosting method

Boosting is a technique for creating a strong classifier from a few

weak classifiers. It is a model created by boosting weights on data at the boundary. The adaptive boosting (AdaBoost) algorithm is the most typically and widely used algorithm among ensemble learning methods. Specifically, it is one of the boosting series in ensemble learning. In AdaBoost, after a weak classifier is generated using the initial training data, the distribution of the training data is adjusted based on the prediction performance afforded by the training of the weak classifier. The weight of the training sample with low prediction accuracy is increased using the information received from the classifier in the previous stage. In other words, the training accuracy is improved by adaptively changing the weights of samples with low prediction accuracy in the previous classifier. Finally, a strong classifier with slightly better performance is created by combining these weak classifiers with low prediction performance. GBR is a method of sequentially adding multiple models such as the AdaBoost model. The most significant difference between the two algorithms is the method by which they recognize weak classifiers. AdaBoost recognizes values that are more difficult to classify by weighting them. By contrast, GBR uses a loss function to classify errors. In other words, the loss function is an index that can evaluate the performance of the model in learning specific data, and the model result can be interpreted based on the loss function used.

AdaBoost can be used for both classification and regression. In general, when a regression problem is considered, the training data set can be expressed as follows:

$$\phi = \{(X_1, Y_1), (X_2, Y_2), \ldots, (X_m, Y_m)\} \tag{16}$$

where $(X_i, Y_i)(i = 1, \ldots, m)$ is the ith sample of the training dataset, m the total number of samples, X_i the input data vector value, and Y_i the output data value.

Next, we can train a weak classifier $G(X)$ using a specific learning algorithm, and the relative prediction error e_i of each sample is expressed as follows:

$$e_i = L(Y_i, G(X_i)) \tag{17}$$

where $L(\bullet)$ is the loss function. In general, three options are available: linear loss, square loss, and exponential loss. For a simple explanation, the linear loss is applied as follows:

$$e_i = \frac{|Y_i - G(X_i)|}{E} \tag{18}$$

where $E = \max|Y_i - G(X_i)|$ is the maximum absolute error of all samples.

The performance of one weak classifier will inevitably be unsatisfactory. Hence, the objective of AdaBoost is to sequentially generate weak classifiers $G_k(X), k = 1, 2, \ldots, N$, and then combine them. A strong classifier $H(X)$ is composed of a few combination strategies. For regression analysis, the combination is expressed as follows:

$$H(X) = \nu \sum_{k=1}^{N} \left(\ln \frac{1}{a_k}\right) g(X) \tag{19}$$

where a_k is the weight of the weak classifier ($G_k(X)$), $g(X)$ is the median of all $a_k G_k(X)$, k = 1,2,...,N, and $\nu \in [0,1]$ is used as a regulatory factor or to prevent overfitting. Both the weak classifier ($G_k(X)$) and weight a_k are generated using the modified value of the existing learning data. As such, the distribution weight of each sample is adjusted based on the error predicted by the previous weak classifier ($G_{k-1}(X)$). Incorrectly predicted samples are repeatedly trained by increasing the weight such that they will be prioritized in the next learning process. During the iteration of k = 1,2,...,N, the weak classifier ($G_k(X)$) and relative prediction error e_{ki} are calculated using Eq. (19). Subsequently, the total error rate e_k is expressed as follows (Eq. (20)):

$$e_k = \sum_{i=1}^{m} e_{ki} \tag{20}$$

Furthermore, the weight a_k of the weak classifier can be represented as follows (Eq. (21)):

$$\alpha_k = \frac{e_k}{1 - e_k} \tag{21}$$

Finally, for the next step learning, the weight distribution of each sample ($w_{k+1,i}$) is updated again as follows (Eq. (22)):

$$w_{k+1,i} = \frac{w_{k,i} \alpha_k^{1-e_{ki}}}{\sum_{i=1}^{m} w_{k,i} \alpha_k^{1-e_{ki}}} \tag{22}$$

Between the two types of weights (w_k, α_k) defined above, the first (w_k) involves training the data sample and is used to enable better training in the next step after the weight of the incorrectly predicted sample is increased. The second (α_k) implies a weak classifier and is used to such that a more accurate weak classification will impose a greater effect on the final result. AdaBoost provides a stronger framework than specific learning algorithms because it does not provide a specific form of the weak classifier $G(X)$. Theoretically, every type of ML regression algorithm can be used as a weak classifier in AdaBoost.

3. Application of ML in Coastal and Marine Engineering Field

3.1 Wave Prediction

Accurate wave estimations can be applied to coastal engineering, marine transportation, and leisure sports. For example, the transportation route can be optimized by reducing the transportation

time through accurate wave information prediction, which can provide accurate prediction information regarding the generation of wave energy. Furthermore, useful information can be provided to surfers in a surf zone by providing wave information at a coast. Significant wave height is an important parameter in coastal port structure design and construction. Most physics-based models are applied to estimate such wave information. However, wave estimation studies based on ML models have increased recently (Deo and Naidu, 1999; Balas et al., 2004; Mahjoobi et al., 2008; Shahabi et al., 2016; Oh and Suh, 2018; Garcia et al., 2021).

James et al. (2018) developed an ML model to predict the characteristics of wave distributions. Data were generated via a few thousand rounds of iterative learning using a physics-based model known as the simulating waves nearshore (SWAN) model. Furthermore, a model for predicting the significant wave height and peak period using a multilayer perceptron and an SVM was proposed. A total of 741 input variables were applied considering the wave conditions at the interface (H_s, T_s, D), flow distribution within the grid (u,v), wind speed, and wind direction. Meanwhile, 11,078 data points were used for training, where two output variables (i.e., the significant wave height and peak period) calculated using the SWAN model were applied (Table A1). The result shows that the ML model reproduced more than 90% of the wave characteristics of the physics-based model, with an MSE of 9 cm. Moreover, the computation time is shorter compared with that afforded by the SWAN model; therefore, it is expected to be a promising alternative to the physics-based model. Fig. 3 shows a heat map presenting the difference ($\triangle H$) between the value predicted by the representative ML model and the value calculated using the SWAN model for the result of the ML model based on data derived from the calculations of 11,078 cases using the SWAN model. The image on the left shows the result of underestimating the significant wave height to a maximum of 15 cm near the bay, although the RMSE is 6 cm. However, the image on the right indicates an RMSE of 14 cm, although the error near the bay is smaller, and a clear location-based trend is not shown. Although statistical values such as the RMSE are important, the reliability of the model may differ by the application purpose. Therefore, the accuracy should be further improved through additional data analysis.

Shamshirband et al. (2020) constructed three ML models, i.e., the ANN, support vector regression (SVR), and the extreme learning machine (ELM) for wave height estimation and compared their performances with the results of the SWAN model. The input variable applied to the ML models was the near-surface wind speed, and the output variable was the significant wave height measured at the Bushehr and Assulayeh Ports of the Persian Bay. These variables were applied to training. The prediction performance of the ELM model was excellent, and the ML-based model of the Bushehr Port was reliable. However, for the Assaluyeh Port, the prediction accuracy for the significant wave height was low, and a correction was performed to improve the efficiency. Furthermore, the result of the ML model underestimated the extreme values. Hence, accurate input values and data preprocessing technology are necessitated to improve the result. The results of the SWAN model underestimated the extreme wave height. Both models require improvement for predicting extreme wave conditions. The ML-based model can be implemented at a low computational cost without requiring the depth information. However, unlike the SWAN model, it requires a separate model to predict the wave height of locations other than the two points used for training.

Chen et al. (2021) proposed a new surrogate model developed using the RF method, which is an ML model, based on spatial wave data estimated using the SWAN numerical model. Twelve input variables were used for model training: the significant wave height (H_s), mean

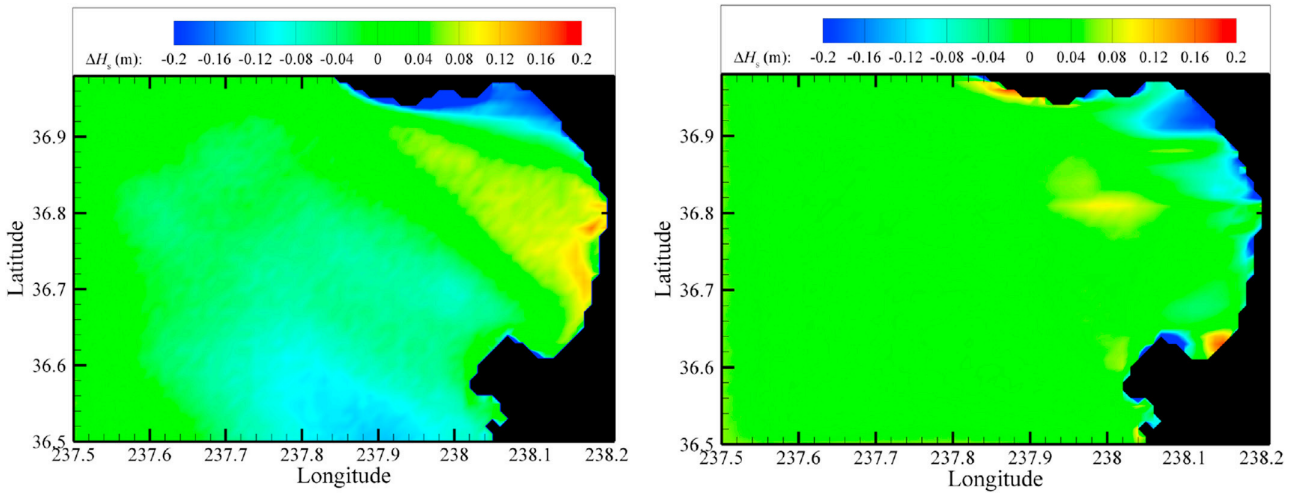

Fig. 3 Figure from James et al. (2018), who used ANN and SVM to predict the significant wave height (H_s) and wave period (T). Differences between SWAN- and machine-learning-simulated H_s selected from 11,078 SWAN model simulations are shown. Image of wave height differences on the left shows local discrepancy trends (RMSE = 6 cm in this image), which are not evident in the figure on the right, which in fact has a higher RMSE (i.e., 14 cm). Nevertheless, the domain shows primarily near-zero RMSEs, with local deviations at locations closer to the shoreline, where secondary effects are the most prominent.

wave direction (m_{Dir}), period (T_z), and peak period (T_p) at three buoys. For the output variable, the spatial wave information derived via SWAN calculation was used. The result of the ML model agreed better with the on-site buoy observation values than with the result of the SWAN model, and the computation time of the ML model was 100 times shorter than that of the SWAN model.

Kim et al. (2010) calculated the expected damage of an inclined breakwater using an ANN. The ANN, which uses the tide level and deep-sea waves as input, was trained to predict shallow-sea significant waves. They proved that a high degree of expected damage can be estimated within a short duration by calculating the shallow sea waves.

Kang and Oh (2019) investigated the prediction of swell wave generation using the RF, logistic regression, the K-nearest neighbor algorithm, the ANN, and the SVM. Changes in the water temperature, atmospheric pressure, and tide level were confirmed as primary variables for predicting swell high waves. Furthermore, the RF model performed the best (prediction accuracy: 88.6%).

Park et al. (2020) estimated the significant wave height of an X-band radar using an ANN; this method was demonstrated to be superior over the conventional wave height observation method. The result of a comparative analysis based on Hujeong Beach in Uljin confirmed the high accuracy of the calculated significant wave height.

Lee et al. (2020) conducted a wave breaking prediction study using an open-source ML algorithm to quantitatively predict wave breaking on a coast. The prediction results for the wave breaking wave height and depth by their trained neural network showed better prediction performance compared with the results calculated using the conventional empirical formula.

3.2 Tide Level Prediction

Accurate predictions of the tide level are crucial because the tide level significantly affects navigation, leisure activities, and coastal ecosystems. Tides refer to the periodic ascent and descent of the Earth's sea level due to tidal forces caused by the sun and moon. Thus, the tide level is an important parameter in terms of coastal engineering, maritime safety, and maritime activities. Various other factors such as the wind speed and atmospheric pressure must be considered in addition to the tide level. A harmonic analysis method in which many sine wave components are superimposed is generally used to predict the tide level; however, the effects of time-dependent factors are difficult to consider in this method. This paper introduces research cases that apply an ML model for tide level prediction in coastal and marine engineering.

The conventional harmonic decomposition method requires a significant amount of observational tidal data. Moreover, the parameters of the harmonic analysis model are estimated using the least-squares method based on data obtained for a long duration (i.e., more than 1 month). Lee (2004) constructed an ANN model using short-term measurements for tide level prediction and applied the $\cos(w_n t_j)$ and $\sin(w_n t_j)$ functions for 69 tidal components as input variables. Consequently, the primary components were determined based on two months' worth of measurement data. A comparison between the ANN and harmonic analysis models showed improved accuracy by the ANN model. Moreover, when 15 d of observation data were applied to training, the model presented prediction results that were applicable for predicting the tide levels for 1 year.

These tidal changes involve complex processes that are affected by not only the movement of celestial bodies, but also by nonperiodic meteorological factors such as wind, atmospheric pressure, and water temperature. However, the effect of time-dependent factors cannot be considered using the conventional harmonic analysis method. Therefore, Li et al. (2018) developed a tide level prediction model

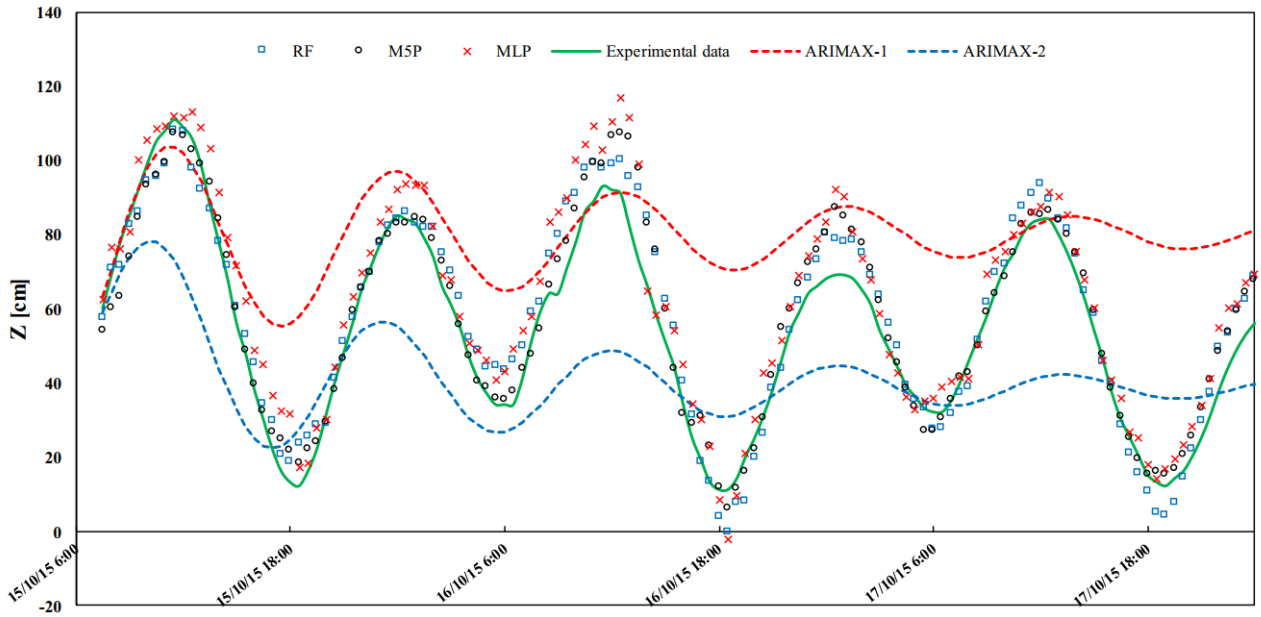

Fig. 4 Figure from Granta and Nunno (2021), who used M5P, RF and ANN to predict tide level. Forecast of tide fluctuations with 5 h advance: comparison between ML-based and ARIMAX models.

using the ELM to consider various nonlinear factors such as wind, air pressure, and water temperature. They presented results with higher accuracy and time efficiency than those yielded by conventional harmonic analysis models.

Granta and Nunno (2021) suggested a tide level prediction model using M5P, RF, and ANN algorithms (which are ML models). A total of 28 input variables were used in that study, including the astronomical tide (AT), wind speed (WS), barometric pressure (BP), and previously observed tide levels (Z_{-24} to Z_{-1}) to construct a tide level prediction model. Fig. 4 shows the tide level prediction results using the three ML models and the ARIMAX regression analysis. The M5P model showed a high coefficient of determination of 0.924–0.996. The result of sensitivity analysis showed high-level prediction results without considering meteorological factors (WS, BP), including for exceptionally high water levels. These results suggest that the training dataset can be continuously updated and applied to sea level fluctuations caused by climate change and subsidence.

3.3 Estimation of Design Variables

Several phenomena pertaining to wave–structure interactions exist, such as reflections in the structure, wave breaking on the slope and at the front, dissipation, wave runups and rundowns, transmitted waves, and overtopping. Therefore, techniques for understanding and quantitatively estimating these phenomena are required for the design of structures. Various studies have been conducted to estimate the primary design variables (Goyal et al., 2014; Lee and Suh, 2019; Lee and Suh, 2020; Etemad-Shahidi et al., 2016; Najafzadeh et al., 2014). Herein, we provide examples of applying the ML model for calculating the stability number, overtopping rate, wave transmission coefficient, and reflection coefficient.

3.3.1 Estimating stability number

Kim and Park (2005) constructed a stability number calculation model for rubble-mound breakwater using an ANN. For the input variables of the model, seven parameters were applied, including porosity (P), the number of wave attacks (N_W), damage level (S_d), structure slope ($\cos\alpha$), wave height (H_s), wave period (T_s), dimensionless water depth (h/H_s), and spectral shape (SS). Moreover, the stability number (N_s) was set as the output model. The result shows that the ML model demonstrated higher accuracy in predicting the stability number and damage level compared with the results obtained using the conventional empirical formula. Therefore, it can be utilized for design purposes.

Yagci et al. (2005) modeled the damage rates of different breakwaters using ANN, multiple LR, and fuzzy models. The experimental results yielded by the multiple LR model were unsatisfactory. However, they reported that the neural network and fuzzy model results can be estimated through interpolation for missing values.

Etemad-Shahidi and Bonakdar (2009) constructed a stability prediction model for rubble-mound breakwater using the M'5 model. Five input parameters were applied to the model: porosity (P), the number of wave attacks (N_W), damage level (S_d), surf similarity coefficient (ξ_m), and dimensionless water depth (h/H_s). Based on comparison, the results obtained showed higher accuracy compared with those obtained using the conventional Van der Meer empirical equation. A new equation was derived based on the M5' model, which proved to be useful for engineering design.

Based on the experimental data of Van der Meer et al. (1988), Koc et al. (2016) suggested a stability number prediction model for breakwater using the genetic algorithm. The experiment result showed that the genetic algorithm afforded better prediction performance than the empirical equation for the stability number.

3.3.2 Estimating overtopping rate

EurOtop is a representative result of a study that predicted the overtopping rate using an ML tool. In the Crest Level Assessment of Coastal structures by Full-scale Monitoring, Neural Network Prediction, and Hazard Analysis on Permissible Wave Overtopping (CLASH) project (De Rouck et al., 2004), an ANN model was developed to predict the mean overtopping rate, q (Pullen, 2007).

Van Gent et al. (2007) constructed an ANN-based prediction model to estimate the overtopping rates of various coastal structures. A database comprising approximately 10,000 mathematical model data points obtained from the European CLASH project was used for model training. A complexity factor and a reliable factor (RF) were introduced to increase data reliability. Data with low reliability or high complexity were excluded from training. Subsequently, the remaining data were converted to $H_{m0,toe}$ = 1 m by applying Froude's law of similarity to match with the mathematical model test results. Fig. 5 describes the parameters used for training. As input variables, 15 parameters describing wave characteristics (e.g., the significant wave height, average period, and wave direction) and factors pertaining to the structural shape (e.g., ridge depth, crest width, and slope) were applied. The mean overtopping rate (q) was set as a dependent variable. The result suggests that the ANN model is sufficiently applicable for modeling the correlation between the input variables related to overtopping and the average overtopping rate in coastal structures. However, all datasets were applied for training without segmenting the dataset in this study, and data with $q < 10^{-6}$ m^3/s/m were excluded from training. Therefore, the generalization of the model is likely to be difficult.

Subsequently, errors in the CLASH database were corrected, and more than 17,000 datasets were expanded through the Innovative Technologies for Safer European Coasts in a Changing Climate project (Zanuttigh et al., 2014). The calculation for the overtopping rate and the estimated results for uncertainty were presented using an ANN model. In previous studies, data with $q < 10^{-6}$ m^3/s/m were removed as measurement errors by experiment were assumed to have increased. However, Zanuttigh et al. (2016) categorized all data into three quantitative classifiers and constructed a training and a prediction model. The result showed improved prediction accuracy compared

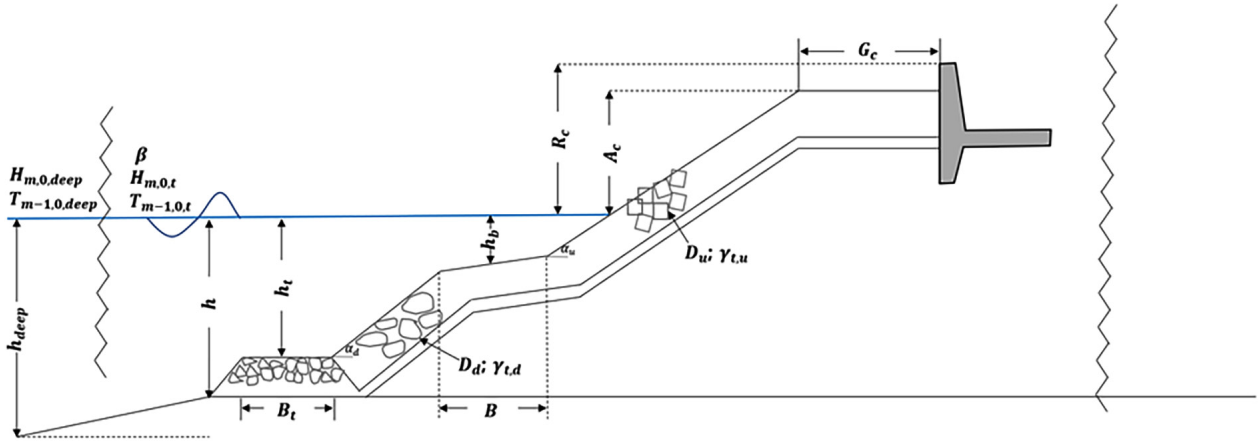

Fig. 5 Schematic illustration of structure based on CLASH, including geometrical and hydraulic parameters

with the results of previous studies, and the generalization performance was high even for data not used for training.

Den Bieman et al. (2020) and Den Bieman et al. (2021) constructed an overtopping rate prediction model using extreme gradient boosting (XGBoost)—an ML model. The result shows that the prediction error was 2.8 times lower than that of the existing neural network model. Moreover, they conducted variable importance analysis via feature engineering. The result shows that the XGBoost model can be successfully applied as an alternative to the ANN model.

Hosseinzadeh et al. (2021) constructed a mean overtopping rate prediction model for an inclined breakwater using GPR and SVR models, which are two kernel-based ML models. The result showed that the accuracy of the GPR model was higher than that of the conventional ANN model and empirical formula. Furthermore, they derived an optimal combination of input variables through sensitivity analysis and demonstrated that the prediction yielded is more accurate than that afforded by the combination of input variables by Van der Meer et al. (2018).

3.3.3 Wave trasmission and reflection coefficients

Formentin et al. (2017) proposed a prediction model for the mean overtopping rate and wave transmission/reflection coefficients (K_t and K_r) using the CLASH database to predict wave–structure interactions. An ANN was applied (as an ML model), and 15 nondimensional input variables were applied while considering the structural characteristics (geometric structure, amplitude, and roughness) and wave attack (wave slope and wave direction). Moreover, the overtopping rate, wave transmission coefficient, and reflection coefficient were set as output variables. The result showed that the ANN model afforded a higher prediction accuracy than the existing empirical formula and can be useful for design.

Kuntoji et al. (2018) proposed a prediction model for the wave transmission rate of underwater breakwaters using SVM and ANN models. They developed a model by applying eight input variables, including the wave slope (H_i/gT^2) and relative reef width. The prediction result showed that the SVM model to which the kernel function was applied afforded a higher accuracy than the ANN model with an coefficient of dtermination (R^2) value of 0.984.

Gandomi et al. (2020) estimated the wave transmission and reflection coefficients of permeable breakwater structures using a genetic algorithm, an ANN, and an SVM. Seven input variables including the porosity, relative wave height, and wave slope were

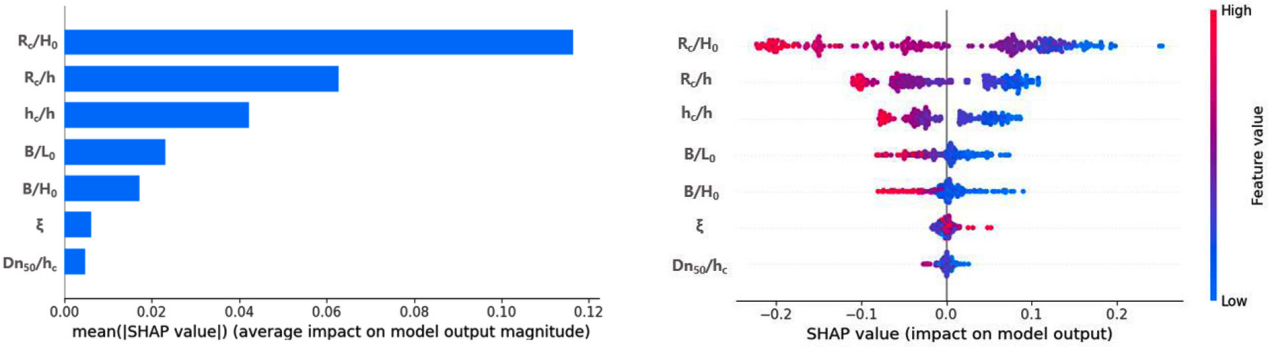

(a) **(b)**

Fig. 6 Figure from Kim et al. (2021), who used ML model to predict the wave transmission coefficient. Graphs show the variable importance, where the x-axis represents the average absolute Shapley values of the input variables throughout the data. (a) SHAP feature importance; (b) summary plot (feature effects).

applied as input variables. Moreover, the wave transmission and reflection coefficients were set as output variables. The result showed that the exponential GPR model performed the best for a correlation analysis between experimental and predicted values. They proposed a formula for calculating wave transmission and reflection coefficients using a Gaussian model.

Kim et al. (2021) constructed an ML model for estimating the wave transmission coefficient of low-crested structures using data from a mathematical model used in an experiment conducted through the DELOS project. They adjusted the hyperparameters via grid search for 10 ML models such as GBR, AdaBoost, and Gaussian regression, and selected an ML model suitable for the data. Seven nondimensional input variables such as the relative ridge depth and relative crest width were applied as input variables, whereas the wave transmission coefficient was set as an output variable. In addition, they analyzed the correlation between the input variable and the dependent variable using an explanatory AI technique and determined the dominant factor affecting the prediction of the wave transmission coefficient. Fig. 6 shows the variable importance results for each input variable based on the dependent variable analyzed using the ML analysis tool. The factor related to the ridge depth contributed the most toward the prediction of the output variable. This suggests that the reliability of the model should be improved through model analysis instead of constructing a simple ML model.

3.4 Prediction of Morphological Changes

Studies for further understanding and predicting shoreline fluctuations have been actively conducted, owing to the possibility of increasing coastal erosion acceleration promoted by climate change over the past few decades. The quantitative prediction of coastal erosion and restoration is effective for mitigating erosion risks and is essential for establishing a strategic beach management plan. Therefore, the prediction of beach profile deformation due to waves and beach currents is one of the most important tasks in coastal engineering. Various factors such as wind and waves, beach slope, tide level, sediment particle size, and storm surge frequency can affect beach deformation. Various approaches are available for predicting changes in the beach profile. Sediment movement, erosion, and deposition along a coast are primarily estimated based on empirical formulas; however, the corresponding physical mechanism has not been fully clarified. Recently, data-based ML models have been introduced and used for predicting shoreline fluctuations, barrier islands, and sand dune erosion (Yoon et al., 2013; Wilson et al., 2015; Passarella et al., 2018).

Hashemi et al. (2010) predicted the seasonal variation characteristics of beach profiles using an ANN model based on seven years' worth of beach profile data from 19 stations near Tremadoc Bay. Nine parameters were applied as input variables for the model, i.e., the minimum wind speed, wind direction, continuous storm frequency, storm frequency, significant wave height, significant period, wave, beach slope, and wind duration. In addition, they constructed a model using 12 output variables, i.e., the elevation of 10 points of each cross-sectional profile, the area under each profile curve, and the length of the profile. The result showed that the MSE converged to 0.0007 compared with the observed value, demonstrating the high prediction accuracy of the model in estimating beach variability characteristics. These study results suggest that the ML model can be a more effective tool for predicting changes in the beach profile than the mathematical model for the same points, owing to the complexity and uncertainty associated with the physical understanding of morphological dynamics at the shore. However, the ML model is applicable to only previous measurement data; it cannot be applied easily to abnormal climates or structures that are not reflected in the training data. Therefore, a study combining mathematical models and ML is necessary.

Rigos et al. (2016) constructed a model comprising an ANN using the feedforward method to predict the beach circulation pattern of a coast comprising a reef. The beachrock reef in front of the beach increased the complexity of wave actions and nonlinearities. Legendre polynomials were applied as an activation function to reflect this nonlinearity. Data for training were obtained from long-term time-series data for 10 months from January to November 2014 on the target coast. Six independent variables were applied as input variables, i.e., the ridge depth, structure slopes, structure width, significant wave height, and peak wave period. Subsequently, the model was built by setting the offshore distance as a dependent variable.

López et al. (2017) predicted the sandbar generated on a coast by applying an ANN model. Seven input variables were applied, including the wave characteristics, sediment characteristics, and time data. A model was constructed to predict the location of the sandbar crossing the shore based on six dependent variables at the barrier islands' feature points (start, ridge, and end points). The results showed that the error of the neural network model was lower than that of the general empirical formula for predicting the characteristics of barrier islands.

Montaño et al. (2020) conducted a workshop and contest related to the shoreline fluctuation model "Shoreshop," where participants from 15 international organizations tested and improved the performance of the model for predicting shoreline changes. They presented the result of a modeling contest, in which 19 models including the conventional numerical model were tested using the data pertaining to the daily average shoreline position and beach rotation for approximately 18 years (between 1999 and 2017) in the target sea, Tairua Beach. The result showed that the performance of the ML model was comparable to those of conventional numerical models. In fact, the multiyear variability at shorelines, which is difficult to simulate using conventional numerical models, can be analyzed easily using their model. Fig. 7 shows the results of shoreline fluctuations predicted using a numerical model, an ML model, and a hybrid model. Shoreline fluctuations during extreme events that occurred on a short time scale (~monthly) was difficult to reproduce using the general numerical model. Meanwhile, the ML model adequately reproduced shoreline

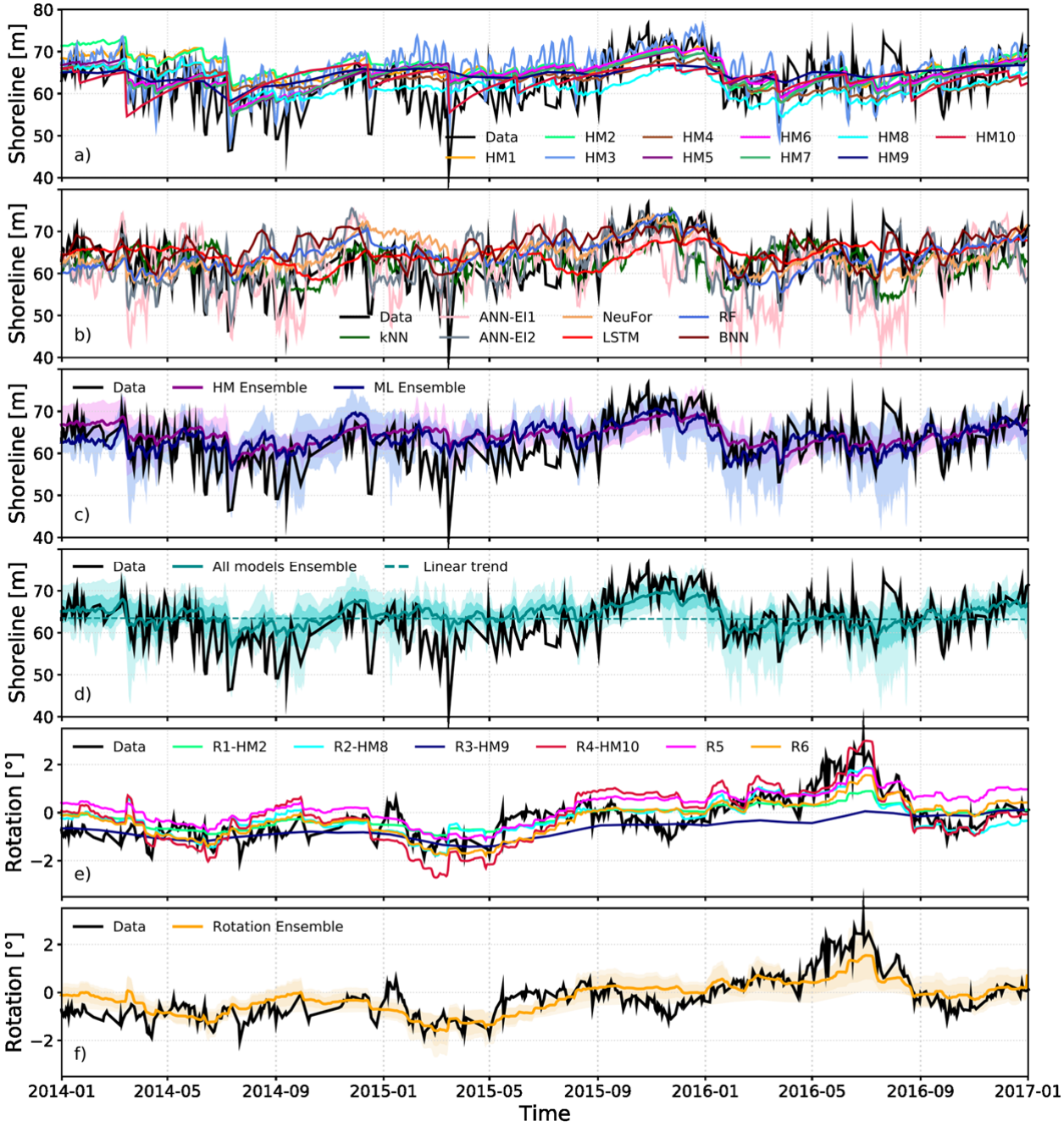

Fig. 7 Figure from Montaño et al. (2020), who used ML and numerical model to predict shoreline evolution. Model outputs (see legends) compared with observations (black): (a) Hybrid models; (b) ML models; (c) HM and ML ensemble; (d) multimodel ensemble; (e) rotation models; (f) hybrid model ensemble for beach rotation. Dark shadows in ensemble figures represent one standard deviation of model prediction. Light shadows represent maxima/minima envelope of model predictions. See Methods section and Supporting Information for model details.

fluctuations in extreme events. However, the ability of the ML model in predicting the shoreline position deteriorated for the case involving data not used for training (2014–2017). Therefore, the ML (inductive) and numerical (deductive) models complement each other in estimating shoreline fluctuations owing to their different approaches. Consequently, the ensemble approach combining the ML and numerical models improved the prediction reliability and reduced the uncertainty of the model.

4. Conclusions

In this study, we examined waves, tide level and sea level fluctuations, design variable estimation, and morphological changes in several studies that applied ML in coastal engineering. Based on extensive studies, the ML model proved to be a reliable in solving problems related to coastal engineering. The ML model can be constructed by learning the correlations between the input and output

variables without basic mathematical and physical understanding pertaining to extremely complex interactions and processes associated with coastal engineering. However, several factors should be considered from the researcher's perspective to implement such highly accurate models, including the following:

(1) Amount of data

A significant amount of training data with various ranges is required to construct an ML model. However, the exact amount of data required to derive meaningful prediction results remains elusive. Goldstein et al. (2019) reported that the performance deteriorates when a significant amount of data is applied to a low-complexity model in certain cases. These results cannot be generalized to all cases. However, the amount of data required for optimal prediction using the empirical knowledge of researchers and the method for managing noise in the data must be analyzed quantitatively.

(2) Data preprocessing

Actual data were acquired from various sources and processes; hence, incomplete data, noise, and inconsistent data that reduce the quality of the dataset may be included in the acquired data. Researchers must perform appropriate data preprocessing to improve data quality to achieve high-performance models. During data preprocessing, the model data should be converted into data suitable for the model through data cleaning, which replaces missing values or removes noise data and outliers. Furthermore, data normalization should be performed to reduce dimension and noise by via feature scale matching. For example, Zanuttigh et al. (2016) introduced a weight factor to the preprocessing process for more than 17,000 data points obtained from the CLASH database and reduced the data impurity via bootstrap sampling. Furthermore, the range of the dependent variables was $10^{-9} < q < 10$ but might be underestimated due to error calculation. Thus, a study was performed to improve the accuracy of the model by converting the dependent variable into $\log(q)$. The reliability and accuracy of the model could be further improved through appropriate data preprocessing based on the results of previous studies.

(3) Model analysis

An ML model is a black box model with a complex structure. Therefore, its intuitive interpretation ability is low for supporting the prediction results. To improve the limitations of such black box models, explainable artificial intelligence (XAI) is currently being conducted. The XAI methodology provides interpretation such that humans can understand the results predicted by ML algorithms. The model is reliable if the basis on which the model derived the prediction results through XAI can be determined. Furthermore, one can determine whether the model has been appropriately trained or whether the data used for training are appropriate. Kim et al. (2021) analyzed a wave transmission coefficient prediction model for low-crested structures using the Shapley additive explanation (SHAP). Simple ML models should be constructed and reliable model analyses should be conducted based on previous results.

(4) Model validation and generalization

ML models generally segregate the data into training and test datasets randomly. However, data under extreme conditions or data with important information may be excluded from the training process, and this possibility should be considered when segregating the data. The reliability of the model should be improved through cross-validation, such as the k-fold cross validation and leave one out cross-validation. Furthermore, the model constructed through verification should perform a generalization process using new data that have not been used for training. Montaño et al. (2020) presented the results of blinding tests on a numerical model and an ML model through workshops and competitions pertaining to "Shoreshop," which is a shoreline fluctuation model. The exchange and dissemination of knowledge among researchers worldwide should be promoted, and problems in coastal engineering should be solved from various angles through such modeling contests.

Coastal engineering researchers can obtain new knowledge and insights regarding data analysis via ML models. However, the ML model is an inductive approach rather than a deductive approach, which is the conventional approach used in numerical models. Hence, it is difficult to generalize the model based on the range and characteristics of the data. For example, in regard to the prediction of morphological changes, generalizing all regions based on a single model is difficult because the data characteristics of a specific region are reflected in the model. Therefore, various problems in the coastal engineering field should be solved using an ensemble model that combines the conventional numerical model with an ML model, and by deriving results that improve prediction performance through a mutual complement of their strengths and weaknesses.

Conflict of Interest

Woo-Dong Lee serves as an editor of the Journal of Ocean Engineering and Technology but does not decide the publication of this article. No potential conflicts of interest relevant to this article are reported.

Funding

This study was conducted under the support of the Korea Research Foundation with funding from the government in 2022 (Ministry of Science and ICT) (No. NRF-2022R1C1C2004838).

References

Balas, C.E., Koc, L., & Balas, L. (2004). Predictions of Missing Wave Data by Recurrent Neuronets. Journal of Waterway, Port, Coastal, and Ocean Engineering, 130(5), 256–265. https://doi.org/10.1061/(ASCE)0733-950X(2004)130:5(256)

Boser, B.E., Guyon, I., & Vapnik, V.N. (1992). A Training Algorithm for Optimal Margin Classifiers. Proceedings of the Fifth Annual Workshop on Computational Learning Theory, 5, 144−152. Pittsburgh, ACM. https://doi.org/10.1145/130385.130401

Chen, J., Pillai, A.C., Johanning, L., & Ashton, I. (2021). Using Machine Learning to Derive Spatial Wave Data: A Case Study for a Marine Energy Site. Environmental Modelling & Software, 142, 105066. https://doi.org/10.1016/j.envsoft.2021.105066

De Rouck, J., Van de Walle, B., & Geeraerts, J. (2004). Crest Level Assessment of Coastal Structures by Full Scale Monitoring, Neural Network Prediction and Hazard Analysis on Permissible Wave Overtoppingg - (CLASH). Proceedings of the EurOCEAN 2004 (European Conference on Marine Science & Ocean Technology), Galway, Ireland, EVK3-CT-2001-00058, 261−262.

Dwarakish, G.S., Rakshith, S., & Natesan, U. (2013). Review on Applications of Neural Network in Coastal Engineering. Artificial Intelligent Systems and Machine Learning, 5(7), 324−331.

Den Bieman, J.P., Wilms, J.M., Van den Boogaard, H.F.P., & Van Gent, M.R.A. (2020). Prediction of Mean Wave Overtopping Discharge Using Gradient Boosting Decision Trees. Water, 12(6), 1703. https://doi.org/10.3390/w12061703

Den Bieman, J.P., Van Gent, M.R.A., & Van den Boogaard, H.F.P. (2021). Wave Overtopping Predictions Using an Advanced Machine Learning Technique. Coastal Engineering, 166, 103830. https://doi.org/10.1016/j.coastaleng.2020.103830

Deo, M.C., & Naidu, C.S. (1999). Real Time Wave Forecasting Using Neural Networks. Ocean Engineering, 26(3), 191−203. https://doi.org/10.1016/S0029-8018(97)10025-7

Deo, M.C., & Jagdale, S.S. (2003). Prediction of Breaking Waves with Neural Networks. Ocean Engineering, 30(9), 1163−1178. https://doi.org/10.1016/S0029-8018(02)00086-0

Etemad-Shahidi, A., & Bonakdar, L. (2009). Design of rubble-mound breakwaters using M5 machine learning method. Applied Ocean Research, 31(3), 197−201. https://doi.org/10.1016/j.apor.2009.08.003

Etemad-Shahidi, A., Shaeri, S., & Jafari, E. (2016). Prediction of wave overtopping at vertical structures. Coastal Engineering 109, 42−52. https://doi.org/10.1016/j.coastaleng.2015.12.001

Pullen, T., Allsop, N.W.H., Bruce, T., Kortenhaus, A., Schüttrumpf, H., & van der Meer, J.W. (2007). European Manual for the Assessment of Wave Overtopping. Pullen, T., Allsop, N.W.H., Bruce, T., Kortenhaus, A., Schüttrumpf, H. & van der Meer, J.W.(Eds.), HR Wallingford.

Van der Meer, J.W., Allsop, N.W.H., Bruce, T., De Rouck, J., Kortenhaus, A., Pullen, T., ... Zanuttigh, B. (2018). Manual on Wave Overtopping of Sea Defences and Related Structures: An Overtopping Manual Largely Based on European Research, but for Worldwide Application (2nd ed.). EurOtop. Retrieved from http://www.overtopping-manual.com/assets/downloads/EurOtop_II_2018_Final_version.pdf

Formentin, S.M., Zanuttigh, B., & van der Meer, J.W. (2017). A Neural Network Tool for Predicting Wave Reflection, Overtopping and Transmission. Coastal Engineering Journal, 59(1), 1750006-1-1750006-31. https://doi.org/10.1142/S0578563417500061

Gandomi, M., Moharram, D.P., Iman, V., & Mohammad, R.N. (2020). Permeable Breakwaters Performance Modeling: A Comparative Study of Machine Learning Techniques. Remote Sensing, 12(11), 1856. https://doi.org/10.3390/rs12111856

Goyal, R., Singh, K., & Hegde, A.V. (2014). Quarter Circular Breakwater: Prediction 3 of Transmission Using Multiple Regression 4 and Artificial Neural Network. Marine Technology Society Journal, 48(1).

Goldstein, E.B., Coco, G., & Plant, N.G. (2019). A Review of Machine Learning Applications to Coastal Sediment Transport and Morphodynamics. Earth-Science Reviews, 194, 97−108. https://doi.org/10.1016/j.earscirev.2019.04.022

Gracia, S., Olivito, J., Resano, J., Martin-del-Brio, B., Alfonso, M., & Alvarez, E. (2021). Improving Accuracy on Wave Height Estimation Through Machine Learning Techniques. Ocean Engineering, 236, 108699. https://doi.org/10.1016/j.oceaneng.2021.108699

Granta, F., & Nunno, F.D. (2021). Artificial Intelligence Models for Prediction of the Tide Level in Venice. Stochastic Environmental Research and Risk Assessment, 35, 2537−2548. https://doi.org/10.1007/s00477-021-02018-9

Hashemi, M.R., Ghadampour, Z., & Neill, S.P., (2010). Using an Artifi cial Neural Network to Model Seasonal Changes in Beach Profi les. Ocean Engineering, 37(14−15), 1345−1356. https://doi.org/10.1016/j.oceaneng.2010.07.004

Hosseinzadeh, S., Etemad-Shahidi, A., & Koosheh, A. (2021). Prediction of Mean Wave Overtopping at Simple Sloped Breakwaters Using Kernel-based Methods. Journal of Hydroinformatics, 23(5), 1030−1049. https://doi.org/10.2166/hydro.2021.046

James, S.C., Zhang, Y., & O'Donncha, F. (2018). A Machine Learning Framework to Forecast Wave Conditions. Coastal Engineering, 137, 1−10. https://doi.org/10.1016/j.coastaleng.2018.03.004

Kang, D.H., & Oh, S.J. (2019). A Study of Machine Learning Model for Prediction of Swelling Waves Occurrence on East Sea. Journal of Korean Institute of Information Technology, 17(9), 11−17. https://doi.org/10.14801/jkiit.2019.17.9.11

Kankal, M., & Yuksek, O. (2012). Artificial Neural Network Approach for Assessing Harbor Tranquility: The Case of Trabzon Yacht Harbor, Turkey. Applied Ocean Research, 38, 23−31. https://doi.org/10.1016/j.apor.2012.05.009

Kim, D.H., & Park, W.S. (2005). Neural Network for Design and Reliability Analysis of Rubble Mound Breakwaters. Ocean Engineering, 32, 1332−1349. https://doi.org/10.1016/j.oceaneng.2004.11.008

Kim, D.H., Kim, Y.J., Hur, D.S., Jeon, H.S., & Lee, C.H. (2010). Calculating Expected Damage of Breakwater Using Artificial

Neural Network for Wave Height Calculation. Journal of Korean Society of Coastal and Ocean Engineers, 22(2), 126−132.

Kim, H.I., & Kim, B.H. (2020). Analysis of Major Rainfall Factors Affecting Inundation Based on Observed Rainfall and Random Forest. Journal of the Korean Society of Hazard Mitigation, 20(6), 301−310. https://doi.org/10.9798/KOSHAM.2020.20.6.301

Kim, T., Kwon, S., & Kwon, Y. (2021). Prediction of Wave Transmission Characteristics of Low-Crested Structures with Comprehensive Analysis of Machine Learning. Sensors, 21(24), 8192. https://doi.org/10.3390/s21248192

Kim, Y.E., Lee, K.E., & Kim, G.S. (2020). Forecast of Drought Index Using Decision Tree Based Methods. Journal of the Korean Data & Information Science Society, 31(2), 273−288. https://doi.org/10.7465/jkdi.2020.31.2.273

Koc, M.L., Balas, C.E., & Koc, D.I. (2016). Stability Assessment of Rubble-mound Breakwaters Using Genetic Programming. Ocean Engineering, 111, 8−12. https://doi.org/10.1016/j.oceaneng.2015.10.058

Koo, M.H., Park, E.G., Jeong, J., Lee, H.M., Kim, H.G., Kwon, M.J., ... Jo, S.B. (2016). Applications of Gaussian Process Regression to Groundwater Quality Data. Journal of Soil and Groundwater Environment, 21(6), 67−79. https://doi.org/10.7857/JSGE.2016.21.6.067

Kuntoji, G., Manu, R., & Subba, R. (2020). Prediction of Wave Transmission over Submerged Reef of Tandem Greakwater Using PSO-SVM and PSO-ANN Techniques. ISH Journal of Hydraulic Engineering, 26(3), 283−290. https://doi.org/10.1080/09715010.2018.1482796

Lee, G.H., Kim, T.G., & Kim, D.S.(2020). Prediction of Wave Breaking Using Machine Learning Open Source Platform. Journal of Korean Society Coastal and Ocean Engineers, 32(4), 262−272. https://doi.org/10.9765/KSCOE.2020.32.4.262

Lee, J.S., & Suh, K.D. (2020). Development of Stability Formulas for Rock Armor and Tetrapods Using Multigene Genetic Programming. Journal of Waterway, Port, Coastal, and Ocean Engineering, 146(1), 04019027. https://doi.org/10.1061/(ASCE)WW.1943-5460.0000540

Lee, S.B., & Suh, K.D. (2019). Development of Wave Overtopping Formulas for Inclined Seawalls using GMDH Algorithm. KSCE Journal of Civil Engineering, 23, 1899−1910. https://doi.org/10.1007/s12205-019-1298-1

Lee, T.L. (2004). Back-propagation Neural Network for Long-term Tidal Prediction. Ocean Engineering, 31(2), 225−238. https://doi.org/10.1016/S0029-8018(03)00115-X

Li, B., Yin, J., Zhang, A., & Zhang, Z. (2018). A Precise Tidal Level Prediction Method Using Improved Extreme Learning Machine with Sliding Data Window. In 2018 37th Chinese Control Conference (CCC), 1787−1792. http://doi.org/10.23919/ChiCC.2018.8482902

Liu, Y., Esan, O. C., Pan, Z., & An, L. (2021). Machine Learning for Advanced Energy Materials. Energy and AI, 3, 100049. https://doi.org/10.1016/j.egyai.2021.100049

López, I., Aragonés, L., Villacampa, Y., Serra, J.C., (2017). Neural Network for Determining the Characteristic Points of the Bars. Ocean Engineering, 136, 141−151. https://doi.org/10.1016/j.oceaneng.2017.03.033

Mahjoobi, J., Etemad-Shahidi, A., & Kazeminezhad, M.H. (2008). Hindcasting of Wave Parameters Using Different Soft Computing Methods. Applied Ocean Research, 30(1), 28−36. https://doi.org/10.1016/j.apor.2008.03.002

Montaño, J., Coco, G., Antolínez, J.A.A., Beuzen, T., Bryan, K.R., Cagigal, L., ... Vos, K. (2020). Blind Testing of Shoreline Evolution Models. Scientific Report, 10, 2137. https://doi.org/10.1038/s41598-020-59018-y

Na, Y.Y., Park, J.G., & Moon, I.C. (2017). Analysis of Approval Ratings of Presidential Candidates Using Multidimensional Gaussian Process and Time Series Text Data. Proceedings of the Korean Operations Research And Management Society, Yeosu, 1151-1156.

Najafzadeh, M., Barani, G.-A., & Kermani, M.R.H. (2014). Estimation of Pipeline Scour Due to Waves by GMDH. Journal of Pipeline Systems Engineering and Practice, 5(3), 06014002. https://doi.org/10.1061/(ASCE)PS.1949-1204.0000171

Oh, J., & Suh, K.-D. (2018). Real-time Forecasting of Wave Heights Using EOF-wavelet-neural Network Hybrid Model. Ocean Engineering, 150, 48−59. https://doi.org/10.1016/j.oceaneng.2017.12.044

Panizzo, A., & Briganti, R. (2007). Analysis of Wave Transmission Behind Low-crested Breakwaters Using Neural Networks. Coastal Engineering, 54(9), 643−656. https://doi.org/10.1016/j.coastaleng.2007.01.001

Park, J.S., Ahn, K.M., Oh, C.Y., & Chang, Y.S. (2020). Estimation of Significant Wave Heights from X-Band Radar Using Artificial Neural Network. Journal of Korean Society Coastal and Ocean Engineers, 32(6), 561−568. https://doi.org/10.9765/KSCOE.2020.32.6.561

Passarella, M., Goldstein, E.B., De Muro, S., Coco, G. (2018). The Use of Genetic Programming to Develop a Predictor of Swash Excursion on Sandy Beaches. Natural Hazards and Earth System Sciences, 18, 599−611. https://doi.org/10.5194/nhess-18-599-2018

Rigos, A., Tsekouras, G.E., Chatzipavlis, A., & Velegrakis, A.F. (2016). Modeling Beach Rotation Using a Novel Legendre Polynomial Feedforward Neural Network Trained by Nonlinear Constrained Optimization. In L. Iliadis, I. Maglogiannis (Eds.), Artificial Intelligence Applications and Innovations. AIAI 2016. IFIP Advances in Information and Communication Technology, 475, 167−179.

Salehi, H., & Burgueño, R. (2018). Emerging Artificial Intelligence Methods in Structural Engineering. Engineering Structures, 171, 170−189. https://doi.org/10.1016/j.engstruct.2018.05.084

Shahabi, S., Khanjani, M., & Kermani, M.H. (2016). Significant Wave Height Forecasting Using GMDH Model. International Journal

of Computer Applications, 133(6), 13-16.

Shamshirband, S., Mosavi, A., Rabczuk, T., Nabipour, N., & Chau, K.W. (2020). Prediction of Significant Wave Height; Comparison Between Nested Grid Numerical Model, and Machine Learning Models of Artificial Neural Networks, Extreme Learning and Support Vector Machines. Engineering Applications of Computational Fluid Mechanics, 14(1), 805-817. https://doi.org/10.1080/19942060.2020.1773932

Van der Meer, J.W. (1988). Rock Slopes and Gravel Beaches under Wave Attack (Ph.D. thesis). Delft University of Technology, Delft Hydraulics Report, 396.

Van Gent, M.R.A., Van den Boogaard, H.F.P., Pozueta, B., & Medina, J.R. (2007). Neural Network Modelling of Wave Overtopping at Coastal Structures. Coastal Engineering, 54(8), 586-593. https://doi.org/10.1016/j.coastaleng.2006.12.001

Wilson, K.E., Adams, P.N., Hapke, C.J., Lentz, E.E., & Brenner, O. (2015). Application of Bayesian Networks to Hindcast Barrier Island Morphodynamics. Coastal Engineering, 102, 30-43. https://doi.org/10.1016/j.coastaleng.2015.04.006

Yagci, O., Mercan, D.E., Gigizoglu, H.K., & Kabdasli, M.S. (2005). Artificial Intelligence Methods in Breakwater Damage Ratio Estimation. Ocean Engineering, 32(17-18), 2088-2106. https://doi.org/10.1016/j.oceaneng.2005.03.004

Yoon, H.-D., Cox, D.T., & Kim, M. (2013). Prediction of Time-dependent Sediment Suspension in the Surf Zone Using Artificial Neural Network. Coastal Engineering, 71, 78-86. https://doi.org/10.1016/j.coastaleng.2012.08.005

Zanuttigh, B., Formentin, S.M., & Van der Meer, J.W. (2014). Advances in Modelling Wave- structure Interaction Tthrough Artificial Neural Networks. Coastal Engineering Proceedings, 1(34), 693.

Zanuttigh, B., Formentin, S.M., & Van der Meer, J.W. (2016). Prediction of Extreme and Tolerable Wave Overtopping Discharges Thorough an Advanced Neural Network. Ocean Engineering, 127, 7-22.

Author ORCIDs

Author name	ORCID
Kim, Taeyoon	0000-0002-5060-5302
Lee, Woo-Dong	0000-0001-7776-4664

Appendix

Table A1 Detail informations of the reference

Reference	Input variables	Output variables	ML model	Hyper parameter
		Wave prediction		
James et al. (2018)	1) Wave conditon (H_s, T_z and D) 2) Oven-currents (357 values each for u, v) 3) Wind files (12 values each for u and v)	1) Significant wave height (H_s) 2) Wave period (T_z)	ANN SVM	NHN = 20 AF = ReLU
Shmshirband et al. (2020)	1) Surface wind speed	1) Significant wave height (H_s)	ANN SVM ELM	AF = Sigmoid OP = Levenberg-Marquardt
Chen et al. (2021)	1) Significant wave height (H_s) 2) Mean wave direction (D) 3) Wave period (T_z) 4) Peak period (T_p)	1) Significant wave height (H_s) 2) Wave period (T_z) 3) Peak period (T_p)	RF	-
		Tide level		
Lee et al. (2004)	1) 69 tidal constituent ($\cos(w_n t_j)$, $\sin(w_n t_j)$)	1) Tidal levels	ANN	NHN = 7 AF = Sigmoid Momentum factor=0.8
Granta and Nunno (2021)	1) Astronomical tide (AT) 2) Wind speed (WS) 3) Barometric pressure (BP) 4) Observed tide levels (Z-24 ~ Z-1)	1) Tide level	M5P ANN RF	-
		Design variables		
Kim and Park (2005)	1) Permeability of breakwater (P) 2) The number of wave attack (NW) 3) Damage level (S_d) 4) Slope of structure ($\cos\alpha$) 5) Significant wave height (H_s) 6) Wave period (T_s) 7) Dimensionless water depth (h/H_s) 8) Spectral Shape (SS)	1) Stability number (Ns)	ANN	NHN = 12 AF = Non linear

Table A1 Detail informations of the reference (Continuation)

Reference	Input variables	Output variables	ML model	Hyper parameter
Etemad-Shahidi and Bonakda (2009)	1) Permeability of breakwater (P) 2) The number of wave attack (NW) 3) Damage level (S_d) 4) Surf similarity coefficient (ξ_m) 5) Dimensionless water depth (h/H_s)	1) Stability number (Ns)	M5'	-
van Gent et al. (2007)	1) Significant wave height at the structure toe($H_{mo,t}$) 2) Spectral wave period at the structure toe($T_{m-1,\ o}$) 3) Wave obliquity (β) 4) Toe submergence (h_t) 5) Slope of structure ($\cos\alpha$) . . .	1) Wave overtopping discharge (q*)	ANN	NHN = 20 AF = Non linear Bootstrap resampling
Zanuttigh et al. (2016)	14 variables 1) Wave steepness ($H_{m0,t}/L_{m-1,0,t}$) 2) Wave obliquity (β) 3) Shoaling parameter ($h/L_{m-1,0,t}$) 4) Effect of the toe submergence ($ht/H_{m-1,0,t}$) 5) Effect of the toe width ($Bt/L_{m-1,0,t}$) . . .	1) Wave overtopping discharge (q*)	ANN	NHN = 20 AF = Hyperbolic tangent sigmoid OP = Levenberg-Marquardt Bootstrap resampling
Den Bieman et al. (2021)	15 variables 1) Crest Freeboard(R_c) 2) Roughness factor for cot α_u (γ_{fu}) 3) Crest width (G_c) 4) Berm width (B) 5) Slope of structure ($\cos\alpha$) . . .	1) Wave overtopping discharge (q*)	XG boost	Max_depth = 7 Min-child-weight = 5 Learning_rate = 0.05 Subsample = 1 Reg_lamda = 1 Bootstrap resampling
Formentin et al. (2017)	16 variables 1) Wave steepness ($H_{m0,t}/L_{m-1,0,t}$) 2) Wave obliquity(β) 3) Shoaling parameter ($h/L_{m-1,0,t}$) 4) Effect of the toe submergence ($ht/H_{m-1,0,t}$) 5) Effect of the toe width ($Bt/L_{m-1,0,t}$) . . .	1) Wave overtopping discharge (q*) 2) Wave reflection coefficient (Kr) 3) Wave transmission coefficient (Kt)	ANN	NHN = 20 AF = Hyperbolic tangent sigmoid OP = Levenberg-Marquardt Bootstrap resampling
Kuntoji et al. (2018)	15 variables 1) Relative wave steepness (H_i/gT^2) 2) Relative spacing (X/d) 3) Stability number (H_i/Dn_{50}) 4) Relative crest widths (B/d) 5) Relative crest widths (B/L_o) 6) Relative crest heights (h/d) 7) Relative submergence (F/H_i) 8) Relative water depth (d/gT^2)	1) Wave transmission coefficient (Kt)	ANN SVM	1) ANN NHN = 3 2) SVM C = 183.78 ε = 0.0000538 d = 3
Gandomi et al. (2020)	1) Relative chamber width (B/h) 2) Relative rockfill height (d/h) 3) Relative chamber width in terms of wavelength (B/L_p) 4) Wave steepness (H_s/L_p) 5) Wave number multiplied by water depth (kh) 6) Relative wave height in terms of rockfill height (H_s/d) 7) Permeability of the back wall (p)	1) Wave reflection coefficient (Kr) 2) Wave transmission coefficient (Kt)	LR SVM GPR GP ANN	1) GPR Kernel Function = Exp Kernel Scale = 1.664473 Basic Function = Constant SSD = 0.063, 0.105 Sigma = 0.063, 0.105

Table A1 Detail informations of the reference (Continuation)

Reference	Input variables	Output variables	ML model	Hyper parameter
Kim et al. (2021)	1) Relative freeboard (R_c/H_0) 2) Relative crest width (B/H_0) 3) Surf similarity parameter (ξ) 4) Relative crest width (B/L_0) 5) Relative freeboard to water depth ratio (R_c/h) 6) Ratio of the nominal diameter to the crest height (Dn_{50}/h_c) 7) Relative structure height (h_c/h)	1) Wave transmission coefficient (Kt)	GPR ANN GBR RF SVM LR . . .	-
Morphological and morphodynamic				
Hashemi et al. (2010)	1) Min wind speed 2) Wind direction 3) Number of successive wind 4) Number of wind 5) Significant wave height 6) Significant wave period 7) Direction of wave 8) Angle of beach 9) Wind duration	1) Elevation of 10points on each profile 2) Area under each profile curve 3) Length of profile	ANN	NHN = 20 AF = tanh
Rigos et al. (2016)	1) Freeboard (d) 2) inshore slope (ω_1) 3) offshore slope (ω_2) 4) reef width (w) 5) Significant wave height (H_s) 6) Peak wave period (T_p)	1) The distance from the reef top point to the shoreline (y)	ANN	NHN = 4 AF = Legendre polynomial
López et al. (2017)	1) Month of survey profile 2) Steepness corresponding to the maximum wave height 3) H_{max} direction 4) Days elapsed from H_{max} to the survey profile 5) H_m 6) d_{50} 7) Difference in beach width between profiles	1) Distance from shoreline to the start of the bar (X_s) 2) Depth of the starting point of the bar (Y_s) 3) Distance from shoreline to the crest (X_c) 4) Depth of the crest (Y_c) 5) Distance from shoreline to the final of the bar (X_f) 6) Final point depth (Y_f)	ANN	NHN = 12 AF = sigmoid

NHN = Number of Hidden Neuron, AF = Activation Function, OP = Optimizer

Instructions for Authors

General information

To submit a manuscript to the Journal of Ocean Engineering and Technology (JOET), it is advised to first carefully read the aims and the scope section of this journal, as it provides information on the editorial policy and the category of papers it accepts. Unlike many regular journals, JOET usually has no lag in acceptance of a manuscript and its publication. Authors that find a match with the aims and the scope of JOET are encouraged to submit as we publish works from all over the world. JOET adheres completely to guidelines and best practices published by professional organizations, including Principles of Transparency and Best Practice in Scholarly Publishing (joint statement by COPE, DOAJ, WAME, and OASPA (http://doaj.org/bestpractice) if otherwise not described below. As such, JOET would like to keep the principles and policies of those professional organizations during editing and the publication process.

Research and publication ethics

Details on publication ethics are found in http://joet.org/authors/ethics.php. For the policies on research and publication ethics not stated in the Instructions, Guidelines on Good Publication (http://publicationethics.org/) can be applied.

Requirement for membership

One of the authors who submits a paper or papers should be member of the Korean Society of Ocean Engineers (KSOE), except a case that editorial board provides special admission of submission.

Publication type

Article types include scholarly monographs (original research articles), technical articles (technical reports and data), and review articles. The paper should have not been submitted to other academic journal. When part or whole of a manuscript was already published to conference papers, research reports, and dissertations, then the corresponding author should note it clearly in the manuscript.

Copyright

After published to JOET, the copyright of manuscripts should belong to KSOE. A transfer of copyright (publishing agreement) form can be found in submission website (http://www.joet.org).

Manuscript submission

Manuscript should be submitted through the on-line submission website (http://www.joet.org). The date that manuscript was received through on-line website is the official date of receipt. Other correspondences can be sent by an email to the Editor in Chief or secretariat. The manuscript must be accompanied by a signed statement that it has been neither published nor currently submitted for publication elsewhere. The manuscript should be written in English or Korean. Ensure that online submission are in a standard word processing format. Corresponding author must write the manuscript using the JOET template provided in Hangul or MS Word format. Ensure that graphics are high-resolution. Be sure all necessary files have been uploaded/ attached.

Authors' checklist

Please refer to “Authors' Checklist” for details.

Article structure

Manuscript must be edited in the following order: (1) Title, (2) Authors' names and affiliations, (3) Keywords, (4) Abstract, (5) Nomenclature (optional), (6) Introduction, (7) Main body (analyses, tests, results, and discussions), (8) Conclusions, (9) Conflict of interest (optional), (10) Funding (optional), (11) Acknowledgements (optional), (12) References, (13) Appendices (optional), (14) Author’s ORCIDs.

Abstract

A concise and factual abstract is required. The abstract should state briefly the background, purpose and methods of the research, the principal results and conclusions. An abstract should be written in around 300 words. References are not cited in abstract whenever possible. Also, non-standard or uncommon abbreviations should be avoided, but if essential they must be defined at their first mention in the abstract itself.

Keywords

Immediately after the abstract, provide a maximum of 5 or 6 keywords.

Unit

Use the international system units(SI). If other units are mentioned, please give their equivalent in SI.

Equations

All mathematical equations should be c1early printed/typed using well accepted explanation. Superscripts and subscripts should be typed clearly above or below the base line. Equation numbers should be given in Arabic numerals enclosed in parentheses on the right-hand margin.

Tables

Tables should be numbered consecutively with Arabic numerals. Each table should be fully titled. All tables should be referred to in the texts.

Figures

Figures should be numbered consecutively with Arabic numerals. Each figure should be fully titled. All figures should be referred to in the texts. All the illustrations should be of high quality meeting with the publishing requirement with legible symbols and legends.

Conflict of interest

It should be disclosed here according to the statement in the Research and publication ethics regardless of existence of conflict of interest. If the authors have nothing to disclose, please state: “No potential

conflict of interest relevant to this article was reported."

Funding

Funding to the research should be provided here. Providing a FundRef ID is recommended including the name of the funding agency, country and if available, the number of the grant provided by the funding agency. If the funding agency does not have a FundRef ID, please ask that agency to contact the FundRef registry (e-mail: fundref.registry@crossref.org). Additional detailed policy of FundRef description is available from http://www.crossref.org/fundref/. Example of a funding description is as follows:

The study is supported by the Inha University research fund (FundRef ID: 10.13039/501100002632), and the Korea Health Personnel Licensing Examination Institute research fund (FundRef ID: 10.13039/501100003647).

Acknowledgments

Any persons that contributed to the study or the manuscript, but not meeting the requirements of an authorship could be placed here. For mentioning any persons or any organizations in this section, there should be a written permission from them.

References in text

References in texts follow the APA style. Authors can also see how references appear in manuscript text through the 'Template'.

Reference list

Reference list follows the APA style. Authors can see how references should be given in reference section through the 'Template'.

Appendices

The appendix is an optional section that can contain details and data supplemental to the main text. If there is more than an appendix, they should be identified as A, B, C, etc. Formulae and equations in appendices should be given separate numbering: Eq. (A1), Eq. (A2), etc.; in a subsequent appendix, Eq. (B1) and so on. Similarly for tables and figures: Table A1; Fig. A1, etc.

ORCID (Open Researcher and Contributor ID)

All authors are recommended to provide an ORCID. To obtain an ORCID, authors should register in the ORCID web site: http://orcid.org. Registration is free to every researcher in the world. Example of ORCID description is as follows:

Joonmo Choung: https://orcid.org/0000-0003-1407-9031

Peer review and publication process

The peer review process can be broadly summarized into three groups: author process, review process, and publishing process for accepted submissions. General scheme is presented in Figure 1.

Check-in process for review

If the manuscript does not fit the aims and scope of the Journal or does not adhere to the Instructions to Authors, it may be rejected immediately after receipt and without a review. Before reviewing, all submitted manuscripts are inspected by Similarity Check powered by iThenticate (https://www.crossref.org/services/similarity-check/), a plagiarism-screening tool. If a too high degree of similarity score is found, the Editorial Board will do a more profound content screening.

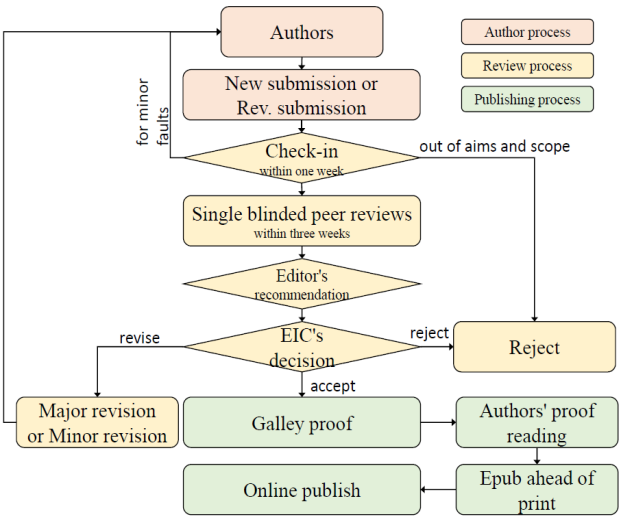

Figure 1 Flow chart of the peer review and publication process of JOET

The criterion for similarity rate for further screening is usually 15%; however, rather than the similarity rate, the Editorial Board focuses on cases where specific sentences or phrases are similar. The settings for Similarity Check screening are as follows: It excludes quotes, bibliography, small matches of 6 words, small sources of 1%, and the Methods section.

Number of reviewers

Reviewers will be selected from the list of reviewers. Manuscripts are then peer reviewed by at least 2 experts in the corresponding field, usually by 2.

Peer review process and the author response to the reviewer comments

JOET adopts single blind review, which means that the authors do not know the identity of the reviews. All papers, including those invited by the Editor, are subject to peer review.

The review period is 4 weeks. Usually the first decision is made within a week after completion of the review. The Editorial Board's decision after the review will be one of followings: Accept, Minor revision, Major revision, or Rejection. The Editorial Board may request the authors to revise the manuscript according to the reviewers' comments. If there are any requests for revision of the manuscript by the reviewers, the authors should do their best to revise the manuscript. If the reviewer's opinion is not acceptable or is believed to misinterpret the data, the author should reasonably indicate that. After revising the manuscript, the author should upload the revised files with a separate response sheet to each item of the reviewer's commentary. The author's revisions should be completed within 3 months after the request. If it is not received by the due date, the Editorial Board will notify the author. To extend the revision period beyond 3 months, the author should negotiate that with the Editorial Board. The manuscript review process can be provided for up two rounds. If the authors wish further review, the Editorial Board may consider it. The Editorial Board will make a final decision on the approval of the submitted manuscript for publication and can request any further corrections, revisions, and deletions of the article text if necessary. Statistical editing is also performed if the data requires professional statistical review by a statistician.

Processing after acceptance

If the manuscript is finally accepted, the galley proof will be sent to the corresponding author after professional manuscript editing and English proofreading. Proofreading should be performed for any misspellings or errors by the authors. Proofreading manuscript for publication is provided to the corresponding author, and the corresponding author must review the proofreading manuscript. Corresponding authors are responsible for the content of the proofreading manuscript and any errors. After final proofreading, the manuscript may appear at the journal homepage as an article in press with a unique DOI number for rapid communication. All published articles will be replaced by the replacement XML file and a final PDF.

Feedback after publication

If the authors or readers find any errors, or contents that should be revised, it can be requested from the Editorial Board. The Editorial Board may consider erratum, corrigendum or a retraction. If there are any revisions to the article, there will be a CrossMark description to announce the final draft. If there is a reader's opinion on the published article with the form of Letter to the editor, it will be forwarded to the authors. The authors can reply to the reader's letter. Letter to the editor and the author's reply may be also published.

How the journal handle complaints and appeals

The policy of JOET is primarily aimed at protecting the authors, reviewers, editors, and the publisher of the journal. If not described below, the process of handling complaints and appeals follows the guidelines of the Committee of Publication Ethics available from: https://publicationethics.org/appeals

- *Who complains or makes an appeal?*

Submitters, authors, reviewers, and readers may register complaints and appeals in a variety of cases as follows: falsification, fabrication, plagiarism, duplicate publication, authorship dispute, conflict of interest, ethical treatment of animals, informed consent, bias or unfair/inappropriate competitive acts, copyright, stolen data, defamation, and legal problem. If any individuals or institutions want to inform the cases, they can send a letter via the contact page on our website: https://www.joet.org/about/contact.php. For the complaints or appeals, concrete data with answers to all factual questions (who, when, where, what, how, why) should be provided.

- *Who is responsible to resolve and handle complaints and appeals?*

The Editorial Board or Editorial Office is responsible for them. A legal consultant or ethics editor may be able to help with the decision making.

- *What may be the consequence of remedy?*

It depends on the type or degree of misconduct. The consequence of resolution will follow the guidelines of the Committee of Publication Ethics (COPE).

Article processing charge

Payment due

Article processing charge (APC) covers the range of publishing services JOET provides. This includes provision of online tools for editors and authors, article production and hosting, and customer services. Upon editorial acceptance of an article for the regular review service and upon submission of an article for the fast review service, the corresponding author will be notified that payment is due.

APC

The APC up to 6 pages is ₩200,000 (or ＄200) and ₩550,000 (or ＄550) for the for the regular and fast review services, respectively. An extra APC of $50 per page is charged for papers longer than 6 pages, No taxes are included in this charge. For the fast review service, an advance fee of ₩250,000 ($250) should be paid on submission.

Payment methods

Credit card payment can be made online using a secure payment form as soon as the manuscript has been editorially accepted. We will we send a receipt by email once payment has been processed. Please note that payment by credit card carries a surcharge of 10% of the total APC.

Invoice payment is due within 7 days of the manuscript receiving editorial acceptance. Receipts are available on request.

JOET Templet 2021.02.04.

Journal of Ocean Engineering and Technology 00(0), 000-000, December, 2100
https://doi.org/10.26748/KSOE.2100.000
pISSN 1225-0767
eISSN 2287-6715

Original Research Article, Technical Article, Review Article, etc

Title of Article

Firstname Lastname[1], Firstname Lastname[2] and Firstname Lastname[3]

[1]*Professor, Department of OO, OO School, OO University, Busan, Korea*
[2]*Graduate Student, Department of OO, OO University, Seoul, Korea*
[3]*Senior Researcher, Department of OO, OO Engineering. Corp., Seoul, Korea*

KEY WORDS: Lumped mass line model, Explicit method, Steel lazy wave riser (provide a maximum of 5 or 6 keywords.)

ABSTRACT: *A concise and factual abstract is required. The abstract should state briefly the background, purpose and methods of the research, the principal results and conclusions. An abstract should be written in around 300 words. References are not cited in abstract whenever possible. Also, non-standard or uncommon abbreviations should be avoided, but if essential they must be defined at their first mention in the abstract itself.*

Nomenclature (Optional)

ITOC	Increment of total operating cost ($/yr)
LHV	Lower heating value (kJ/kg)
Pw	Power (kW)
T	Temperature (K)
V	Volume (m^3)
ρ	Density (kg/m^3)

1. Introduction

The introduction should briefly place the study in a broad context and highlight why it is important. It should define the purpose of the work and its significance. The current state of the research field should be reviewed carefully and key publications cited. Please highlight controversial and diverging hypotheses when necessary. Finally, briefly mention the main aim of the work and highlight the principal conclusions. As far as possible, please keep the introduction comprehensible to scientists outside your particular field of research.

2. General Information for Authors

2.1 Research and Publication Ethics

Authorship should be limited to those who have made a significant contribution to the conception, design, execution, or interpretation of the reported study. All those who have made significant contributions should be listed as co-authors. Where there are others who have participated in certain substantive aspects of the research project, they should be acknowledged or listed as contributors.

The corresponding author should ensure that all appropriate co-authors and no inappropriate co-authors are included on the paper, and that all co-authors have seen and approved the final version of the paper and have agreed to its submission for publication.

Details on publication ethics are found in the journal's website (http://joet.org/authors/ethics.php). For the policies on research and publication

Received 00 February 2100, revised 00 October 2100, accepted 00 October 2100
Corresponding author Firstname Lastname: +82-51-759-0656, e-mail@e-mail.com
It is a recommended paper from the proceedings of 2019 spring symposium of the Korea Marine Robot Technology (KMRTS).

ethics not stated in the Instructions, Guidelines on Good Publication (http://publicationethics.org/) can be applied.

2.2 Requirement for Membership

One of the authors who submits a paper or papers should be member of The Korea Society of Ocean Engineers (KSOE), except a case that editorial board provides special admission of submission.

2.3 Publication Type

Article types include scholarly monographs (original research articles), technical articles (technical reports and data), and review articles. The paper should have not been submitted to other academic journal. When part or whole of a manuscript was already published to conference papers, research reports, and dissertations, then the corresponding author should note it clearly in the manuscript.

Example: It is noted that this paper is revised edition based on proceedings of KAOST 2100 in Jeju.

2.4 Copyright

After published to JOET, the copyright of manuscripts should belong to KSOE. A transfer of copyright (publishing agreement) form can be found in submission website (http://www.joet.org).

2.5 Manuscript Submission

Manuscript should be submitted through the on-line submission website (http://www.joet.org). The date that manuscript was received through on-line website is the official date of receipt. Other correspondences can be sent by an email to the Editor in Chief or secretariat. The manuscript must be accompanied by a signed statement that it has been neither published nor currently submitted for publication elsewhere. The manuscript should be written in English or Korean. Ensure that online submission are in a standard word processing format. Corresponding author must write the manuscript using the JOET template provided in Hangul or MS Word format. Ensure that graphics are high-resolution. Be sure all necessary files have been uploaded/ attached.

2.5.1 Authoer's checklist

Authoer's checklist and Transfer of copyright can be found in submission hompage (http:/www.joet.org).

3. Manuscript

Manuscript must be edited in the following order: (1) Title, (2) Authors' names and affiliations, (3) Keywords, (4) Abstract, (5) Nomenclature (optional), (6) Introduction, (7) Main body (analyses, tests, results, and discussions), (8) Conclusions, (9) Conflict of interest (optional), (10) Funding (optional), (11) Acknowledgements (optional), (12) References, (13) Appendices (optional), (14) Author's ORCIDs.

3.1 Unit

Use the international system units(SI). If other units are mentioned, please give their equivalent in SI.

3.2 Equations

All mathematical equations should be clearly printed/typed using well accepted explanation. Superscripts and subscripts should be typed clearly above or below the base line. Equation numbers should be given in Arabic numerals enclosed in parentheses on the right-hand margin. The parameters used in equation must be defined. They should be cited in the text as, for example, Eq. (1), or Eqs. (1)–(3).

$$G_{GEV}(x;\mu,\sigma,\xi)=\begin{cases}\exp[-(1+\xi(x-\mu)/\sigma)^{-1/\xi}] & \xi\neq 0\\ \exp[-\exp(-(x-\mu)/\sigma)] & \xi=0\end{cases} \tag{1}$$

in which μ, σ, and ξ represent the location ("Shift" in figures), scale, and shape parameters, respectively.

3.3 Tables

Tables should be numbered consecutively with Arabic numerals. Each table should be typed on a separate sheet of paper and be fully titled. All tables should be referred to in the texts.

Table 1 Tables should be placed in the main text near to the first time they are cited

Item	Buoyancy riser
Segment length[1)] (m)	370
Outer diameter (m)	1.137
Inner diameter (m)	0.406
Dry weight (kg/m)	697
Bending rigidity ($N \cdot m^2$)	1.66E8
Axial stiffness (N)	7.098E9
Inner flow density ($kg \cdot m^3$)	881
Seabed stiffness ($N/m/m^2$)	6,000

[1)]Tables may have a footer.

3.4 Figures

Figures should be numbered consecutively with Arabic numerals. Each figure should be fully titled. All the illustrations should be of high quality meeting with the publishing requirement with legible symbols and legends. All figures should be referred to in the texts. They should be referred to in the text as, for example, Fig. 1, or Figs. 1−3.

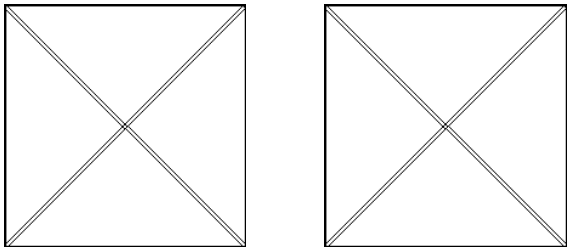

(a) Description of what is contained in the first panel

(b) Description of what is contained in the first panel

Fig. 1 Schemes follow the same formatting. If there are multiple panels, they should be listed as: (a) Description of what is contained in the first panel; (b) Description of what is contained in the second panel. Figures should be placed in the main text near to the first time they are cited

3.5 How to Describe the References in Main Texts

All references should be listed at the end of the manuscripts, arranged in order of Alphabet. References in texts follow the American Psychological Association (APA) style. The exemplary form of listed references is as follows:

Single author: (Kim, 1998) or Kim (1998)

Two authors: (Kim and Lee, 2000) or Kim and Lee (2000)

Three or more authors: (Kim et al., 1997) or Kim et al. (1997)

Two or more papers: (Lee, 1995a; Lee, 1995b; Ryu et al., 1998)

Year unknown: (Kim, n.d.) or Kim (n.d.)

4. Results

This section may be divided by subheadings. It should provide a concise and precise description of the experimental results, their interpretation as well as the experimental conclusions that can be drawn. Tables and figures are recommended to present the results more rapidly and easily. Do not duplicate the content of a table or a figure with in the Results section. Briefly describe the core results related to the conclusion in the text when data are provided in tables or in figures. Supplementary results can be placed in the Appendix.

5. Discussion

Authors should discuss the results and how they can be interpreted in perspective of previous studies and of the working hypotheses. The findings and their implications should be discussed in the broadest context possible. Future research directions may also be highlighted

6. Conclusions

This section can be added to the manuscript.

Conflict of Interest (Optional)

It should be disclosed here according to the statement in the Research and publication ethics regardless of existence of conflict of interest. If the authors have nothing to disclose, please state: “No potential conflict of interest relevant to this article was reported.”

Funding (Optional)

Please add: “This research was funded by Name of Funder, grant number XXX” and “The OOO was funded by XXX”. Check carefully that the details given are accurate and use the standard spelling of funding agency names at https://search.crossref.org/funding

Acknowledgments (Optional)

In this section you can acknowledge any support given which is not covered by the author contribution or funding sections. This may include administrative and technical support, or donations in kind (e.g., materials used for experiments). For mentioning any persons or any organizations in this section, there should be a written permission from them.

References

- Journal name should not be abbreviated.
- A private report with limited access or download availability can not be a reference.
- Include the digital object identifier DOI or URL for all references where available.
- Reference list follows the American Psychological Association (APA) style.

Referring to journal publications:

Author, A.A., Author, B.B., & Author, C.C. (Year). Title of Article. Journal Title, vol(no), pp–pp. https://doi.org/xx.xxxx/xxxxxx

Author, A.A., Author, B.B., Author, C.C. (accepted; in press). Title of Article. Title of Periodical. Retrieved from http://xx.xxx/x.pdf

Lee, T.K., Kim, T.W., Rim, C.W., & Kim, S.C. (2013). A Study on Calculation of Local Ice Pressures for ARAON Based on Data Measured at Arctic Sea. Journal of Ocean Engineering and Technology, 27(5), 88–92. https://doi.org/10.5574/KSOE.2013. 27.5.088

Lee, T.K., Kim, T.W., Rim, C.W., & Kim, S.C. (accepted; in press). A Study on Calculation of Local Ice Pressures for ARAON Based on Data Measured at Arctic Sea. Journal of Ocean Engineering and Technology, Retrieved from http://xxx.xxx/xxx.pdf

Referring to conference proceedings:

Author, A.A., Author, B.B., & Author, C.C. (Year). Title of Article. Proceeding Title, City, Country, pp–pp. https://doi.org/xx.xxxx

Aoki, S., Liu, H., & Sawaragi, T. (1994). Wave Transformation and Wave Forces on Submerged Vertical Membrane. Proceedings of International Symposium Waves - Physical and Numerical Modeling, Vancouver, Canada, 1287–1296.

Tsukamoto, C.L., Lee, W., Yuh, J., Choi, S.K., & Lorentz, J. (1997). Comparison Study on Advanced Thruster Control of Underwater Robots. Proceedings of International Conference on Robotics and Automation, 1845–1850. https://doi.org/110.1109/ROBOT.1997.619056

Referring to books:

Author, A.A. (Year). Title of Book (xx ed.). Location: Publisher.

Strunk, W., & White, E.B. (2000). The Elements of Style (4th ed.). NewYork, USA: Longman.

Schlichting, H. (1968). Boundary Layer Theory (6th ed.). New York, USA: McGraw-Hill.

Referring to theses or dissertations:

Author, A.A. (Year). Title of Doctoral Dissertation or Master’s thesis (Doctoral Dissertation or Master’s thesis). Name of Institution, City, Country.

Giovanni, I. (1998). Modelling and Identification of Underwater Robotic Systems (Ph.D. Thesis). University of Genova, Genova, Italy.

Referring to technical reports, rules, or guidelines:

Author, A.A. (Year). Title of report (Reprot No. xxx), Location: Publisher.

Likhomanov, V. (2010). Full-Scale Ice Trials of the Korean Research Icebreaker ARAON. Daejeon, Korea: Arctic and Antarctic Research Institute (AARI).

ABS. (2011). Guide for Ice Loads Monitoring Systems. Houston, USA: American Bureau of Shipping.

Lloyd's Register. (2011). FDA ICE Fatigue Induced by Ice Loading, ShipRight Design and construction - Fatigue Design Assesment. London, United Kingdom: Lloyd's Register.

Larson, M., & Kraus, N.C. (1989). SBEACH: Numerical Model for Simulating Storm-Induced Beach Change - Report 1 Empirical Foundation and Model Development (Technicla Report CERC-89-9). Coastal Engineering research center Vicksburg Ms.

Referring to patents:

Righsholder, A.A. (Year). Title of Patent. Patent number, Patent office with country.

Dawoo Shipbulding & Maringe Engineering (DSME). (2013). Distance Length Standardization Method for Preventing Interference at the time of Uploading Cell Guide of Container Ship. Unexamined Patent Publication 1020130044635, Korean Interllectual Property Office.

Referring to websites:

Righsholder, A.A. (Year). Title of webpage. Retrieved Month Year from http://xxxx

International Association of Classification Societies (IACS). (2010a). Common Structural Rules for Bulk Carriers. Retrieved July 2010 from http://www.iacs-data.org.uk

US Congressional Hearing. (2009). Strategic Importance of the Arctic in Us Policy. Retrieved June 2019 from https://fas.org/irp/arctic.pdf

Dawoo Shipbulding & Maringe Engineering (DSME). (2013). Distance Length Standardization Method for Preventing Interference at the time of Uploading Cell Guide of Container Ship. Retrieved June 2019 from https://patentimages.storage./pdfs/792.pdf

Referring to software:

Righsholder, A.A. (Year). Title of Software. Downloaded Month Year from http://xxxx

Standard

Organization. (Year). Title of the standard in italics [Translated title – if applicable] (Standard No.). Retrieved from https://...

International Organization for Standardization. (2005). Industrial sewing machines: Safety requirements for sewing machines, units and systems (ISO Standard No. 10821). Retrieved from http://www.standard.no/no/Nettbutikk/produktkatalogen/Produktpresentasjon/?ProductID=113554

Translation

Author, A. A. (Year of publication). Title of work: Capital letter also for subtitle (T. Translator, Trans.). Location: Publisher. (Original work published YEAR). DOI

Ura, T., & Takakawa, S. (2015). All about Submersibles (W.S. Kim, D.S. Kim, Y.H. Choi,.C.H. Park, J.S. Park, P.M. Lee, H.S. Jung, Trans.). Korea: CIR. (Original Work Published in 1994, Japan: Seizan-Shoten Publiching)

in text: (Ura and Takakawa, 1994/2015)

Referring to some exceptional cases:

- when authors are missing, institution can replace authors

National Oceanic and Atmospheric Administration (NOAA). (2015). Deep-ocean Assessment and Reporting of Tsunamis (DART). Retrieved December 2019 from https://nctr.pmel.noaa.gov/Dart/

- when dates or years are missing, it is replaced with "n.d."

National Oceanic and Atmospheric Administration (NOAA). (n.d.). Deep-ocean Assessment and Reporting of Tsunamis (DART).

- when more then seven authors, first 6 authors ... last author.

Yeu, T., Choi, H.T., Lee, Y., Chae, J., Lee, Y., Kim, S.S., ... Lee, T.H. (2019). Development of Robot Platform for Autonomous Underwater Intervention. Journal of Ocean Engineering and Technology, 33(2), 168–177. https://doi.org/10.26748/KSOE. 2019.021

Appendix (Optional)

The appendix is an optional section that can contain details and data supplemental to the main text. For example, explanations of experimental details that would disrupt the flow of the main text, but nonetheless remain crucial to understanding and reproducing the research shown; figures of replicates for experiments of which representative data is shown in the main text can be added here if brief, or as Supplementary data. Mathematical proofs of results not central to the paper can be added as an appendix.

All appendix sections must be cited in the main text. In the appendixes, Figures, Tables, etc. should be labeled starting with 'A', e.g., Fig. A1, Fig. A2, etc.

Examples:

https://doi.org/10.26748/KSOE.2019.022

https://doi.org/10.26748/KSOE.2018.4.32.2.095

Author ORCIDs

All authors are recommended to provide an ORCID. To obtain an ORCID, authors should register in the ORCID web site: http://orcid.org. Registration is free to every researcher in the world. Example of ORCID description is as follows:

Author name	ORCID
So, Hee	0000-0000-000-00X
Park, Hye-Il	0000-0000-000-00X
Yoo, All	0000-0000-000-00X
Jung, Jewerly	0000-0000-000-00X

Authors' Checklist

The following list will be useful during the final checking of a manuscript prior to sending it to the journal for review. Please submit this checklist to the KSOE when you submit your article.

< Checklist for manuscript preparation >

☐ I checked my manuscript has been 'spell-checked' and 'grammar-checked'.

☐ One author has been designated as the corresponding author with contact details such as
- E-mail address
- Phone numbers

☐ I checked abstract 1) stated briefly the purpose of the research, the principal results and major conclusions, 2) was written in around 300 words, and 3) did not contain references (but if essential, then cite the author(s) and year(s)).

☐ I provided 5 or 6 keywords.

☐ I checked color figures were clearly marked as being intended for color reproduction on the Web and in print, or to be reproduced in color on the Web and in black-and-white in print.

☐ I checked all table and figure numbered consecutively in accordance with their appearance in the text.

☐ I checked abbreviations were defined at their first mention there and used with consistency throughout the article.

☐ I checked all references mentioned in the Reference list were cited in the text, and vice versa according to the APA style.

☐ I checked I used the international system units (SI) or SI-equivalent engineering units.

< Authorship checklist >

JOET considers individuals who meet all of the following criteria to be authors:

☐ Made a significant intellectual contribution to the theoretical development, system or experimental design, prototype development, and/or the analysis and interpretation of data associated with the work contained in the article.

☐ Contributed to drafting the article or reviewing and/or revising it for intellectual content.

☐ Approved the final version of the article as accepted for publication, including references.

< Checklist for publication ethics >

☐ I checked the work described has not been published previously (except in the form of an abstract or as a part of a published lecture or academic thesis).

☐ I checked when the work described has been published previously in other proceedings without copyright, it has clearly noted in the text.

☐ I checked permission has been obtained for use of copyrighted material from other sources including the Web.

☐ I have processed Plasgiarism Prevention Check through reliable web sites such as www.kci.go.kr, http://www.ithenticate.com/, or https://www.copykiller.org/ for my submission.

☐ I agree that final decision for my final manuscript can be changed according to results of Plasgiarism Prevention Check by JOET administrator.

☐ I checked one author at least is member of the Korean Society of Ocean Engineers.

☐ I agreed all policies related to 'Research and Publication Ethics'

☐ I agreed to transfer copyright to the publisher as part of a journal publishing agreement and this article will not be published elsewhere including electronically in the same form, in English or in any other language, without the written consent of the copyright-holder.

☐ I made a payment for reviewing of the manuscript, and I will make a payment for publication on acceptance of the article.

☐ I have read and agree to the terms of Authors' Checklist.

Title of article	:	
Date of submission	: DD/MM/YYYY	
Corresponding author	:	signature
Email address	:	

※ E-mail this with your signature to ksoehj@ksoe.or.kr

Publishing Agreement

ARTICLE DETAILS

Title of article :

Corresponding author :

E-mail address :

DOI : https://doi.org/10.26748/KSOE.2XXX.XXX

YOUR STATUS

I am one author signing on behalf of all co-authors of the manuscript.

ASSIGNMENT OF COPYRIGHT

I hereby assign to the Korean Society of Ocean Engineers, the copyright in the manuscript identified above and any tables, illustrations or other material submitted for publication as part of the manuscript (the "Article"). This assignment of rights means that I have granted to Korean Society of Ocean Engineers the exclusive right to publish and reproduce the Article, or any part of the Article, in print, electronic and all other media (whether now known or later developed), in any form, in all languages, throughout the world, for the full term of copyright, and the right to license others to do the same, effective when the Article is accepted for publication. This includes the right to enforce the rights granted hereunder against third parties.

SCHOLARLY COMMUNICATION RIGHTS

I understand that no rights in patents, trademarks or other intellectual property rights are transferred to the Journal owner. As the author of the Article, I understand that I shall have: (i) the same rights to reuse the Article as those allowed to third party users of the Article under the CC-BY-NC License, as well as (ii) the right to use the Article in a subsequent compilation of my works or to extend the Article to book length form, to include the Article in a thesis or dissertation, or otherwise to use or re-use portions or excerpts in other works, for both commercial and non-commercial purposes. Except for such uses, I understand that the assignment of copyright to the Journal owner gives the Journal owner the exclusive right to make or sub-license commercial use.

USER RIGHTS

The publisher will apply the Creative Commons Attribution-Noncommercial Works 4.0 International License (CC-BY-NC) to the Article where it publishes the Article in the journal on its online platforms on an Open Access basis.

The CC-BY-NC license allows users to copy and distribute the Article, provided this is not done for commercial purposes and further does not permit distribution of the Article if it is changed or edited in any way, and provided the user gives appropriate credit (with a link to the formal publication through the relevant DOI), provides a link to the license, and that the licensor is not represented as endorsing the use made of the work. The full details of the license are available at http://creativecommons.org/licenses/by-nc/4.0/legalcode.

REVERSION OF RIGHTS

Articles may sometimes be accepted for publication but later rejected in the publication process, even in some cases after public posting in "Articles in Press" form, in which case all rights will revert to the author.

☑ I have read and agree to the terms of the Journal Publishing Agreement.

Corresponding author:

name signature

※ E-mail this with your signature to ksoehj@ksoe.or.kr (Papers will not be published unless this form is signed and returned)

Research and Publication Ethics

Journal of Ocean Engineering and Technology (JOET) adheres to the guidelines published by professional organizations, including Committee on Publication Ethics (COPE; https://publicationethics.org/)

1. Authorship

JOET considers individuals who meet all of the following criteria to be authors:

1) Made a significant intellectual contribution to the theoretical development, system or experimental design, prototype development, and/or the analysis and interpretation of data associated with the work contained in the article.
2) Contributed to drafting the article or reviewing and/or revising it for intellectual content.
3) Approved the final version of the article as accepted for publication, including references.

Contributors who do not meet all of the above criteria may be included in the Acknowledgment section of the article. Omitting an author who contributed to your article or including a person who did not fulfill all of the above requirements is considered a breach of publishing ethics.

Correction of authorship after publication: JOET does not correct authorship after publication unless a mistake has been made by the editorial staff.

2. Originality and Duplicate Publication

All submitted manuscripts should be original and should not be in consideration by other scientific journals for publication. Any part of the accepted manuscript should not be duplicated in any other scientific journal without permission of the Editorial Board, although the figures and tables can be used freely if the original source is verified according to the Creative Commons Attribution License (CC BY-NC). It is mandatory for all authors to resolve any copyright issues when citing a figure or table from other journal that is not open access.

3. Conflict-of-Interest Statement

Conflict of interest exists when an author or the author's institution, reviewer, or editor has financial or personal relationships that inappropriately influence or bias his or her actions. Such relationships are also known as dual commitments, competing interests, or competing loyalties. These relationships vary from being negligible to having a great potential for influencing judgment. Not all relationships represent true conflict of interest. On the other hand, the potential for conflict of interest can exist regardless of whether an individual believes that the relationship affects his or her scientific judgment. Financial relationships such as employment, consultancies, stock ownership, honoraria, and paid expert testimony are the most easily identifiable conflicts of interest and the most likely to undermine the credibility of the journal, the authors, or of the science itself. Conflicts can occur for other reasons as well, such as personal relationships, academic competition, and intellectual passion. If there are any conflicts of interest, authors should disclose them in the manuscript. The conflicts of interest may occur during the research process as well; however, it is important to provide disclosure. If there is a disclosure, editors, reviewers, and reader can approach the manuscript after understanding the situation and the background of the completed research.

4. Management Procedures for the Research and Publication Misconduct

When JOET faces suspected cases of research and publication misconduct such as a redundant (duplicate) publication, plagiarism, fabricated data, changes in authorship, undisclosed conflicts of interest, an ethical problem discovered with the submitted manuscript, a reviewer who has appropriated an author's idea or data, complaints against editors, and other issues, the resolving process will follow the flowchart provided by the Committee on Publication Ethics (http://publicationethics.org/resources/flowcharts). The Editorial Board of JOET will discuss the suspected cases and reach a decision. JOET will not hesitate to publish errata, corrigenda, clarifications, retractions, and apologies when needed.

5. Editorial Responsibilities

The Editorial Board will continuously work to monitor and safeguard publication ethics: guidelines for retracting articles; maintenance of the integrity of the academic record; preclusion of business needs from compromising intellectual and ethical standards; publishing corrections, clarifications, retractions, and apologies when needed; and excluding plagiarism and fraudulent data. The editors maintain the following responsibilities: responsibility and authority to reject and accept articles; avoiding any conflict of interest with respect to articles they reject or accept; promoting publication of corrections or retractions when errors are found; and preservation of the anonymity of reviewers.

6. Hazards and human or animal subjects

If the work involves chemicals, procedures or equipment that have any unusual hazards inherent in their use, the author must clearly identify these in the manuscript. If the work involves the use of animal or human subjects, the author should ensure that the manuscript contains a statement that all procedures were performed in compliance with relevant laws and institutional guidelines and that the appropriate institutional committee(s) has approved them. Authors should include a statement in the manuscript that informed consent was obtained for experimentation with human subjects. The privacy rights of human subjects must always be observed.

Ensure correct use of the terms sex (when reporting biological factors) and gender (identity, psychosocial or cultural factors), and, unless inappropriate, report the sex and/or gender of study participants, the sex of animals or cells, and describe the methods used to determine sex and gender. If the study was done involving an exclusive population, for example in only one sex, authors should justify why, except in obvious cases. Authors should define how they determined race or ethnicity and justify their relevance.

7. Secondary publication

It is possible to republish manuscripts if the manuscripts satisfy the conditions of secondary publication. These are:

- The authors have received approval from the Editorial Board of both journals (the editor concerned with the secondary publication must have access to the primary version).
- The priority for the primary publication is respected by a publication interval negotiated by editors of both journals and the authors.
- The paper for secondary publication is intended for a different group of readers
- The secondary version faithfully reflects the data and interpretations of the primary version.
- The secondary version informs readers, peers, and documenting agencies that the paper has been published in whole or in part elsewhere, for example, with a note that might read, "This article is based on a study first reported in the [journal title, with full reference]"
- The title of the secondary publication should indicate that it is a secondary publication (complete or abridged republication or translation) of a primary publication.

8. Complaints and Appeals

The process of handling complaints and appeals follows the guidelines of the COPE available from: https://publicationethics. org/appeals

9. Post-publication discussions and corrections

The post-publication discussion is available through letter to editor. If any readers have a concern on any articles published, they can submit letter to editor on the articles. If there found any errors or mistakes in the article, it can be corrected through errata, corrigenda, or retraction.

(사)한국해양공학회 특별회원

한국해양공학회의 특별회원은 다음과 같으며, 귀사의 찬조에 진심으로 감사드립니다.(순서: 입회순)

한국선급 / 현대중공업㈜ / 대우조선해양㈜ / 선박해양플랜트연구소 /
대양전기공업㈜ / ㈜대영엔지니어링 / 한국해양조선기자재연구원 /
한국조선해양플랜트협회 / (주)파나시아 / 선보공업(주) / ㈜멀티스하이드로 /
SK건설(주) / 삼성중공업(주) / ㈜유에스티21 / ㈜해양정보기술

한국해양공학회 특별회원 가입방법은 학회홈페이지(www.ksoe.or.kr)의
입회안내를 참고하시고, 기타사항은 학회 사무국으로 연락주시기 바랍니다.

The Korean Society of Ocean Engineers